UNIVERSIDADE FEDERAL DE SANTA CATARINA
PROGRAMA DE PÓS-GRADUAÇÃO EM ENGENHARIA MECÂNICA

Gil Felix Greco

A COMPUTATIONAL INVESTIGATION OF JET-PLATE INTERACTION NOISE USING A LATTICE-BOLTZMANN BASED METHOD

Florianópolis

2018

Gil Felix Greco

A COMPUTATIONAL INVESTIGATION OF JET-PLATE INTERACTION NOISE USING A LATTICE-BOLTZMANN BASED METHOD

Dissertação submetida ao Programa de Pós-Graduação em Engenharia Mecânica da Universidade Federal de Santa Catarina para a obtenção do Grau de Mestre em Engenharia Mecânica.
Orientador: Prof. Andrey Ricardo da Silva, Ph.D.

Florianópolis
2018

Ficha de identificação da obra elaborada pelo autor,
através do Programa de Geração Automática da Biblioteca Universitária da UFSC.

Greco, Gil Felix
A computational investigation of jet-plate interaction noise using a Lattice-Boltzmann based method / Gil Felix Greco ; orientador, Andrey Ricardo da Silva, 2018.
170 p.

Dissertação (mestrado) - Universidade Federal de Santa Catarina, Centro Tecnológico, Programa de Pós Graduação em Engenharia Mecânica, Florianópolis, 2018.

Inclui referências.

1. Engenharia Mecânica. 2. Aeroacústica. 3. Ruído de jato. 4. Interação fluído-estrutura. 5. Método de Lattice-Boltzmann. I. da Silva, Andrey Ricardo . II. Universidade Federal de Santa Catarina. Programa de Pós-Graduação em Engenharia Mecânica. III. Título.

Gil Felix Greco

A COMPUTATIONAL INVESTIGATION OF JET-PLATE INTERACTION NOISE USING A LATTICE-BOLTZMANN BASED METHOD

Esta Dissertação foi julgada adequada para a obtenção do título de "Mestre em Engenharia Mecânica", e aprovada em sua forma final pelo Programa de Pós-Graduação em Engenharia Mecânica.

Florianópolis, 14 de Dezembro de 2018.

Prof. Jonny Carlos da Silva, Dr. Eng.
Coordenador do Curso

Banca Examinadora:

Prof. Andrey Ricardo da Silva, Ph.D. – Orientador
Universidade Federal de Santa Catarina, Brasil

Prof. César José Deschamps, Ph.D.
Universidade Federal de Santa Catarina, Brasil

Prof. Júlio Apolinário Cordioli, D.Eng.
Universidade Federal de Santa Catarina, Brasil

Victor Henrique Pereira da Rosa, Ph.D.
Universidade Federal de Santa Catarina, Brasil

Aos meus amados avós, Vilnei e Marlene.

ACKNOWLEDGEMENTS

First of all, I would like to thank my family for the unconditional love and support. In special, to my Father, Gilnei, my greatest inspiration for the world of science. I own all my gratitude to my grandparents, Vilnei and Marlene, and to my Mother, Glades, and Sister, Liz. An very special thanks to Valéria for being on my side during this journey. After all, this work would not be possible without you.

My deepest thanks goes to my advisor, Prof. Andrey da Silva, who has believed in my potential for the academy by supporting my work and for providing me many opportunities since the undergraduation years. It has been a pleasure to work and learn from you through all these years of partnership.

I would like to thank my colleagues from the Jet Noise team: Henrique, Murilo and Simas. An special thanks to Neto for the friendship and patience in sharing his knowledge during countless hours of technical discussions.

To my dearest friends from the Aeroacoustics team: André and Fernanda, Bonomo, Braga, Drone guy, Felipe Camara and Léo. I also include here my friends from the old and good 3rd floor: Zargos, Loch, Zé Pedro and Dudu. Life is nothing without good friends and a nice pint of beer.

To the EAC family who made me feel at home in Florianópolis: Bernardo, Jean, Lobato and Serjão. In extension, I would like to thank Tiagão and Augusto.

To EMBRAER engineers, Lobão, Rudner and Maicon for the opportunity to work in the SILENCE project and for the technical discussions and knowledge shared.

I would like to thank Felipe Dutra and Leandro Oliveira for kindly sharing their knowledge on the use of PowerFLOW. To Exa Corporation engineers, Wouter van der Velden, André Ribeiro and Rafael Ihi for the support. An special thanks to Prof. Damiano Casalino for the technical support and to Leandro Rêgo, from TU Delft, for sharing the porous FWH surface geometry used in this dissertation.

I would like to thank Prof. César Deschamps, Prof. Júlio Cordioli and Dr. Victor Rosa for the discussions and suggestions on this document.

Last but not least, I would like to thank the Laboratory of Vibrations & Acoustics and all the friends I made there during this period of my life. UFSC and EMBRAER/FINEP are also acknowledge for the financial support and for all the learning opportunities.

It's all about the journey...
not the destination.

(Rick Sanchez)

RESUMO

Quando o motor é montado em uma aeronave, fontes adicionais de ruído são geradas devido à interação do jato de exaustão com os dispositivos hipersustentadores da aeronave, i.e. asa e *flaps*. O chamado efeito de instalação é observado como (1) um aumento do ruído em baixas frequências devido ao espalhamento acústico do campo próximo do jato e (2) redirecionamento do campo acústico em médias e altas frequências devido a efeitos de reflexão sonora. Neste trabalho, propõe-se o uso de um modelo computacional para investigar o ruído de instalação. Para tanto, é considerada a interação entre um jato subsônico e uma placa plana. As simulações foram realizadas em um *solver* comercial de simulação de largas escalas baseado no Método de Lattice-Boltzmann (LBM). A predição do ruído em campo distante é obtida por meio do método de Ffowcs Williams & Hawkings (FWH). Inicialmente, uma análise de validação foi conduzida em um modelo computacional de um jato isolado, a fim de avaliar a influência da resolução da malha sobre os resultados fluidodinâmicos e acústicos. Os resultados acústicos em campo distante foram validados através de medições realizadas na bancada experimental de jatos, localizada no Laboratório de Vibrações e Acústica (LVA), da Universidade Federal de Santa Catarina (UFSC), Brasil. Posteriormente, o modelo numérico foi empregado para investigar alguns aspectos fundamentais relacionados ao efeito da instalação, tais como: (1) a influência da placa sobre o campo aerodinâmico do jato; (2) caracterização do campo de pressão incidente sobre a placa; (3) o efeito de instalação sobre o ruído em campo distante; e (4) contribuição da placa para o ruído em campo distante.

Palavras-chave: Aeroacústica, Ruído de Jato, Ruído Aeronáutico, Interação Fluído-Estrutura, Método de Lattice-Boltzmann.

UMA INVESTIGAÇÃO COMPUTACIONAL SOBRE O RUÍDO DE INTERAÇÃO JATO-PLACA UTILIZANDO O MÉTODO DE LATTICE-BOLTZMANN

Introdução

O ruído aeronáutico tornou-se um tópico importante no contexto urbano devido à crescente quantidade de residências perto de aeroportos e o aumento contínuo do tráfego aéreo. Buscando mitigar os efeitos adversos nas comunidades próximas a aeroportos, diversas medidas tem sido propostas pelas autoridades de aviação, incluindo restrições sobre o tipo de operação e tamanho da aeronave, planejamento de rotas e a certificação de aeronaves. O procedimento de certificação envolve a medição dos níveis de ruído em três pontos de referência distintos e uma métrica chamada *Effective Perceived Noise Level* (EPNL), a qual quantifica o incômodo humano ao ruído aeronáutico. O procedimento de certificação requer que o EPNL não exceda um certo nível cumulativo entre os três pontos de referência. Dessa forma, a redução de ruído tornou-se um tópico importante no projeto de aeronaves.

Neste contexto, o efeito de instalação sobre o ruído do jato é um problema relevante para a indústria aeronáutica uma vez que mecanismos adicionais de geração de ruído são introduzidos quando um motor é montado em uma aeronave. O efeito de instalação ocorre devido à interação do jato com os dispositivos hipersustentadores da aeronave, i.e. asa e *flaps*, sendo observado como (1) um aumento do ruído em baixas frequências devido ao espalhamento acústico do campo próximo do jato e (2) redirecionamento do campo acústico em médias e altas frequências devido a efeitos de reflexão sonora.

Objetivos

Este trabalho tem como objetivo principal o estudo de aspectos fundamentais relacionados ao efeito de instalação utilizando um *software* comercial de simulação computacional baseado no Método de Lattice-Boltzmann. Para tanto, é considerada a interação entre um jato subsônico e uma placa plana. Para alcançar este objetivo, propõe-se: (i) investigar o quão preciso é o modelo computacional para a previsão do ruído do jato e, (ii) avaliar como a placa modifica os campos fluido-dinâmico e acústico para diferentes configurações de instalação.

Método Numérico

O *software* comercial de fluido-dinâmica computacional PowerFLOW, versão 6.0beta, é utilizado para realizar as simulações de um jato subsônico, emitido por um bocal circular (SMC000), em diferentes configurações de instalação. O pacote computacional emprega um método híbrido para simular fluídos em altas velocidades subsônicas, o qual envolve um esquema tridimensional baseado no Método de Lattice-Boltzmann (LBM) e um modelo de turbulência para levar em consideração as escalas de turbulência não resolvidas pela malha computacional. O método é intrinsecamente transiente e compressível, o que o torna particularmente adequado para simulações aeroacústicas. A predição do ruído em campo distante é obtida por meio do método de Ffowcs Williams & Hawkings (FWH).

Análise de Validação: Jato Isolado

Uma análise de validação foi conduzida em um modelo computacional de um jato isolado. Buscou-se avaliar a influência da malha computacional sobre os resultados fluido-dinâmicos e acústicos. Para tal, foram avaliadas três resoluções de malha diferentes. Inicialmente, a validação dos resultados fluido-dinâmicos foi realizada por meios de comparação dos resultados do campo médio do escoamento com resultados disponíveis na literatura.

Na sequência, foram avaliados os resultados computacionais de ruído em campo distante, os quais foram validados através de experimentos realizados na bancada experimental de jatos, localizada no Laboratório de Vibrações e Acústica (LVA), da Universidade Federal de Santa Catarina (UFSC), Brasil. Primeiramente, problemas relacionados ao uso da técnica de FWH foram abordados. Em especial, a influência de parâmetros como a resolução espacial da malha da superfície porosa de FWH e a frequência de amostragem foram investigados. Por fim, o impacto da resolução da malha computacional sobre os resultados acústicos foi analisada, tendo como principal parâmetro de interesse os níveis de pressão sonora gerados pelo jato em campo distante.

Ruído de Interação Jato-Placa

O ruído de instalação é analisado através de um problema simplificado considerando a interação entre um jato subsônico e uma placa plana. A placa é posicionada em paralelo ao eixo do jato e posicionada em três diferentes distâncias radiais. Alguns aspectos fundamentais relacionados ao efeito de instalação foram investigados, tais como: (1) a influência da placa sobre o campo aerodinâmico do jato; (2) caracterização do campo de pressão incidente sobre a placa; (3) o efeito de instalação sobre o campo acústico em campo distante; e (4) contribuição da placa para o ruído em campo distante.

Conclusões

O presente trabalho buscou avaliar o uso de um modelo computacional baseado no método de Lattice-Boltzmann para a investigação do efeito de instalação no ruído gerado por um jato subsônico. Buscando avaliar as limitações do modelo computacional, foi realizada uma análise de validação no caso de um jato isolado. Em geral, os resultados mostraram que o modelo computacional apresenta pouca sensibilidade a resolução da malha, principalmente com relação aos resultados acústicos. No entanto, os resultados fluido-dinâmicos mostraram-se sensíveis a resolução de malha uma vez que somente o modelo com resolução *fine* foi capaz de predizer satisfatoriamente os níveis de turbulência verificados experimentalmente.

Em geral, a investigação sobre o ruído de interação jato-placa levou as seguintes conclusões: (1) para as configurações de instalação avaliadas, a placa não altera significantemente o campo aerodinâmico do jato; (2) a placa interage predominantemente com um campo de pressão caracterizado por um regime hidrodinâmico linear que possui alta energia em baixos números de Strouhal; (3) verificou-se que o espalhamento acústico do campo próximo do jato é o principal mecanismo responsável pelo aumento do ruído em baixas frequências, e que este fenômeno é dependente do número de Strouhal e da distância radial da placa; (4) o modelo computacional é capaz de predizer satisfatoriamente o ruído de instalação em campo distante utilizando a abordagem de FWH, e (5) o ruído de instalação pode ser decomposto entre as contribuições de ruído gerado pelo jato isolado e das flutuações de pressão incidentes na placa.

ABSTRACT

When an engine is mounted on an aircraft, additional noise sources are generated due to the close integration of the jet exhaust nozzle and the aircraft high-lift devices (HLD), i.e. wing and flaps. The so-called installation effects are observed as (1) a low-frequency augmentation on the far-field noise due to the scattering of the jet near-field by the HLD and (2) as shielding effects at mid- and high-frequencies due to the reflection of the sound waves at the HLD. In this work, the use of a computational model is proposed to investigate some fundamental aspects of the installation noise by considering the interaction between a subsonic jet and a flat plate. The simulations are conducted using a commercial Large-Eddy flow solver based on the Lattice-Boltzmann Method (LBM). The far-field acoustic prediction is obtained using the Ffowcs Williams & Hawkings (FWH) integral formulation. Initially, a validation analysis of the computational model of an isolated jet is conducted to assess the influence of the grid resolution on the flow and acoustic predictions. The far-field acoustic results are validated by experiments conducted in the jet rig located at the Laboratory of Vibrations & Acoustics (LVA) of the Federal University of Santa Catarina (UFSC), Brazil. Thereafter, the numerical model is employed to investigate some aspects concerning the installation effect, such as: (1) the influence of the plate on the jet flow; (2) characterization of the pressure field incident upon the plate; (3) the installation effect on the acoustic far-field and (4) the contribution of the plate to the far-field noise.

Keywords: Aeroacoustics, Jet Noise, Aircraft noise, Fluid-Structure Interaction, Lattice-Boltzmann method.

LIST OF FIGURES

LIST OF TABLES

LIST OF ACRONYMS

BC	Boundary Condition
BGK	Bhatnagar-Gross-Krook collision term model
BL	Boundary Layer
BPF	Blade Pass Frequency
BPR	Bypass ratio
CAA	Computational Aeroacoustics
CFD	Computational Fluid Dynamics
EPNL	Effective Perceived Noise Level
EASA	European Aviation Safety Agency
FDM	Finite Difference Method
FEM	Finite Element Method
FFT	Fast-Fourier Transform
FVM	Finite Volume Method
FWH	Ffowcs-Williams & Hawkings
HLD	High-Lift Devices
HBR	High-Bypass ratio
HWA	Hot-Wire Anemometry
ICAO	International Civil Aviation Organization
JAR	Jet Acoustic Rig
JSI	Jet Surface Interaction
JSR	Jet Surface Reflection
LBM	Lattice-Boltzmann Method
LBE	Lattice-Boltzmann Equation
LBR	Low-Bypass ratio
LEE	Linearized Euler Equations
LHS	Left Hand Side
LVA	Laboratory of Vibrations and Acoustics
NPR	Noozle Pressure Ratio
OASPL	Overall Sound Pressure Level
PSE	Parabolized Stability Equations
RHS	Right Hand Side
RNG	Renormalization Group Theory

SEL	Sound Exposure Level
SMC	Small Metal Chevron
SP	Set point according to Bridges and Brown [65]
SPL	Sound Pressure Level
SDA	Santos Dumont Airport
TE	Trailing Edge
UFSC	Federal University of Santa Catarina
VR	Variable Resolution
VLES	Very Large-Eddy Simulation

LIST OF SYMBOLS

Latin Symbols

(x, y, z)	Cartesian coordinate system	
$(x_\mathrm{s}, y_\mathrm{s}, z_\mathrm{s})$	Cartesian coordinate system based on the plate's TE	
$\mathrm{St}_{D_\mathrm{J}}$	Strouhal number	
Re_J	Reynolds number	
A_B	Anechoic buffer factor	
B_B	Anechoic buffer factor	
C_i	Collision operator for the i-th direction	
c_∞	Ambient sound speed	[m/s]
C_s	Plate's chord length	[m]
C_μ	Closure coefficient	
C_{ε_1}	Closure coefficient	
C_{ε_2}	Closure coefficient	
D_J	Nozzle diameter	[m]
f	Frequency	[Hz]
f_i^eq	Local equilibrium function for the i-th direction	
f_i	Density distribution function for the i-th direction	
f_min	Minimum frequency	[Hz]
f_s	Sampling frequency	[Hz]
h	Plate's radial distance to the jet centerline	[m]
h_s	Plate's thickness	[m]
k	Acoustic wavenumber	[m^{-1}]

L	Characteristic length-scale	[m]
L_{D}	Computational domain edge length	[m]
L_{FWH}	FWH surface length	[m]
L_{s}	Plate's spam length	[m]
M_{∞}	Free-stream Mach number	
$M_{\mathrm{a_{ref}}}$	Reference acoustic Mach number	
M_{a}	Acoustic Mach number	
M_{c}	Source convection Mach number	
M_{J}	Jet Mach number	
N	Number of time-samples	
N_{ppw}	Number of points per wavelength	
p'	Pressure fluctuation	[Pa]
P_0	Stagnation pressure	[Pa]
P_{∞}	Ambient pressure	[Pa]
P_{ref}	Reference pressure	[Pa]
R	Gas constant	[J/mol K]
r_0	Distance between a turbulent eddy and the surface TE	[m]
r_{inner}	Anechoic buffer inner radius	[m]
r_{lip}	radial distance from the nozzle lipline	[m]
r_{out}	Anechoic buffer outer radius	[m]
s	Surface characteristic length scale	[m]
S_{pp}	Pressure power spectrum	[Pa^2]
S_{ij}	Strain rate	
T	Fluid temperature	[K]
t	Time	[s]

T_0	Stagnation temperature	[K]
T_∞	Ambient temperature	[K]
t_a	Acquisition time	[s]
T_J	Jet temperature	[K]
t_s	Total simulation time	[s]
t_t	Transient time	[s]
u	Fluid velocity	[m/s]
u'_max	Maximum velocity fluctuation	[m/s]
$U(t)$	Instantaneous jet velocity	[m/s]
u'	Velocity fluctuation	[m/s]
U_J	Jet exit mean velocity	[m/s]
U_c	Eddy convection velocity	[m/s]
U_f	Free-stream velocity	[m/s]
U_slip	Fluid velocity at slip surface	[m/s]
w_i	Discrete velocity weight factor for the i-th direction	
W_D	Sound power of dipole noise sources	[W]
W_Q	Sound power of quadrupole noise sources	[W]
x_c	Potential core length	[m]
x_te	Plate's TE axial distance to the nozzle exit	[m]
X_W	Witze's potential core length	[m]
NPR	Nozzle pressure ratio	
OASPL	Overall sound pressure level	[dB]
SPL	Sound pressure level	[dB]
$\mathrm{SPL_c}$	Corrected sound pressure level	[dB]
$\mathrm{St_{min}}$	Minimum Strouhal number	

Greek Symbols

α_{W}	Witze's constant	
β_{s}	Acquisition time factor	
β_{T}	Closure coefficient	
Δf	Frequency resolution	[Hz]
Δl_{cups}	FWH surface end caps distance	[m]
Δt	Time-step	[s]
Δx	Minimum grid element size	[m]
Δx_{FWH}	FWH surface grid resolution	[m]
δ_{ij}	Kronecker's delta	
$\eta(\theta)$	Angle correction factor	
η_0	Closure coefficient	
η_{T}	Swirl correction factor	
γ	Ratio of specific heats	
λ	Acoustic wavelength	[m]
μ	Dynamic viscosity	[Pa s]
ν	Kinematic viscosity	[$\mathrm{m^2 s^{-1}}$]
ν_{T}	Eddy viscosity	[$\mathrm{m^2 s^{-1}}$]
ω	Angular frequency	[rad/s]
ϕ	Azimuthal angle	[deg]
ρ	Fluid density	[$\mathrm{kg/m^3}$]
ρ_∞	Ambient fluid density	[$\mathrm{kg/m^3}$]
ρ_{J}	Jet density	[$\mathrm{kg/m^3}$]
σ	Closure coefficient	

τ	Relaxation time	
τ_{eff}	Effective relaxation time	
τ_{ij}	Stress tensor	[Pa s]
θ	Polar angle	[deg]
ξ_i	Discrete particle velocity for the i-th direction	

Other Symbols

$(.)'$	Fluctuating quantity
$\langle . \rangle$	Time-averaged quantity
$\partial(.)$	Partial derivative
$\tilde{(.)}$	Complex quantity
$(.)^*$	Complex conjugate
D(.)	Material derivative

CONTENTS

1 INTRODUCTION

1.1 Aircraft noise

Aircraft noise has become an important topic in the urban context due to the growing amount of residences near airports (see Figure 1.1a) and the continuous increase of the air traffic. Figure 1.1b gives an perspective of the noise levels in which the communities surrounding the Santos Dumont Airport (SDA), in the city of Rio de Janeiro, Brazil, are exposed. The noise map is expressed in terms of A-weighted sound pressure levels representative of take-off and landing procedures performed during the day period (7am - 10pm). The noise map show that the residences near the SDA are exposed to noise levels up to 60 dBA for the assessed period.

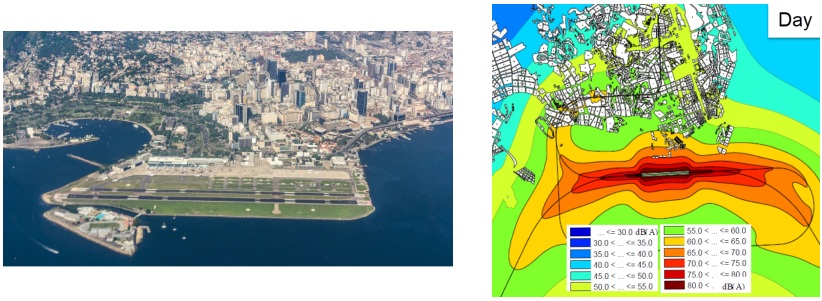

(a) (b)

Figure 1.1 – Santos Dumont airport, Rio de Janeiro, Brazil: (a) top view and (b) noise map. Source: (a) <www.travelandleisure.com> and (b) adapted from Sirotto et al. [1].

Several studies attribute long-term exposure to aircraft noise to adverse health problems [2, 3, 4] and, as a consequence, some countermeasures have been proposed by the aviation authorities. Some of the measures adopted include restrictions on the noise emission levels, on the type of operation and size of the aircraft and route planning.

In the early 1970s, aircraft noise regulations were proposed by the International Civil Aviation Organization (ICAO) (document 9501 - annex 16 [5]) as an attempt to mitigate the excessive aircraft noise levels around airports. The certification process involves measuring

noise levels at three distinct reference points (take-off, sideline and approach) and a metric called EPNL[1], which quantifies the human annoyance to aircraft noise. The regulation requires that the EPNL does not exceed a certain cumulative level for the three reference points. Even though a significant noise reduction has been achieved throughout the years, more stringent regulations are expected in the future years as aircraft noise remains a significant cause of annoyance and adverse reactions by the communities living near airports.

Much of the reduction in aircraft noise emissions achieved over the years is a direct consequence of the technological advances on the design of the propulsion system. In the first turbojet and low-bypass ratio (LBR) turbofan powered aircraft, the jet engine noise was dominant over the total noise emitted by an airplane. In modern aircraft, the use of high-bypass (HBR) engines led to a significant reduction of the jet noise contribution. In this type of propulsion system, a mass of cold, slow air flows through a bypass duct, allowing the jet velocity to be reduced without compromising the resulting thrust. As a consequence, the jet noise is reduced, as explained by Lighthill's eighth power law (see Appendix A.1 for more details), and the fan noise became the most relevant noise source in modern aero-engines (see Figure 1.2). Figure 1.3 shows the progress in noise reduction achieved along the years due to the increase of the engine's bypass-ratio (BPR[2]).

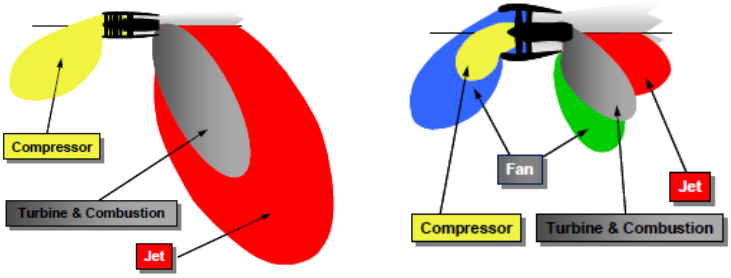

(a) Low-bypass ratio engine. (b) High-bypass ratio engine.

Figure 1.2 – Turbofan engine noise sources: (a) typical 1960s design versus (b) modern design. Source: Astley et al. [6].

[1] Acronym for Effective Perceived Noise Level.
[2] The ratio between mass flow through the bypass and core of a turbofan engine.

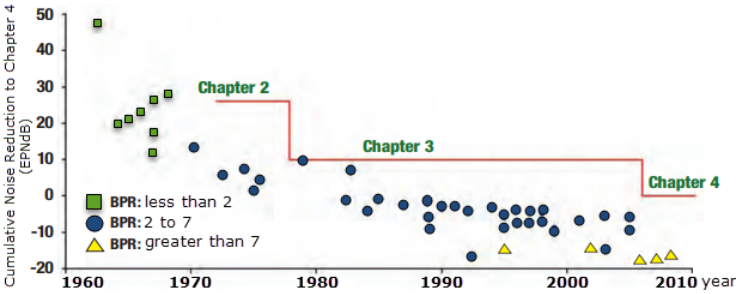

Figure 1.3 – Progress made in aircraft noise reduction over the years due to the increase of the engine BPR. Source: adapted from ICAO [7].

According to Zaporozhets et al. [8], a modern turbofan aircraft has distinct and complex noise sources (see Figure 1.4), which can be classified in two main categories:

- Airframe noise: generated due to aerodynamic interaction between the air flow and the aircraft's external structure (e.g. wing, fuselage, flaps and landing gear).

- Engine noise: related to the aircraft's propulsion system components such as turbo-machinery (fan, compressor, turbine), combustion and exhaust jet.

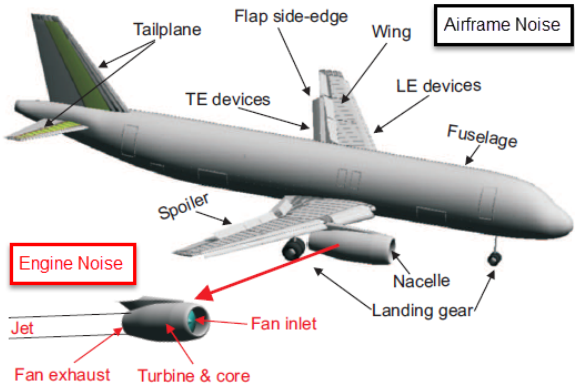

Figure 1.4 – Typical aircraft noise sources. Source: adapted from Merino [9].

The contributions from airframe and engine noise are highly dependent on the flight procedure. During the approach (see Figure 1.5a), the noise contributions from the engine components and the elements associated with the airframe have almost the same relevance. In the other hand, during the acceleration on the ground at take-off, the dominant noise sources are associated with the engine components (see Figure 1.5b). With the advent of HBR engines, the fan has a considerable contribution for both take-off and landing procedures.

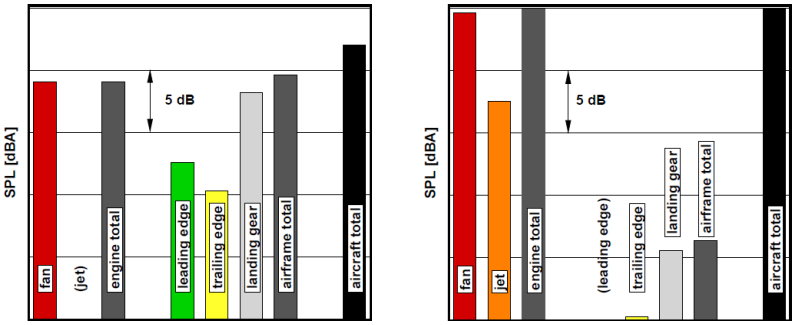

(a) Approach. (b) Take-off.

Figure 1.5 – Noise source breakdown for an Airbus A319. Source: adapted from Bertsch [10].

As observed in Figure 1.5, the major source of aircraft noise is attributed to the propulsion system components inside the engine nacelle including fan, compressor, combustor and turbine noise (see Figure 1.6). Each one of these engine components are noise sources with distinct spectral characteristics. Rotating machinery like fan, compressor and turbine generate both tonal and broadband noise. Besides BPF related tones, shocks created by the supersonic relative speed of a inlet flow to the fan blade originates different tones at harmonics of the shaft rotation frequency, known as buzz-saw noise.

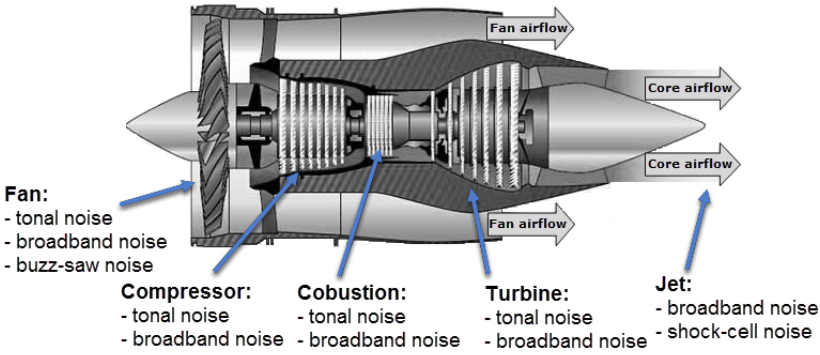

Figure 1.6 – Main components of a turbofan engine and their respective noise characteristics. Source: adapted from <www.flight-mechanic.com>.

Broadband noise is generally due to turbulent flow impingement on solid surfaces as the fan's rotor-stator or blades, for example, and occurs in all engine's components. The exhaust jet at the engine's rear also creates a broadband noise when the hot, fast core, and the slow, cold bypass flows mix with each other and the ambient air stream. Moreover, jet flows in supersonic regime may produce tonal shock-associated high frequency noise in addition to the broadband mixing noise.

Despite the noise reduction promoted by HBR engines, the jet exhaust remains one of the main noise sources in aircraft, specially during take-off. Among various strategies developed to mitigate jet noise (see the work of Casalino et al. [11] for a complete review), the use of chevron nozzles is nowadays employed in commercial aircraft since it promotes an effective far-field noise reduction without significant aerodynamic compromises. Chevron nozzles increase jet mixture by breaking coherent large scale instabilities that would generate low-frequency noise, promoting a shift of the jet noise spectral signature to higher frequencies. As a consequence, a reduction on the EPNL levels is obtained as high frequencies suffers more atmospheric attenuation.

1.2 Installation effects

When the propulsion system is installed in an aircraft, additional mechanisms of noise generation are introduced over the original acoustic signature of an isolated jet engine. Considering the jet noise as the primary source of noise, two levels of installation effects may occur:

- Acoustic installation effects: sound waves are reflected or scattered by the aircraft high-lift devices (HLD), i.e. wing and flaps, changing the original characteristics of the noise source;
- Installation noise sources: additional noise sources are generated due to the interaction of the aircraft HLD with the jet flow.

The installation effects are particularly relevant in under-wing mounted HBR configurations (see Figure 1.7) where the jet exhaust is significantly close to the aircraft HLD. In this case, three main mechanisms of noise generation can be identified (see Figure 1.8): (1) reflection and scattering of acoustic waves on the wing and fuselage; (2) scattering of the jet near-field due to jet-wing interaction and (3) jet-flap interaction source. Figure 1.9 helps us to have an appreciation of the impact of the installation effect on the far-field noise of an isolated jet engine.

Figure 1.7 – Underwing mounted turbofan engine. Source: <www.aircraftnerds.com>.

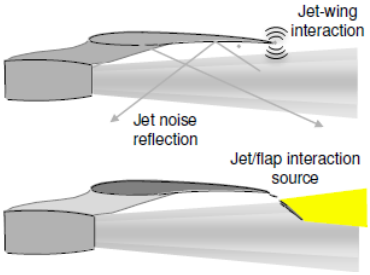

Figure 1.8 – Installation noise mechanisms. Source: adapted from Astley et al. [6].

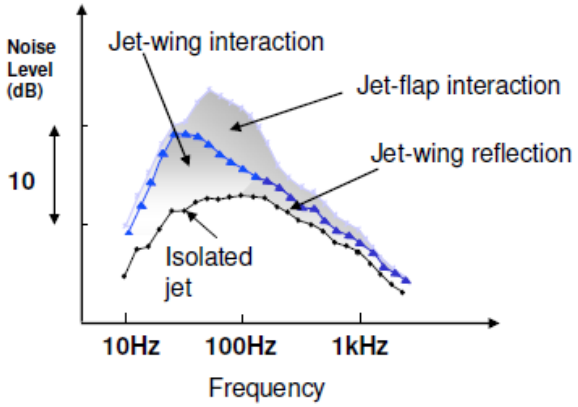

Figure 1.9 – Jet noise installation effect: typical noise spectra at a fly-over position. Source: Astley et al. [6].

As can be verified in Figure 1.9, the main adverse effect due to the integration of the engine on the aircraft is an augmentation above the noise generated by an isolated jet at the low frequencies. This effect is attributed to two mechanisms: (1) jet-wing interaction and (2) jet-flap interaction. The first is associated with the scattering of the hydrodynamic fluctuations produced by the jet shear-layer at the trailing edge of the wing; the second is due to the generation of additional aerodynamic noise sources by the interaction of the jet flow with a deployed flap. In general, the closer the jet exhaust is to the aircraft HLD, the more intense are these effects. Moreover, the reflection of the jet noise by the wing is observed as a increase in the mid and high frequency range of the noise spectrum.

1.3 Motivation and objectives

Noise reduction has become an important topic in aircraft design because increasingly stricter regulations on sound levels were imposed to civil aviation throughout the years. In this context, the installation effect on jet noise is a relevant problem for the aviation industry as additional noise mechanisms are introduced when an engine is mounted on an aircraft. Nowadays, most of the noise prediction tools used by the industry lies on semi-empirical models limited to experimental databases, so it is important to develop and assess prediction tools capable to estimate the installation noise for the most diverse configurations.

With the development of reliable numerical schemes and increase in computational resources, numerical models are currently becoming a feasible tool to assess complex engineering problems with industrial applications. This is specially likely in the case of jet noise installation effects as information on both jet flow and acoustic fields are required to better understand the noise generation mechanisms involved in this phenomena. In this sense, computational simulations are advantageous over experimental measurements since they are less time consuming and provides flow and acoustic data without any instrumentation constraints.

The objective of this work is to investigate fundamental aspects related to the sound generation mechanisms involved in the jet noise installation effect using the Lattice-Boltzmann based commercial software PowerFLOW, version 6.0beta. The interaction between a single-stream, subsonic, cold jet issued by a round nozzle with a flat plate is considered. To achieve this objective, the following research questions are posed:

1. How accurate is the computational model for the prediction of jet noise?

    - What is the flow and acoustic results sensitivity to the grid resolution?
    - What is the requirements for an accurate computation of the far-field noise?

2. How does the plate modify the jet flow and acoustics for different installation configurations?

    - Does the plate alter the hydrodynamic field of the jet?
    - What is the regime of the pressure fluctuations incident on the plate?
    - How does the plate modify the far-field acoustic directivity of the jet noise?

1.4 Document outline

This dissertation is organized as follows:

- **Chapter 2:** provides a background on relevant topics related to the aerodynamic noise of subsonic jets, such as: (1) the aerodynamics of jet flows (Section 2.1); (2) the fundamental aspects regarding sound generation by subsonic jets (Section 2.2); (3) theory background and experimental observations concerning jet-surface interaction noise (Section 2.3) and (4) review of computational aeroacoustics and the use of the Lattice-Boltzmann method for jet noise prediction (Section 2.4).

- **Chapter 3:** describes the numerical procedures employed in this work for the simulation of jet noise, including (1) a description of the numerical scheme adopted by the commercial software PowerFLOW (Section 3.1) and (2) a description of the computational model (Section 3.2).

- **Chapter 4:** presents the validation analysis of the computational model of an isolated jet. Both flow and acoustics results are assessed for different grid resolutions and the requirements regarding the use of a permeable Ffowcs Williams & Hawkings surface for the prediction of far-field noise are investigated.

- **Chapter 5:** presents a computational investigation regarding the fundamental aspects involved in the jet-plate interaction noise phenomena. In this context, the numerical model is employed to (1) assess the influence of the plate on the jet flow (Section 5.1); (2) characterize the jet near-field and the regime of the pressure fluctuations incident on the plate (Section 5.2); (3) assess the installation effect on the far-field (Section 5.3) and (4) investigate the contribution of the plate to the far-field noise (Section 5.4).

2 BACKGROUND THEORY

This chapter introduces the definitions and terminologies used throughout this work for the discussion of the physical concepts behind aerodynamic noise generated by subsonic jet flows. Section 2.1 provides a brief description on the aerodynamic aspects of jet flows. Section 2.2 introduces some of the fundamental aspects regarding sound generation by subsonic jets. Furthermore, Section 2.3 discusses the theoretical background and experimental observations found in the literature concerning jet-surface interaction noise. Finally, Section 2.4 presents a review of computational methods for the aeroacoustic simulation of jet flows.

2.1 Aerodynamics of subsonic jet flows

A jet flow occurs when a pressurized fluid inside a duct is discharged in an external environment through an orifice or nozzle. This particular type of free shear-flow is found in many natural and industrial environments such as in discharges from chimneys or high-pressure hoses, the jet flame expelled by a burning gas and the exhaust of an turbo-fan aircraft propulsion system, and can be classified according to some of its properties.

One of the main characteristics of jets concerns whether the flow regime at the nozzle exit is laminar or turbulent. An indicator of the flow regime is the jet Reynolds number, $\mathrm{Re_J}$, which is defined as the ration between inertial forces (related to convective effects) to the viscous forces, as

$$\mathrm{Re_J} = \frac{U_\mathrm{J} D_\mathrm{J}}{\nu}, \tag{2.1}$$

where U_J is the jet flow mean velocity at the nozzle exit, D_J is the nozzle diameter and ν is the fluid's kinematic viscosity. When the Reynolds number exceeds a certain value, the flow instabilities starts a transition process where the velocity fluctuations grows in a chaotic manner leading to the development of a fully turbulent flow.

The jet can be initially in laminar ($\mathrm{Re_J} < 1000$) or fully-turbulent ($\mathrm{Re_J} > 3000$) regime and the ambient fluid can be static or moving. Figure 2.1 shows the instabilities in an airstream issuing from a circular pipe with Reynolds number $1{\times}10^4$, whose are made visible through

the smoke wire technique. The jet is laminar as it leaves the nozzle (region I). As the jet flow interact with the quiescent, ambient fluid, a shear layer is formed due to Kelvin-Helmholtz instabilities, producing axisymmetric coherent structures in the form of vortex rings (region II). As the large-scale coherent eddies are advected by the mean flow and eventually collapses downstream, the jet flow becomes fully turbulent (region III).

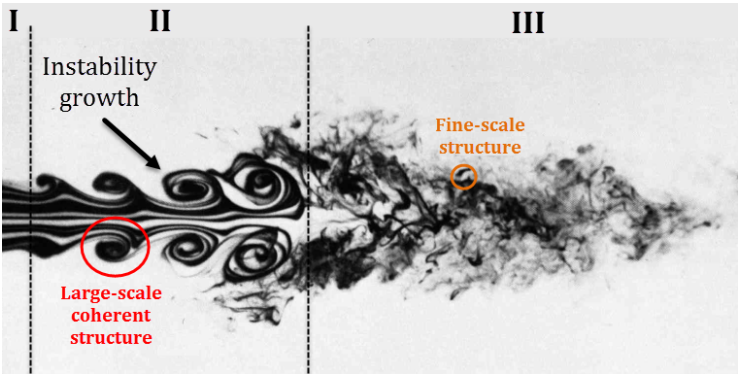

Figure 2.1 – Instabilities of an air stream issued from a circular tube with Reynolds number of $1{\times}10^4$. Source: adapted from Van Dyke [12].

Apart from the flow regime, a jet flow can be also categorized according to some of its characteristics, such as:

- Velocity: the ratio between the jet exit velocity, U_J and the ambient speed of sound, c_∞[1], gives the acoustic mach number $M_\mathrm{a} = U_\mathrm{J}/c_\infty$, which defines subsonic ($M_\mathrm{a} < 1$) and supersonic ($M_\mathrm{a} > 1$) jets;

- Temperature: the ratio between the ambient temperature, T_∞, and the jet flow temperature, T_J, is used to define cold ($T_\mathrm{J}/T_\infty < 1$), isotherm ($T_\mathrm{J}/T_\infty = 1$) and hot ($T_\mathrm{J}/T_\infty > 1$) jets;

- Fluid-stream: a jet can be composed by a single or dual (e.g. coaxial, co-planar) exhaust streams. In the later, the bypass and core exhausts interacts creating a single turbulent shear-layer;

[1] The ambient sound speed $c_\infty = \sqrt{\gamma R T_\infty}$ is calculated in relation to the ambient temperature T_∞, with constants $\gamma = 1.4$ and $R = 8.314$ kJ/kmol.K.

- Isolated and installed conditions refers to the presence of any solid objects that can interact with the aerodynamic or acoustic fields of the jet flow.

A brief overview on the aerodynamic aspects of subsonic, cold jet flows is given in the following sections. The books of Abramovich [13], Mathieu et al. [14], Pope [15] and Nieuwstadt et al. [16] are indicated here in case the reader needs more complete descriptions on the fluid mechanics of jet flows.

2.1.1 Turbulence characterization

Turbulence is a flow regime characterized by chaotic, stochastic property changes and, in general, is time-dependent, rotational, and three-dimensional. Turbulence arises due to the instability of laminar flow at large Reynolds number, where viscous effects are less important than convective effects.

A turbulent flow contain a broad range of scales of motion, which are physically observed as eddies[2], or whirls, with different time- and length-scales. Some of this structures have a length-scale in the order of the flow itself while others are much smaller. Thus, it is intuitive to think that the different scales of motion will produce different amounts of kinetic energy. Following the energy cascade concept postulated by Richardson [18], the turbulent kinetic energy is generated by some external force or hydrodynamic instabilities at a large-scale and is then transferred to smaller scales where it is dissipated into heat due to viscous processes. The smaller, dissipative scales of motion, also known as Kolmogorov scales, changes in size with fluid viscosity, becoming smaller with the increasing of the Reynolds number.

Since the macroscopic properties of the flow, such as velocity, pressure and density, fluctuates with time and space in an apparently random fashion, it is convenient to analyze turbulence by means of its statistical moments. Figure 2.2 illustrates a typical velocity signal of a subsonic, turbulent jet flow.

[2]Regions of the turbulence over which fluctuations of velocity are highly correlated [17].

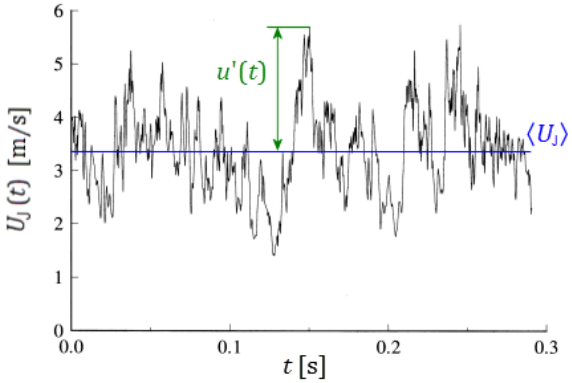

Figure 2.2 – Velocity measurement on the centerline of a turbulent jet. Source: adapted from Hilares [19].

As a starting point, a time-dependent, stochastic quantity can be decomposed into a mean value plus a fluctuation component. Hence, the instantaneous jet velocity, $U(t)$, at a given time, t, can be expressed as

$$U(t) = \langle U \rangle + u'(t), \tag{2.2}$$

where the time-averaged and fluctuating components are denoted by $\langle . \rangle$ and $(.)'$, respectively. Instantaneous quantities are obtained directly from the simulation as time-series functions that are represented at N discrete, evenly spaced time-samples, Δt. Having this in mind, the jet mean velocity is computed by

$$\langle U \rangle = \frac{1}{N} \sum_{j=0}^{N-1} U(t_j), \tag{2.3}$$

where $j = 0, 1, 2, ..., (N-1)$ timesteps and $t_j = j\Delta t$.

The fluctuation velocity, $u'(t)$, which is usually interpreted as representing the turbulence, can be estimated through the standard deviation, or root-mean-square (RMS), of the instantaneous velocity, as

$$u'(t) = \sqrt{\frac{1}{N} \sum_{j=0}^{N-1} (U(t_j) - \langle U \rangle)^2}. \tag{2.4}$$

2.1.2 Mean flow properties

As the jet leaves the nozzle, the diffusion of momentum between the expelled fluid and the quiescent medium gradually decelerates the high-velocity flow through air entrainment on its surroundings. This mixing process creates an axisymmetric annular turbulent shear-layer (also called the mixing-layer) between the moving an quiescent fluids that spreads as the jet develops downstream. Figure 2.3 illustrates the main regions of a turbulent jet flow. The length of those regions depends on the Reynolds number as well on the jet flow conditions.

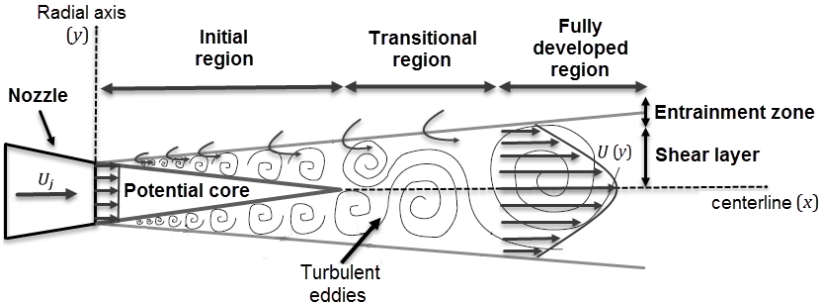

Figure 2.3 – Scheme illustrating the main regions of a free, turbulent jet flow. Source: adapted from Mclaughlin [20].

In the initial region, the mean velocity profile is tapered into a cone shape, called potential core, which is defined as the region where the jet flow is able to keep its initial exhaust velocity. The average axial length of the potential core for cold jets is about $4 \leq D_{\mathrm{J}} \leq 6$, depending on the mach number [21]. According to Cavalieri [22], the flow in the potential core can be assumed as irrotational, and thus allows the definition of a velocity potential. Moreover, the mixing process in the initial region triggers Kelvin-Helmholtz instabilities that grows as they are advected by the mean flow with an eddy convection velocity[3], $U_{\mathrm{c}} = 0.62U_{\mathrm{J}}$ [23]. With the end of the potential core, the uniform growth of the shear-layer ceases and the jet passes through a transition region between an annular mixing layer to a region where the flow becomes fully-turbulent.

[3]This estimative is relative to U_{c} at the center of the shear-layer, i.e. on the jet nozzle lipline.

2.1.3 Velocity profiles

The mean velocity and the mean square turbulence velocity profiles variation across the jet shear-layer are illustrated by Figure 2.4. It can be seen that most of the turbulent energy is confined to a narrow region at the center of the shear-layer.

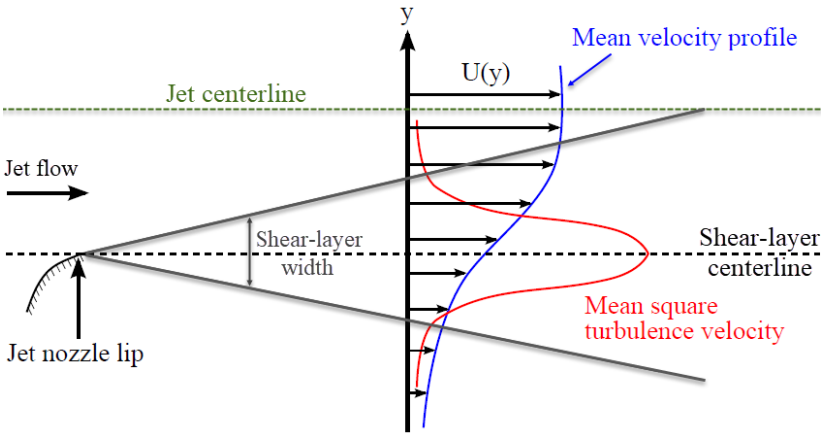

Figure 2.4 – Profiles of mean velocity and root-mean-squared fluctuation velocity. Source: adapted from Lawrence [24].

Immediately after being expelled by the nozzle, the jet mean velocity radial profile is practically uniform, presenting a top-hat like profile (see Figure 2.5a). As the jet develops, the mean velocity varies radially, originating a bell shape velocity profile. As can be seen in Figure 2.5b, the velocity fluctuations are maximum inside the shear-layer and much smaller inside the potential core and in the entrainment regions. Downstream the end of potential core occurs the turbulence intensity peak, which can be fairly approximated by $u'_{\max} \approx 0.16 U_{\mathrm{J}}$ [25].

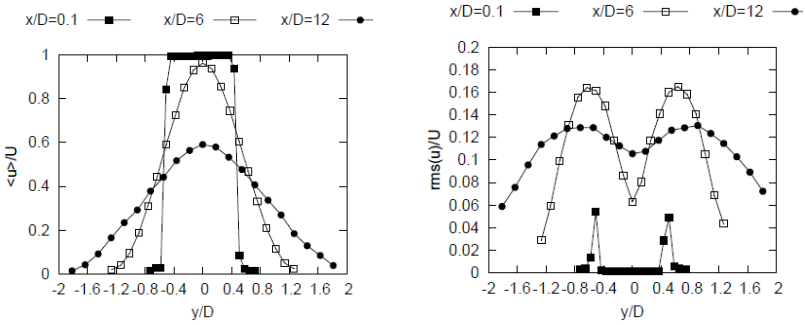

(a) Mean axial velocity.

(b) Turbulent intensity.

Figure 2.5 – Comparison of mean axial velocity radial profiles at different axial distances. Source: Cavalieri [22].

Regarding the jet's centerline behaviour, the mean velocity is decreased after the potential core and the turbulent intensity presents the opposite trend. Bridges & Wernet [26] showed that the centerline velocity profiles for jets with different mach conditions collapses if scaled by the potential core length, x_c. The authors confirmed the universal fit for mean centerline values proposed by Witze [27], which derived an empirical relation to predict the decay of the mean velocity along the jet centerline, given by

$$\frac{U}{U_J} = 1 - e^{\alpha_W/(1-x/X_W)}, \tag{2.5}$$

followed by an estimation of the jet potential core length, X_W, as

$$\frac{X_W}{D_J} = \frac{4.375(\rho_J/\rho_\infty)^{0.28}}{1 - 0.16M_J}, \tag{2.6}$$

where ρ_J and ρ_∞ are the jet's and ambient density, respectively, and $\alpha_W = 1.43$. Figure 2.6 presents results of the axial development of mean and fluctuation velocity fields for jets with different characteristics, i.e. with distinct temperature ratios and velocities. The results shows that the jet scaling by the potential core length is universal since the results are fairly collapsed for all cases. Moreover, the authors observed that the mean velocity starts to decay at roughly $x/X_W = 1.3$ for all cases.

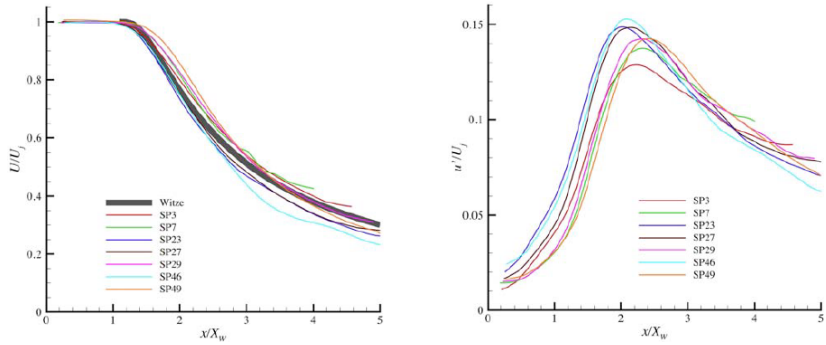

(a) (b)

Figure 2.6 – Centerline profiles of (a) mean streamwise velocity and (b) turbulent intensity for different jet flow conditions covering a wide range from subsonic heated and unheated jets to supersonic heated ones. Source: Bridges & Wernet [26].

2.2 Aeroacoustics of subsonic jet flows

The aerodynamic noise generated by a subsonic jet is mainly attributed to the mixing process between the jet flow and the ambient fluid. Therefore, the characteristics of the acoustic field generated by jet flows are strongly connected to the turbulent field of the jet. In general, the turbulent eddies generated in this process vary significantly in size, growing progressively downstream of the nozzle and decaying in intensity as the velocity falls and the jet becomes fully turbulent. As theorized by Lighthill [28], the frequency of aerodynamic noise is inversely proportional to the size of the turbulent noise sources. Thus, high-frequency noise is generated by small-scale turbulence close to the nozzle while low-frequency noise is associated with large turbulent eddies present downstream the jet shear-layer. Figure 2.7 presents far-field sound pressure levels generated by single-stream, cold jets under different velocities for distinct polar angles[4]. The frequency axis is non-dimensionalized to a Strouhal number by the nozzle diameter and the jet exit velocity, which is defined as $\mathrm{St}_{D_\mathrm{J}} = fD_\mathrm{J}/U_\mathrm{J}$.

[4]The convention adopted defines the polar angles having the jet centerline as reference. Thus, lower angles refers to the direction downstream the jet flow while higher angles above 90° are positioned upstream the jet nozzle.

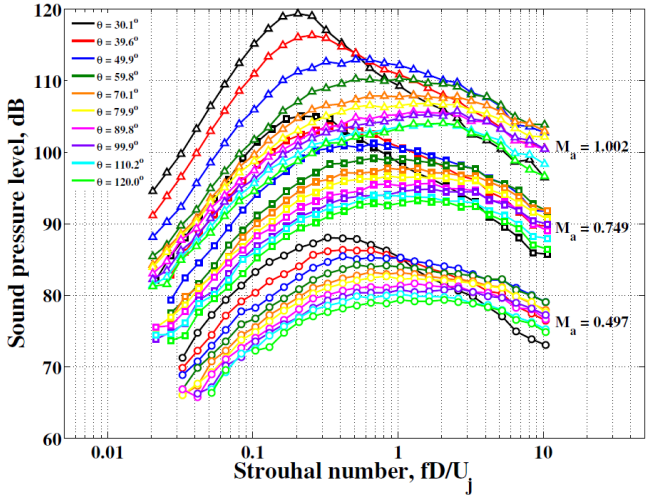

Figure 2.7 – 1/3 octave band far-field sound pressure levels of subsonic jet flows under different acoustic Mach numbers and polar angles. Source: Lawrence [24].

The downstream directivity of subsonic jets is clearly verified for low polar angles in Figure 2.7, especially for low Strouhal numbers. Cavalieri et al. [29] performed an experimental investigation on the polar directivity of subsonic jet flows and found that the low-frequency component downstream the jet is related to large-scale coherent flow structures forming a non-compact wavepacket source. Moreover, it is possible to observe in Figure 2.7 some of the main characteristics related to the far-field noise generated by subsonic jets:

- Jet noise presents a broadband character as no prominent tonal peaks are observed in the spectra;
- Different spectral shapes are verified at low and high polar angles as a consequence of the nature of the turbulent structures being convected by the jet mean flow;
- The sound pressure level magnitude increases proportionally to approximately the eight power of the jet flow velocity.

2.2.1 Pressure field characterization

Many studies have been devoted to the characterization of the pressure field generated by the velocity fluctuations of an turbulent jet flow [30, 31, 32, 33, 34]. As pointed by Howes [35], the analysis of the pressure field close to the jet plume is difficult as the microphone is subjected at the same time to pressure fluctuations induced by hydrodynamic turbulent structures, also referred to as "pseudo-sound", and pressure perturbations generated by acoustic waves. Tinney & Jordan [36] showed that is possible to isolate the hydrodynamic and acoustic pressure fields from the near-field of a coaxial jet based on their phase velocities in the wavenumber-frequency domain.

Savell [30] analyzed the sound pressure levels of a turbulent jet as a function of the radial distance away from the nozzle (see Figure 2.8) and observed that, when sufficiently further away from the jet flow, the intensity of the pressure fluctuations decay with the inverse square of the distance, which characterizes a far-field acoustic condition[5]. This way, the authors showed that is possible to determine the transition between the hydrodynamic, near-field and the acoustic far-field based on the decay rate of the pressure fluctuations with the radial distance.

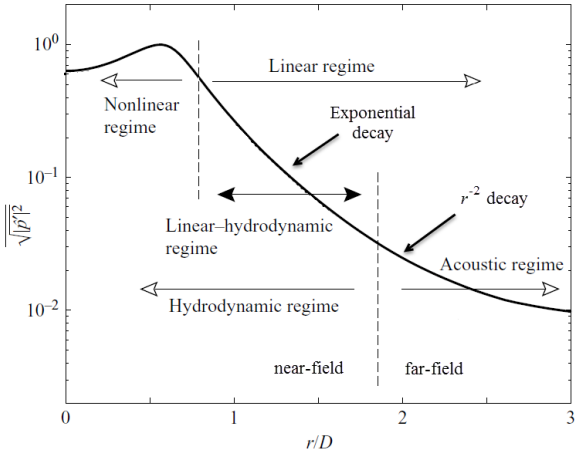

Figure 2.8 – Pressure regimes of a subsonic jet flow as a function of the radial distance. Source: adapted from Colonius & Suzuki [32].

[5]The acoustic far-field is defined as the region sufficiently far from the noise source so that the sound pressure level decays with the inverse of the squared distance.

As illustrated in Figure 2.8, the pressure field generated by a jet flow can be divided into two regimes: a non-propagating near-field and an acoustic regime associated with pressure fluctuations that propagates to the far-field with the speed of sound. Moreover, Colonius & Suzuki [32] identified two distinct hydrodynamic sub-regimes in the near-field: (a) a non-linear, rotational hydrodynamic regime associated with the turbulent field and (b) a linear, irrotational hydrodynamic regime associated with Kelvin-Helmholtz instabilities that decay exponentially with the radial distance.

Arndt et al. [37] observed that, due to differences in phase-velocity, the pressure regimes of an subsonic jet are better defined in terms of a non-dimensional acoustic wavenumber, kr_{lip}, where k is the acoustic wavenumber $k = \omega/c_\infty$ and r_{lip} is the radial distance from the nozzle lipline. The authors related the pressure fluctuations in the entrainment region of the jet to the turbulence energy spectrum using the unsteady Bernoulli equation and observed that the pressure fluctuations generated by turbulence within the inertial-subrange follows a exponential intensity decay $\propto (kr_{\mathrm{lip}})^{-20/3}$. This way, they verified that the transition between regimes is frequency dependent as the dividing line between near- and far-field takes place at $kr_{\mathrm{lip}} = 2$. This implies that acoustic pressure fluctuations can be observed at distances close to the jet flow. Figure 2.9 shows a typical spectrum measured in the vicinity of a turbulent, subsonic jet flow, illustrating the frequency-dependent behaviour of the pressure fluctuations.

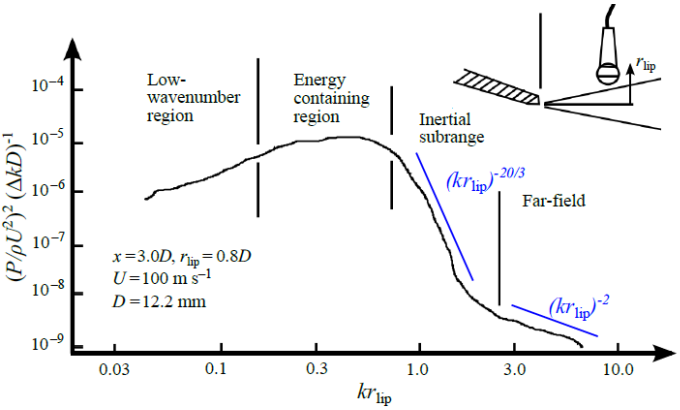

Figure 2.9 – Spectra illustrating all four regions of the pressure fluctuations generated by a turbulent jet according to Arndt et al. [37]. Source: Lawrence [24].

2.2.2 Sound directivity

Aerodynamic sound generation was first modeled mathematically by Lighthill [28], who rearranged the governing equations of fluid motion into an inhomogeneous wave equation (see Appendix A.1). The source term in Lighthill's equation (see Equation (A.1)), describes the sound generation by free turbulence in a quiescent medium as a distribution of quadrupole sources whose force per unit volume is given by the Lighthill tensor (see Equation (A.2)). In jet flows, the quadrupoles are moving acoustic sources as the turbulent structures are convected downstream by the mean flow. This leads to a directional sound radiation pattern that tends to radiate more noise in the direction which the sources are transported. The convective effect is more pronounced as the jet speed increases.

Additionally to the convection effect, sound refraction plays an important role on the sound radiation pattern of jet flows. Sound waves propagating within the shear-layer are refracted due to the highly nonuniform mean flow of the jet, which presents considerable velocity gradients between the centerline regions and the outer regions of the shear-layer. Figure 2.10 illustrates the refraction of an acoustic ray emitted by a point source, S, located within the mixing layer. As the convection velocity is lower in the outer region of the mixing layer (point A) and higher near the jet centerline (point B), the wavefront AB is bent outward the jet flow due to the sound speed gradients. This effect creates a cone of silence downstream of the jet flow since less noise is radiated in this direction. The relevance of the refraction effect increases for heated jets, as higher sound speed gradients within the jet shear-layer are expected.

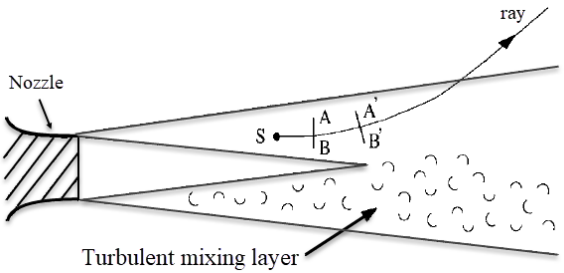

Figure 2.10 – Schematic illustrating sound refraction effects in the jet mixing layer. Source: adapted from Tam [38].

According to Ribner [39], the sound radiation pattern generated by a turbulent jet is composed by two distinct mechanisms. The first, called shear noise, is associated with the sound generated by the turbulence structures interacting with the mean shear flow while the second, called self noise, refers to the noise generated by the turbulence structures interacting with themselves. Figure 2.11 illustrates this concept. The (a) self noise produces a omnidirectional pattern whereas the (b) shear noise presents a dipole-like shape. The superposition of these two sound generation mechanisms generates an ellipsoid sound radiation pattern in which most of the sound is radiated along the jet axis. Combining these sound radiation mechanisms with the convective and refractive effects previously discussed, the overall sound radiation pattern of subsonic jet flows is verified to be highly directional downstream the mean flow.

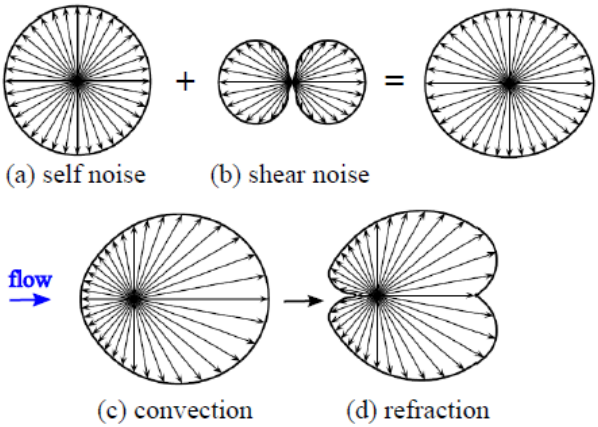

Figure 2.11 – Contribution of distinct sound radiation effects to the overall jet noise directivity pattern. Source: Lawrence [24].

2.2.3 Velocity dependency

Apart from describing aerodynamic sound, another relevant contribution of Lighthill's work regards the estimation of the order of magnitude of the far-field sound power generated by an turbulent jet. The so called Lighthill's eighth power law (see Appendix A.1 for more de-

tails) states that the far-field acoustic power of compact[6] quadrupole noise sources, W_Q, scales with the flow velocity as

$$W_Q \propto U_J^8. \tag{2.7}$$

Lighthill's eighth power law was confirmed experimentally by Lush [40] to provide a quite accurate estimation of the far-field noise generated by a cold subsonic jet at polar angle $\theta = 90°$. Figure 2.12, presents a compendium of overall sound pressure level results of cold, subsonic jet flows obtained at nine distinct small-scale rig facilities. The results confirms the dependence of the overall jet noise to the eighth power of the flow velocity and highlights that small-scale jet noise facilities are consistent in achieving this trend.

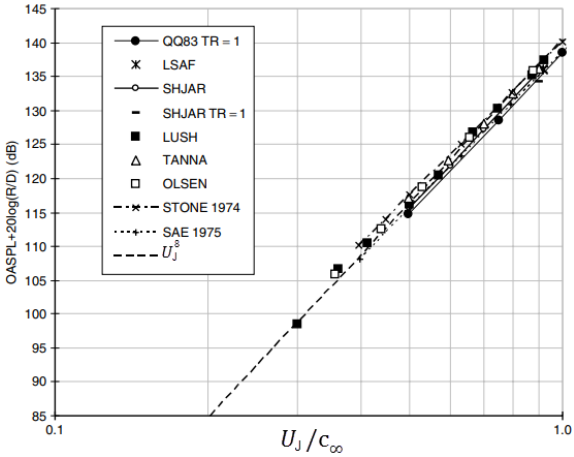

Figure 2.12 – Velocity dependence of jet noise: comparison of far-field, lossless, overall sound pressure levels for unheated jet flows under different mach numbers at polar angle $\theta = 90°$. Results obtained at nine different facilities. Source: adapted from Harper-Bourne [41].

Lighthill's eighth power law does not take into account the convective and refraction effects on the predictions of the jet noise. Thus, it only provides a good approximation for a polar angle of 90°, where convective and diffraction effects on the jet noise directivity pattern are less important. Lighthill recognized the importance of the source con-

[6] An acoustic compact source is defined as the noise source which generates sound with a much bigger acoustic wavelength, λ, than its characteristic length scale, L.

vection effect and proposed a a convective amplification factor as a final addition to the eighth power law, which now becomes also dependent on the polar angle, as

$$W_{\mathrm{Q}}(\theta) \sim \rho_{\infty} D_{\mathrm{J}}^{2} U_{\mathrm{J}}^{8} c_{\infty}^{-5} \underbrace{(1 - M_{\mathrm{c}} \cos\theta)^{-6}}_{\text{convective factor}}, \tag{2.8}$$

where M_{c} is the source convection Mach number (i.e. the mean flow velocity at the source position). This convective, or Doppler, correction term was later refined by Ffowcs-Williams [42] as $(1 - M_{\mathrm{c}} \cos\theta)^{-5}$.

Sirotto [43] observed experimentally that the increasing on the overall sound pressure indeed follows a linear slope increase trend as a function of the jet velocity. However, as can be verified in Figure 2.13, the angular coefficient is different for distinct polar angles. Following this observation, the author derived semi-empirical angular coefficients based on linear fitting procedure over the curves shown in Figure 2.13, whose can be used to correct Lighthill's eighth power law predictions for different polar angles. The angular coefficients are shown later on by Figure 4.9, where a velocity correction is employed to correct the far-field spectra obtained by the numerical model used in this work.

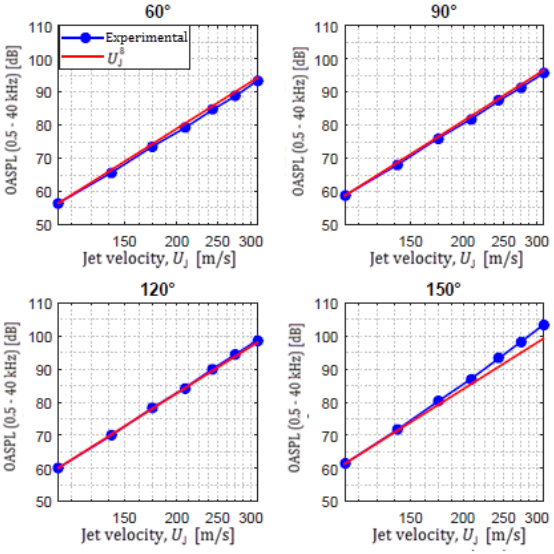

Figure 2.13 – Increase in OASPL with the jet exit velocity for different polar angles. Source: Sirotto [43].

2.3 Jet noise installation effects

As discussed in the introduction of this work, installation effects are an important topic for the aviation industry as the placement of the propulsion system on the aircraft brings adverse effects on the noise radiated by the engine itself. For practical reasons, small-scale models are usually employed to investigate this phenomena in academic laboratories, where the wing profile is approximated by an flat plate. Lawrence [24], investigated the reliability of such approximation by comparing the noise spectra obtained by two jets issued by single-stream, axisymmetric nozzles with different exit diameters under static condition ($U_\mathrm{f} = 0$) at $M_\mathrm{a} = 0.55$. Figures 2.14 depicts the setup configuration along with the results obtained for a fly-over observer position. The author stresses that the position of the wing trailing edge with respect to the jet nozzle is not completely identical for the two cases.

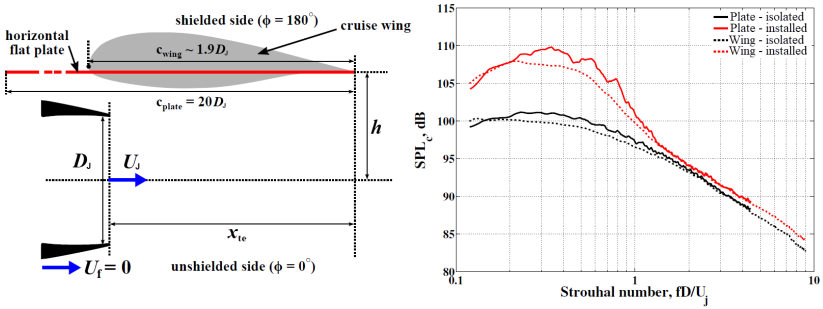

(a) Setup configuration.

(b) Far-field acoustic results at unshielded position.

Figure 2.14 – Read-across between installed jets under realistic (cruise wing) and simplified (flat plate) configurations ($h/D_\mathrm{J} \approx 0.76$; $x_\mathrm{te}/D_\mathrm{J} \approx 2$). Source: adapted from Lawrence [24].

Figure 2.14 shows that, despite the differences on the solid surfaces geometry and positioning, the approximation of the installed problem using a flat plate is plausible as an good agreement between the two cases is verified for the far-field acoustic results. This gives confidence on the investigation conducted in this work as a flat plate is used to assess the installation effects on jet noise.

Throughout the literature, many studies employ a flat plate to investigate the noise generation mechanisms behind the jet noise installation effect phenomena. Head & Fisher [44], were one of the first to identify the two main installation effects on jet noise (see Figure 2.15) by performing a series of experiments involving far-field measurements above and below a long, flat plate placed at the vicinity of an subsonic, unheated jet under static condition.

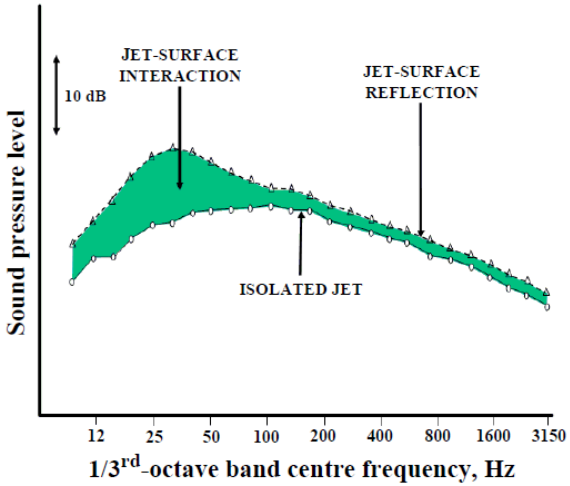

Figure 2.15 – Jet installation effect on the far-field acoustics of an subsonic, unheated jet. Results for the unshielded side of the plate. Source: Lawrence [24].

As shown in Figure 2.15, two main jet noise installation effects modifies the far-field noise of an isolated jet: (1) a low frequency augmentation attributed to jet-surface interaction (JSI) and (2) an broadband increase of mid and high frequencies due to jet-surface reflection (JSR). The mechanisms of sound generation behind these two installation effects are further discussed in the next sections.

2.3.1 Jet-surface interaction

As verified in Figure 2.15, the most relevant installation effect is observed as a low frequency increase. This effect is attributed to the interaction between the jet near-field and the plate trailing edge. This way, it is intuitive to think that the JSI effect on the far-field noise depends on the spectral characteristics of the jet near-field interacting with the plate. As can be verified in Figure 2.16, the axial and radial position of the plate in relation to the jet plume (see Figure 2.14) have important implications on the JSI effect.

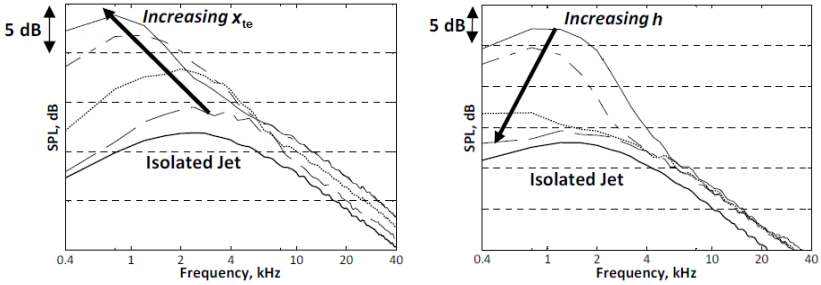

Figure 2.16 – Jet-plate interaction noise: (a) dependence on the axial position of the plate to the jet nozzle, x_{te}, for h/D_J=0.67 and (b) dependence on the radial position of the plate to the jet centerline, h, for x_{te}/D_J=4. Source: adapted from Lawrence et al. [45].

It is possible to verify in Figure 2.16a that the low frequency augmentation on the far-field noise of an isolated jet increases in magnitude and shift to lower frequencies as the plate moves downstream the jet flow. This is due to the large-eddies that evolves in size and magnitude as they are convected downstream the nozzle by the jet mean flow. Since the larger are the turbulent eddies, the lower is their frequency content, the peak frequency of the JSI noise decreases as the plate is positioned downstream. At the same time, as the plate moves axially downstream, it interacts with stronger and larger hydrodynamic pressure disturbances that propagates to the far-field due to scattering phenomena on the plate TE. On the other hand, as the plate is brought closer radially to the jet plume, the magnitude and the peak of the JSI noise increases (see Figure 2.16b). This stresses

the importance of the characterization of the jet pressure field incident upon the plate, since the frequency-content and magnitude of the jet near-field is highly non-homogeneous along the shear-layer.

Curle [46] was the first to tackle mathematically the problem involving the interaction between flow-induced noise and solid boundaries. Curle's analogy (see Appendix A.2) is a generalization of Lighthill's analogy where aerodynamic noise generated by free turbulence, which is analogous to a distribution of quadrupole sources whose force per unit volume is given by the Lighthill tensor, continues to be a fundamental part of the noise generation phenomena. However, an additional source term accounts for the resultant forces exerted on the fluid by the solid boundary (see Equation (A.6)). This noise source is given by a surface integral term which include the contributions of forces due (a) the impingement of sound waves generated by quadrupoles on the surface and (b) due to the flow itself. It is shown that this sound generation mechanism is equivalent to a distribution of dipole sources representing the fluctuating forces exerted on the fluid by the solid boundary.

For the derivation of a scaling law, Curle considered an acoustically compact body, that is, the solid surface has a characteristic length, s, much smaller than the acoustic wavelength, λ, of the sound generated by the aerodynamic noise sources, i.e. $s << \lambda$. For this specific case, Curle showed that the far-field acoustic power, which is proportional to the square of the acoustic pressure, p', scales with the sixth power of the flow speed,

$$p'^2 \sim U_{\mathrm{J}}^6, \tag{2.9}$$

which means that dipole noise sources generated by an acoustically compact body are more efficient noise sources, at low mach numbers, than Lighthill's quadrupoles description of aerodynamic sound generated by free turbulence, which scales with the eighth power of the flow velocity. Moreover, a dipole sound directivity implies that the radiation pattern can be described mathematically as

$$p'^2(\theta) \sim \sin^2(\theta), \tag{2.10}$$

where θ is the polar angle with respect to the incoming flow direction.

Head & Fisher [44], observed a dipole directivity pattern for low-frequencies in their experimental campaign (see Figure 2.17). The authors supports this verification by observing that the peak of the installation noise is at 90° and is reduced as the angle reduces to 0°. Moreover, a 180° phase difference is observed on the far-field noise

measured at microphones below and above the solid surface.

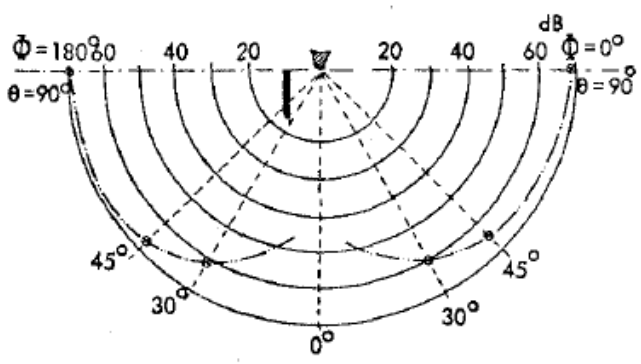

Figure 2.17 – Experimental verification of a dipole radiation pattern attributed to jet-surface interaction noise for low frequencies. Source: Head & Fisher [44].

Ffowcs Williams & Hall [17] are the first to discuss the influence of non-compact bodies on aerodynamic sound through a work with practical interest: the generation of sound near a semi-infinite plate (see Appendix A.3 for more details). The authors tackle this problem by considering the scattering of sound waves generated by a quadrupole distribution in the vicinity of a sharp edged semi-infinite plane. Note that all wavelengths are considered considered compact in this case once the surface characteristic length $s \to \infty$. Through a series of dimensional analysis, Ffowcs Williams & Hall argues that only turbulent structures close to the edge of the surface meeting the condition

$$2kr_0 << 1, \tag{2.11}$$

where k is the acoustic wavenumber and r_0 is the distance between the center of a turbulent eddy and the surface TE, will have a relevant impact on the far-field. In contrast, for turbulent structures whose distance from the surface TE is very large, satisfying the condition

$$(kr_0)^{\frac{1}{2}} >> 1, \tag{2.12}$$

the sound in the far field could be predicted by geometrical acoustics as the surface do not scatters the sound field. Moreover, the authors showed that the scattering of sound waves at the trailing edge of an acoustically non-compact body is a more efficient mechanism of sound

generation than Lighthill's quadrupoles and Curle's compact dipoles as the far-field acoustic power scales with the fifth power of the flow velocity,

$$p'^2 \sim U_J^5. \tag{2.13}$$

Moreover, the authors states that the directivity pattern of the sound field generated by non-compact bodies has a cardioid shape, given by

$$p'^2(\theta) \sim \sin^2(\theta/2), \tag{2.14}$$

which means that the maximum radiation occurs in the upstream direction of the trailing edge, that is, on the surface leading edge direction.

As discussed throughout this section, the characteristic length of the body and the wavelength of the sound waves incident on the plate are key parameters for the efficiency of the acoustic scattering effect. The relationship between these two parameters determines whether the sound field is interacting with an acoustically compact or non-compact body and has a significant impact on the far-field directivity pattern. Moreover, flow-structure interaction noise is a more efficient noise generation mechanism than the one of quadrupoles and its significance on the far-field also depends on the compactness of the body. Figure 2.18 illustrates the influence of the compactness of the body on the velocity dependency and radiation pattern on the far-field noise.

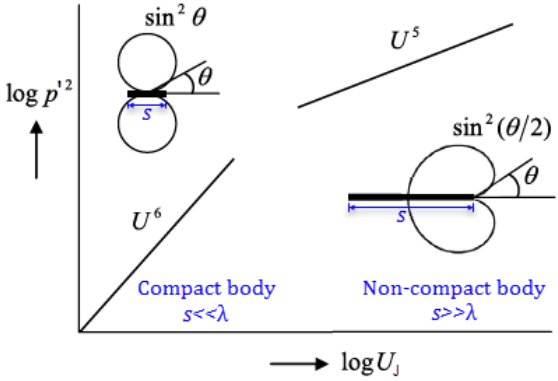

Figure 2.18 – Velocity dependency and noise directivity radiation pattern for compact and non-compact bodies. Source: adapted from van der Velden [47].

2.3.2 Jet-surface reflection

In addition to the scattering of the jet hydrodynamic field, the interaction of a solid surface with an acoustic field characterized by a wavelength much smaller than the surface characteristic length will lead to sound reflection. Brown [48], made an experimental campaign covering a wide range of jet-surface configurations and were able to verify this effect by measuring the sound spectra at the unshielded and shielded sides of the surface simultaneously (see Figure 2.19).

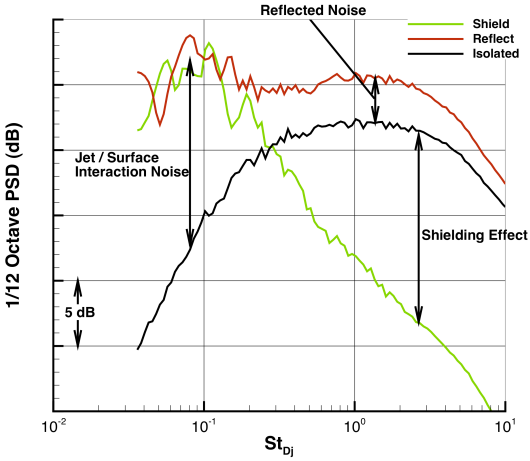

Figure 2.19 – Installation effects on the far-field noise emitted by an M_a=0.9, cold jet. The plate TE is positioned at x_{te}/D_J=14 and h/D_J=1. Source: Brown [48].

As observed in Figure 2.19, the reflection effect occurs only for the higher frequencies of the spectrum and the resultant acoustic field at this frequency range is divided into two regions, namely (1) a blocked region (shielded) and (2) a reflected region (unshielded). An increase of 3 dB in the unshielded side is observed due to the sum of incoherent reflections. Since the reflected sound waves have to propagate through the jet shear-layer, some degree of sound refraction and dispersion is expected to influence on the propagation of these sound waves. On the shielded side, the blockage of sound waves is verified as a consequence of the reflection effect. Moreover, the low-frequency augmentation attributed to the jet-surface interaction noise is verified at both shielded and unshielded sides with equivalent magnitudes, which

is an indication of the dipole radiation pattern characteristic of the jet-surface interaction noise previously discussed.

2.4 Computational Aeroacoustics (CAA)

The use of computational techniques for the prediction of noise generated by flows is called Computational Aeroacoustics (CAA). Since the compressible Navier-Stokes equations describes all information of the flow, including the acoustic field, solving them directly is the most accurate way to perform an aeroacoustic simulation. However, this approach is very expensive as the requirements on the grid resolution to solve the sound field for large distances without relevant numerical dispersion and dissipation demands an prohibitive computational cost. To overcome this limitation, hybrid methods are commonly employed for the computation of far-field aerodynamic sound. Figure 2.20 elucidates this categorization through a flowchart describing the main processes required for an direct or hybrid CAA simulation.

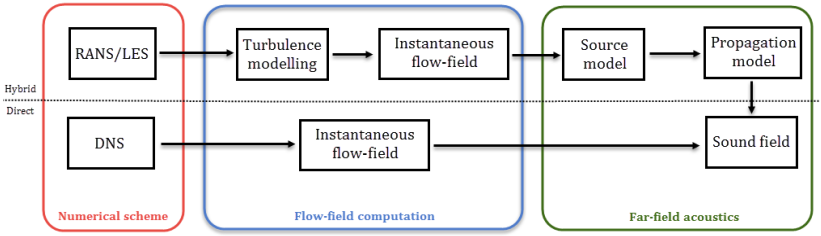

Figure 2.20 – Common CAA approaches to compute the far-field noise generated by aerodynamic sound sources.

In the hybrid approach, the far-field acoustic predictions are obtained through post-processing techniques based on aeroacoustic analogies. In this case, the information of the instantaneous flow-field is used to compute the aerodynamic sound sources at the near-field and then the contribution at the far-field is estimated by either an integral approach or by solving a set of equations, e.g. the Linear Euler Equations (LEE).

One of the major limiting factors in CAA is the computational cost required to accurately simulate turbulent flows. Usually, Computational Fluid Dynamics (CFD) techniques are employed to decrease the computational cost by modelling the turbulence scales of motion

with empirical or analytical models. In this sense, many approaches can be employed and, generally, the computational cost is related to the degree of definition in which the turbulence scales are solved. Figure 2.21 presents an classification on the most common CFD approaches for turbulent flow simulation according to their levels of accuracy. A detailed description on the classical CFD techniques can be found in Andersson [49].

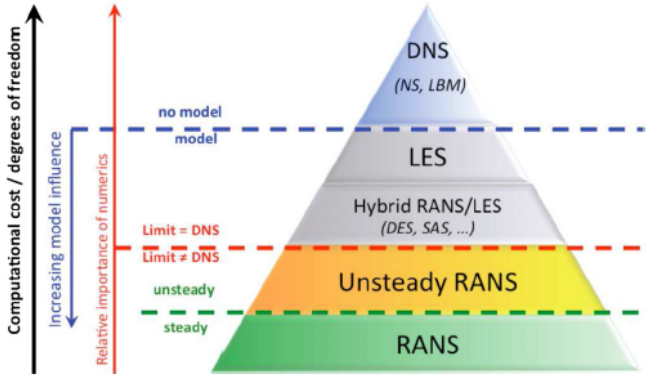

Figure 2.21 – Classical CFD approaches for turbulent flow simulation: classification according to levels of turbulence modelling and relative computational cost. Source: adapted from Deck et al. [50].

The Direct Numerical Simulation (DNS) solves all scales of motion, without any approximation. This method requires a high computational cost, limiting its use to simple cases and low Reynolds numbers. The works of Manning & Lele [51] and Freund [52] are pioneers in the use of DNS for jet noise modelling. The first studied the mechanisms of sound generation by supersonic flows and the second one validated experimentally a DNS model of a single jet with $M_J = 0.9$.

In the Large-Eddy Simulation (LES) approach, only the large turbulence scales are modeled and the dissipative effects related to small scales is accounted for by sub-grid models. Hybrid numerical models based on the use of LES techniques in conjunction with aeroacoustic analogies are the current state-of-the-art in jet noise simulation and in-depth discussions on the recent advances and limitations of such computational methodology are widely available throughout the literature [53, 54, 55, 56, 57].

A solution with a lower computational cost is the RANS[7] approach, where the steady flow solutions are obtained by taking the time average of the Navier-Stokes equation and using semi-empirical models to account for all turbulence scales. According to Wang [58], this approach alone is insufficient for aeroacoustic simulations as only the steady behaviour of the flow field is obtained. Often, far-field acoustic predictions can be obtained using RANS data as input for statistic source models based on semi-empirical relations [59] or by employing hybrid RANS/LES strategies.

As an alternative to the cited methods, which are based on the Navies-Stokes equation, numerical schemes based on the Lattice-Boltzmann Method (LBM) can be employed for the simulation of fluid motion. Based on the kinetic theory of gases, this method obtains the macroscopic behavior of the fluid by simulating the processes of propagation and collision of particles in discrete time and space. This method is intrinsically unsteady and compressible which makes it particularly suitable for aeroacoustic simulations. It is shown that the LBM recovers the compressible Navier-Stokes equation which makes it suitable for direct aeroacoustic simulations. Besides, the LBM can be coupled to turbulence models to account for the sub-grid scales of the fluid motion, reducing significantly the computational cost required for the simulation of high Reynolds number flows.

2.4.1 The use of LBM for jet noise prediction

In this work, a hybrid approach is used to simulate the far-field sound generated by a high-subsonic cold jet flow. The computational method is available by the commercial CFD package PowerFLOW, which employs a flow solver based on the VLES/LBM method for the simulation of the jet unsteady flow-field and then computes the far-field noise associated with it through a post-processing procedure based on the Ffowcs Williams & Hawkings integral method [60, 61]. The numerical scheme is discussed in more details in Chapter 3. Thus, a brief review on the works related to the use of this simulation tool for jet noise prediction is presented hereafter.

One of the first attempts to simulate the noise from a turbulent jet using the hybrid VLES/LBM approach was reported by Lew et al. [62, 63], by using PowerFLOW, version 4.1c, to simulate the noise from a single cold jet (M_J=0.4, Re_J=6×10^3). The flow results showed

[7] Acronym for Reynolds-Averaged Navier-Stokes method.

a good agreement when compared to experimental data and LES results while the predicted far-field noise results were within 2 dB from experimental results. The authors observed non-physical tones at the high-frequency range of the sound spectra, whose are believed to happen due to spurious sound wave reflections at the transition between regions with different grid resolutions. Nevertheless, the LBM proved to be a promising method for low-subsonic jet noise simulation as the results were in close conformity with LES simulations.

One of the major drawbacks of the LBM is that this method is derived under the limits of compressibility effects. In order to overcome this limitation, a new method to extend the solver capabilities to high-subsonic flows was reported by Lew et al. [64]. In this approach, an entropy solver based on a Finite Difference Method (FDM) scheme is coupled to the LBM solver to account for the compressibility effects on the flow. The authors validated the method for 3 benchmark cases of jet flows issued by an SMC000 nozzle[8]: SP03 (cold, M_J=0.5), SP07 (cold, M_J=0.98) and SP46 (hot, M_J=0.5). Figure 2.22 presents the results obtained for (a) the SP07 instantaneous flow-field and (b) the SP03 case where the overall far-field noise computed between the new methodology and the old low-subsonic solver (denoted as SP03i) are compared.

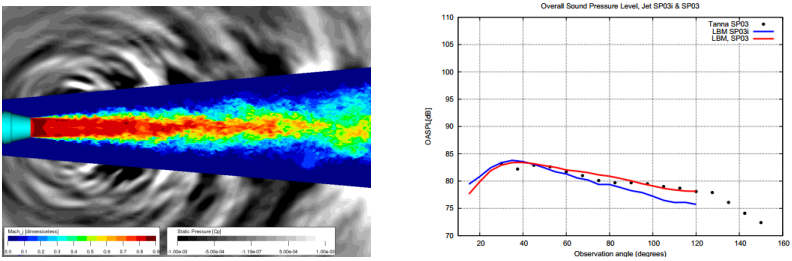

(a) Instantaneous Mach number and static pressure contours for case SP07.

(b) Far-field OASPL comparison between different solvers.

Figure 2.22 – High subsonic methodology validation: (a) flow and (b) acoustic predictions for cases SP07 and SP03, respectively. Source: Lew et al. [64].

[8]The benchmark cases are based on the experimental campaign of Bridges & Brown [65], whose reports a series of acoustic measurements for a wide range of jet conditions according to a matrix of set points (SP) of jet defined by the jet's Mach number and temperature ratio.

It is possible to observe in Figure 2.22a that the computational model was able to simulate effectively a cold jet flow with nearly sonic flow velocities. Moreover, the pressure contours of static pressure, which were conveniently saturated so as to emphasize acoustic waves, presents a radiation pattern which is consistent with the ones obtained by traditional LES schemes. The acoustic results obtained with the new high-subsonic solver (see Figure 2.22b), are in better agreement with the experimental results as the SP03i case was simulated using the old flow solver, limited to low-subsonic conditions up to M_J=0.4.

The installation effect caused by the interaction between a cold jet ($M_J = 0.5$) and a flat plate positioned parallel to the jet nozzle was investigated by da Silva et al. [66]. The effect of the radial distances of the plate from the jet nozzle was investigated. Figure 2.23 presents flow and acoustic results for one jet-plate configuration.

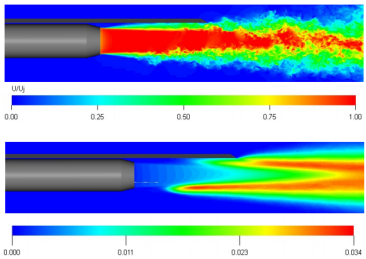

(a) Instantaneous contours of the jet velocity (above) and normalized TKE (below).

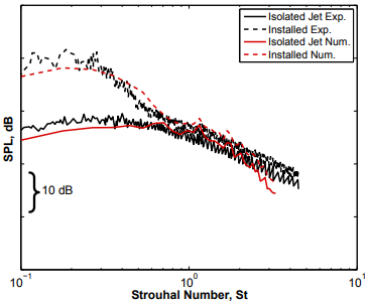

(b) Far-field SPL for isolated and installed cases.

Figure 2.23 – Jet-surface interaction noise investigation using PowerFLOW, version 5.0a. The plate is positioned at $h/D_J = 0.67$ and $x_{te}/D_J = 0.2$ (see Figure 5.1). Source: da Silva et al. [66].

The contours showed in Figure 2.23a presents low levels of turbulence near the nozzle exit, an indication that further improvements on the computational grid configuration, or in the turbulence model, are necessary. Nevertheless, the effect of this under-estimation of the turbulence field is not seen in the far-field acoustics as a good agreement with experimental results was obtained (see Figure 2.23b). This highlights the robustness of the code as the simulations are being able to capture the noise generation mechanisms attributed to the interac-

tion between the jet near-field and the plate. Da Silva et al. [67], further explored the computational model to assess the effect of sweep plate geometries on the installation effect and obtained results in concordance with experimental data. The effect of the sweep plate over an flat plate was observed as an increase on the lower-frequencies of the acoustic spectra for azimuthal far-field observer positions while a minor effect on the polar angles was observed.

More recently, van der Velden et al. [68] validated the new LBM based entropy solver introduced in PowerFLOW, version 6.0. The authors argue that the old FDM based entropy solver presented two main sources of numerical error: (1) spurious noise generated at the grid resolution transitions due to pressure disturbances and conservation issues, and (2) difficulties to apply boundary conditions in complex geometries non-aligned with the grid elements. A grid resolution analysis is presented for the cases previously assessed by Lew et al. [64]. The results for the SP46 (hot, $M_J = 0.5$) case are showed in Figure 2.24a. The authors verified that the acoustic and flow results converges for a medium resolution grid. This trend is observed for all polar angles assessed. Moreover, the robustness of the hybrid computational approach using the LBM flow solver and a permeable FWH integral formulation can be verified in Figure 2.24b as the simulations were consistent in capturing the difference on the noise generated by high-subsonic jet under different flow conditions.

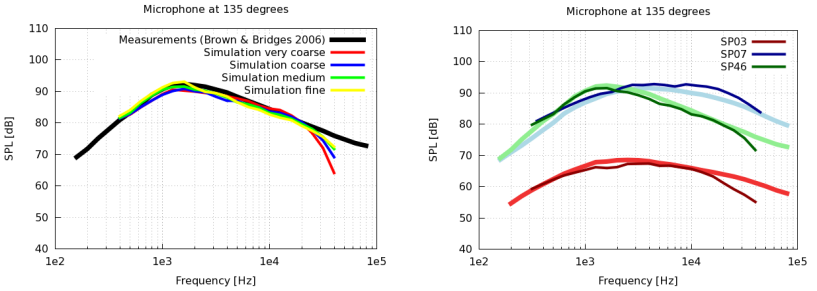

(a) Grid resolution analysis for SP46 (hot, $M_J = 0.5$).

(b) Comparison between different set points.

Figure 2.24 – Jet noise simulation validation of the LBM based entropy solver: far-field acoustic results obtained at a radial distance of $\sim 100 D_J$ from the nozzle exit. Source: van der Velden et al. [68].

3 NUMERICAL METHOD

In this work, the commercial CFD software PowerFLOW, version 6.0beta, is employed to perform the aeroacoustic simulations of a subsonic, single-stream, cold jet flow issued from a round nozzle under installed configurations. Therefore, it is important to understand the numerical scheme behind the software and it's limitations so that a proper simulation of the jet flow and the noise associated with it can be made. This chapter addresses the numerical procedures adopted by this work as follows: Section 3.1 aims to provide a comprehensive description of the numerical scheme adopted by PowerFLOW, including the flow solver and the approach adopted by the software to compute the far-field noise; Section 3.2 presents the computational setup, where details regarding the computational domain, mesh configuration, boundary conditions and time definitions are provided.

3.1 Numerical scheme

The commercial software PowerFLOW employs a hybrid approach to simulate high-subsonic fluid flows. The scheme involves a three-dimensional Lattice-Boltzmann scheme and an eddy-viscosity turbulence model to account for the unresolved scales associated with turbulent flows. The method is intrinsically transient and compressible which makes it particularly suitable for aeroacoustics simulations. Similar hybrid strategies have been successfully applied to assess both fundamental [69, 70] and complex [71, 72, 73] aeroacoustic phenomena.

This section provides an overview on the numerical scheme adopted in PowerFLOW, including a brief description of the Lattice-Boltzmann method (LBM) in Section 3.1.1. Details regarding the turbulence model (Section 3.1.2), meshing and solid surfaces representation (Section 3.1.3) and the wall model (Section 3.1.4) are provided. Finally, the far-field noise computation procedure employed in PowerFLOW is described by Section 3.1.5.

3.1.1 Lattice-Boltzmann method

The Lattice-Boltzmann method belongs to a particle based class of computational fluid dynamics methods. The fluid macroscopic behaviour is obtained by modelling the processes of propagation and collision of particle densities in discrete space and time. Traditional flow simulation approaches are based on derivations of the continuum equations for conservation of momentum, mass and energy. Hence, the fluid behaviour is generally computed by solving a set of partial differential equations, usually the compressible Navier-Stokes equation, through numerical schemes, e.g. Finite Volume method (FVM), Finite Element method (FEM) or Finite Difference method (FDM).

The Lattice-Boltzmann method solves a discretized version of the Boltzmann equation to obtain the flow macroscopic behaviour. In this work, the tridimensional D3Q19 model is adopted, which replaces the continuous velocity distribution function by a discrete set of 19 particle velocities defined on a lattice, or mesh grid, of equally shaped cubic cells (see Figure 3.1). During an elementary time interval Δt, particles can only travel from one center of a cell, $\vec{x}$, to one of the neighbouring cells, $\vec{x} + \vec{\xi}_i \Delta t$, according to their velocity, $\vec{\xi}_i$.

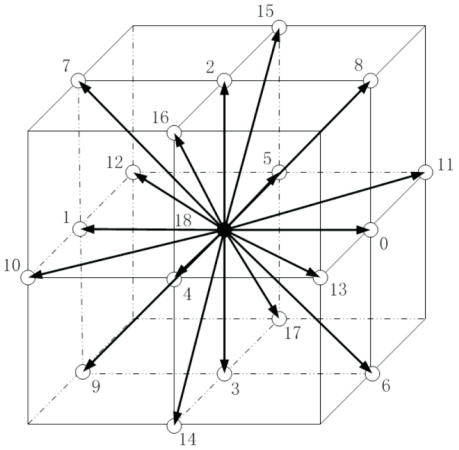

Figure 3.1 – Scheme of the D3Q19 model. The three-dimensional lattice cell has 19 velocity vectors on each cell node. Source: Kotapati et al. [71].

Considering a uniform grid increment, $\Delta x = \vec{\xi}_i \Delta t$, the Lattice-Boltzmann equation (LBE) has the following form [74, 75]

$$f_i(\vec{x} + \vec{\xi}_i \Delta t, t + \Delta t) - f_i(\vec{x}, t) = C_i(\vec{x}, t), \tag{3.1}$$

where the LHS of Equation (3.1) represents the propagation of fluid particles, being $f_i(\vec{x}, t)$ the density distribution function for each velocity component $i = 0, ..., 18$, at a given position $\vec{x}$ and time t. In turn, the RHS of Equation (3.1) represents the collision between particles, which forces the diffusion of momentum to an equilibrium state. The collision operator is approximated by the model proposed by Bhatnagar-Gross-Krook (BGK) [76], which assumes that the rate at which the molecular collisions occurs is proportional to the molecular collision frequency as

$$C_i(\vec{x}, t) = -\frac{\Delta t}{\tau}[f_i(\vec{x}, t) - f_i^{\text{eq}}(\vec{x}, t)], \tag{3.2}$$

where τ is the relaxation time, a parameter that represents the average time interval between particle collisions and which is directly related to the kinematic viscosity of the fluid being simulated, ν, by [64]

$$\tau = (\nu + 0.5)/T. \tag{3.3}$$

In Equation (3.2), the local equilibrium function, $f_i^{\text{eq}}(\vec{x}, t)$, is a discrete form of the Maxwell distribution function, which is derived from its continuous counterpart by applying the maximum entropy principle under the constraints of mass and momentum conservation [64, 77] up to third order as

$$f_i^{\text{eq}} = \rho w_i \left(1 + \frac{\vec{\xi}_i.\vec{u}}{T} + \frac{(\vec{\xi}_i.\vec{u})^2}{2T^2} - \frac{\vec{u}^2}{2T} + \frac{(\vec{\xi}_i.\vec{u})^3}{6T^3} - \frac{\vec{\xi}_i.\vec{u}}{2T^2}\vec{u}^2\right), \tag{3.4}$$

where T is the lattice temperature, set to $1/3$ for isothermal conditions. A formal link between the discrete form of the Boltzmann equation, and its macroscopic counterpart given by the Navier-Stokes equations is achieved by an asymptotic Chapman-Enskog expansion up to Mach numbers around 0.4 [78, 79, 80], confirming that the LBM method is suitable to simulate the continuous behaviour of fluid flow phenomena.

The weighting parameters, w_i, in Equation (3.4) for the D3Q19 model are

$$w_i = \begin{cases} 1/18 & \text{for } i = 0, ..., 5 \text{ (coordinate directions);} \\ 1/36 & \text{for } i = 6, ..., 17 \text{ (bi-diagonal directions);} \\ 1/3 & \text{for } i = 18 \text{ (rest particle).} \end{cases} \tag{3.5}$$

The macroscopic flow variables, such as density and velocity, can be recovered by the summing the statistical moments of the distribution functions:

$$\rho(\vec{x}, t) = \sum_i f_i(\vec{x}, t), \qquad \text{and} \qquad \rho\vec{u}(\vec{x}, t) = \sum_i \vec{\xi}_i f_i(\vec{x}, t). \tag{3.6}$$

It is worth mentioning that in the LBM, all variables, such as, position $\vec{x}$, velocity $\vec{u}$, temperature T, density ρ and time t are defined in dimensionless lattice units. A thorough discussion about the conversion between physical and dimensionless parameters in LBM is given by Aidun and Clausen [81].

For the simulation of high subsonic flows, PowerFLOW adopted an hybrid approach, called high subsonic method [64], to extend the Lattice-Boltzmann method capabilities up to near sonic conditions. In such methodology, the entropy equation is approximated using the Finite Difference method and coupled to the LBE in a similar fashion of Nie et al. [82]. However, according to van der Velden et al. [68], the FDM entropy solver has some drawbacks, such as: 1) difficulties to apply boundary conditions in complex geometries, which is observed as a lost of symmetry in the azimuthal direction of second order moments results; 2) pressure disturbance and conservation issues at the interface between different grid discretization zones, leading to nonphysical and unstable results. In order to overcome these limitations, an LBM based entropy solver has been recently developed and adopted by PowerFLOW, version 6.0beta. This approach introduces an additional set of distribution functions by using a scalar solver similar to the one developed and validated by Zhang et al. [83].

3.1.2 Turbulence modelling

For high Reynolds numbers, the LBE is extended in order to incorporate turbulence modelling [84, 85]. This procedure is made by modifying the molecular relaxation time into an effective relaxation

time, τ_{eff}, which is derived by a systematic Renormalization Group (RNG) [86] theory, as [69, 71]

$$\tau_{\text{eff}} = \tau + C_\mu \frac{\kappa^2/\varepsilon}{T(1+{\eta_{\text{T}}}^2)^{1/2}}, \tag{3.7}$$

where C_μ is a closure coefficient (see Equation (3.12)) and η_{T} is a combination of local strain, vorticity and helicity parameters for swirl correction [71].

The sub-grid turbulence contributions are computed by a modified RNG κ-ε two-equation turbulence model, given by [84, 87, 88]

$$\rho\frac{\text{D}\kappa}{\text{D}t} = \frac{1}{\sigma}\frac{\partial}{\partial x_j}\left[(\mu+\mu_{\text{T}})\frac{\partial\kappa}{\partial x_j}\right] + \tau_{ij}S_{ij} - \rho\varepsilon, \tag{3.8}$$

and

$$\begin{aligned}\rho\frac{\text{D}\varepsilon}{\text{D}t} = \frac{1}{\sigma}\frac{\partial}{\partial x_j}\left[(\mu+\mu_{\text{T}})\frac{\partial\varepsilon}{\partial x_j}\right] + C_{\varepsilon_1}\frac{\varepsilon}{\kappa}\tau_{ij}S_{ij} \\ - \left[C_{\varepsilon_2} + C_\mu\frac{\eta_{\text{T}}^3(1-\eta_{\text{T}}/\eta_0)}{1+\beta_{\text{T}}\eta_{\text{T}}^3}\right]\rho\frac{\varepsilon^2}{\kappa},\end{aligned} \tag{3.9}$$

where μ is the fluid dynamic viscosity, κ represents the turbulent kinetic energy, ε the turbulent dissipation, τ_{ij} the stress tensor and S_{ij} the strain rate, whose are defined as

$$\tau_{ij} = 2\mu_{\text{T}}S_{ij} - \frac{2}{3}\rho\kappa\delta_{ij}, \qquad \text{and} \qquad S_{ij} = \frac{1}{2}\left(\frac{\partial u_i}{\partial x_j} + \frac{\partial u_j}{\partial x_i}\right), \tag{3.10}$$

where the eddy viscosity is computed by [84]

$$\frac{\mu_{\text{T}}}{\rho} = \nu_{\text{T}} = C_\mu\frac{\kappa^2}{\varepsilon}, \tag{3.11}$$

given the following closure coefficients

$$\begin{aligned} C_\mu = 0.085, \quad C_{\varepsilon_1} = 1.42, \quad C_{\varepsilon_2} = 1.68, \\ \sigma = 0.719, \quad \eta_0 = 4.38, \quad \beta_{\text{T}} = 0.012. \end{aligned} \tag{3.12}$$

The equations above are solved in the same grid as the LBM but through a second order finite-difference scheme [89].

The link between the turbulence equations and the LBM simulation is through the eddy viscosity, ν_T, which is added to the kinematic viscosity in Equation (3.3) to achieve the effective relaxation time given by Equation (3.7). As can be inferred from Figure 3.2, this approach is often referred to as Very Large-Eddy Simulation (VLES) since it computes only the statistically anisotropic eddies outside the range of inertial and dissipative sub-grid scales.

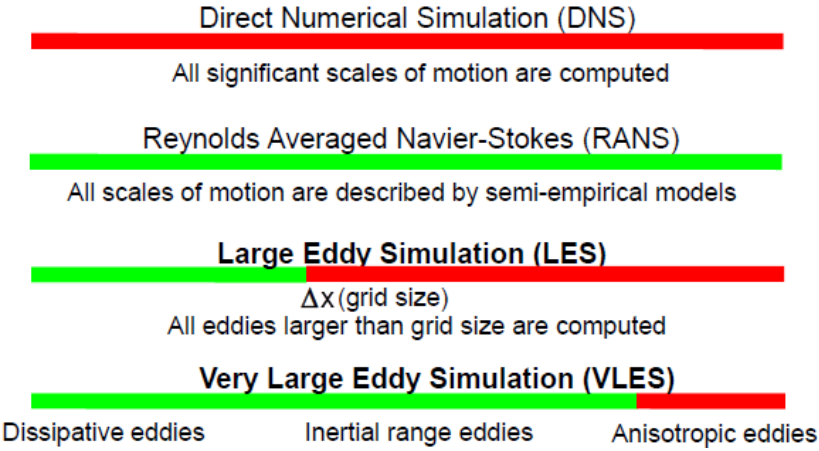

Figure 3.2 – Comparison between different turbulence modelling approaches in terms of modeled (green) and computed (red) turbulence scales. Source: adapted from [90].

3.1.3 Meshing and surface representation

The computational domain is composed by a structured grid, or lattice, of cubic cartesian volumetric cells, called voxels. The mesh refinement strategy is based on Variable Resolution (VR) regions, whose can be defined to locally allow the refinement or coarsening of adjacent grid regions by a factor of two. The grid refinement algorithm described in the work of Chen et al. [91] is employed to satisfy conservation of mass and momentum at VR transitions. Due to the intrinsic characteristics of the LBM scheme, the time-step resolution depends on the grid resolution of each VR, being inversely proportional to the grid size in factors of two as well. Therefore, larger voxels are not evaluated every time-step.

Regarding surface representation, a volumetric boundary scheme [92, 93] is employed since standard bounce back boundary conditions for no-slip condition do not produce accurate results on non-lattice aligned curved surfaces. The geometry is represented by surface elements, called facets, and surface cells, called surfels (see Figure 3.3a), are created at the intersection between voxels and facets.

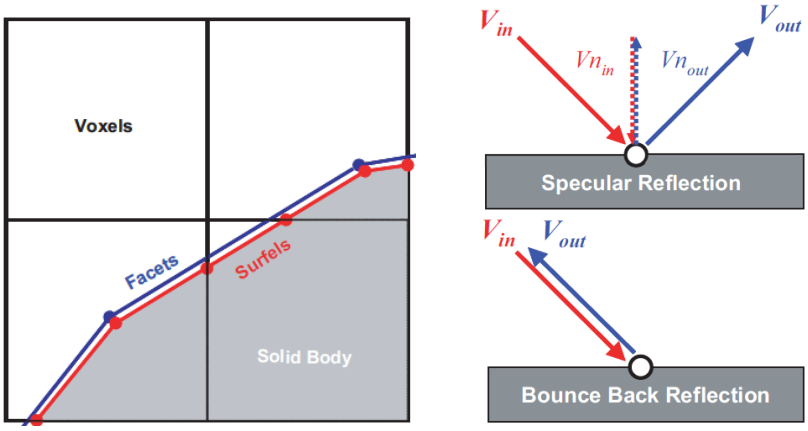

(a) (b)

Figure 3.3 – Fluid-surface interaction: (a) surface representation definitions; (b) slip and no-slip wall boundary conditions. Source: adapted from de Jong [94].

Wall boundary conditions are easily handled in complex geometries by applying simple particle bounce-back or specular reflection process (see Figure 3.3b) in the cases of no-slip or frictionless wall conditions, respectively. In each time step, the particles that would hit the surface are gathered by the surfels and the boundary conditions are applied by a surface-collision process. Later, the particles are scattered back from the surface to the fluid voxels. This procedure is illustrated in Figure 3.4. If a limited slip wall is needed, a weighted combination of these two methods can be used.

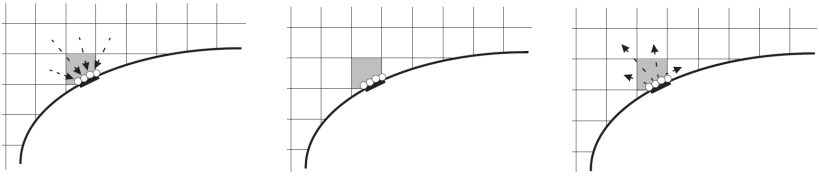

Figure 3.4 – Particle-surface interaction scheme: (a) voxel to surfel advection; (b) boundary conditions are applied via surface-collision process; (c) surfel to voxel advection. Source: adapted from PowerFLOW user's guide [95].

3.1.4 Wall shear stress model

For high Reynolds numbers, found in most practical applications, it is too expensive to fully resolve the boundary layer (BL) at solid surfaces. In order to reduce the computational cost, an pressure-gradient extended version of the wall function proposed by Launder & Spalding [96] is used to approximate the no-slip boundary condition on solid surfaces. According to Teixeira [84], the computation starts at the first cell above the wall instead of attempting to achieve a no-slip condition on the solid surface, where the fluid velocity at a slip surface (see Figure 3.5b), U_{Slip}, is typically non-zero. Hence, the fluid velocity profile towards the wall has the well known logarithmic profile if the law-of-the-wall holds at this location, and the shear stress at the slip surface is the same as its value at the wall.

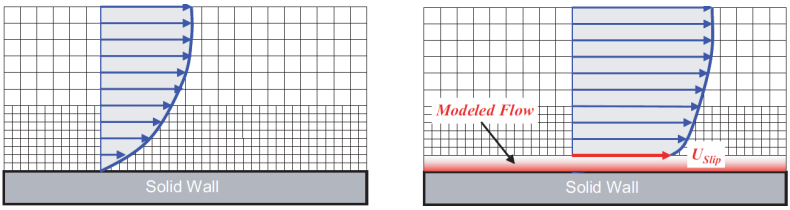

Figure 3.5 – Near-wall flow treatment for (a) DNS simulation and (b) VLES simulation. Direct simulations are feasible only for low Reynolds number flows as it requires a large number of voxels to fully resolve the boundary layer down to the wall. Source: de Jong [94].

The estimated local skin friction from the wall shear stress model are supplied to alter the momentum of scattered near-wall particles via a generalization of the surface collision process mentioned in Section 3.1.3. This is implemented by combining the two reflection models of Figure 3.3b with different weights.

3.1.5 Far-field noise computation

The prediction of far-field noise is a challenging task for numerical simulations since practical engineering problems involving large distances demands a prohibitive computational cost to resolve the propagation of small amplitude acoustic perturbations from the near-field source region to far-field observer position.

To overcome this difficulty, is possible to adopt an hybrid approach in PowerFLOW, meaning that the acoustical field at an far-field observation point is estimated in two steps: (1) the jet's unsteady flow field is computed using the hybrid Lattice-Boltzmann based flow solver; (2) the aerodynamic sound sources are computed from the transient solutions of the flow field and extrapolated to the desired far-field positions through a post-processing technique based on the Ffowcs Williams & Hawkings (FWH) surface integral method available in PowerACOUSTICS, version 4.0a. This procedure is explained in more details by Brès et al. [61] and also in Appendix A.4.

Essentially, this approach uses the idea of control surfaces to compute the contributions of the aerodynamic noise sources in the near-field based on the FWH analogy, and then an integral formulation is used to solve for the acoustic pressure at any far-field observation point. The input to the FWH solver are the unsteady flow field parameters, whose are stored in a surface mesh during the simulation. The surface mesh elements should be reasonably fine so that the smaller acoustic wavelengths being assessed are efficiently discretized. Also, a high oversampling ratio must be employed to ensure accuracy at the desired high-frequency cutoff because of the numerical differentiation involved in the computational FWH scheme [97]. Moreover, this approach requires that the computational mesh is fine enough to allow acoustic waves to propagate to the surface without suffering significant numerical dispersion and dissipation.

In this context, two types of control surfaces can be used:

- Solid (impenetrable) surface: in the case where the control surface corresponds to the contours of a solid body, the FWH analogy reduces to Curle's equation so that a surface distribution of dipole source represents aerodynamic sound generation due to unsteady forces exerted by the solid body upon the external fluid. In the case where the surface is moving, an additional monopole term accounts for sound generation due to the accelerations caused on the ambient fluid by the solid body;
- Permeable (porous) surface: in this case, a fictitious surface surrounds a region of the fluid containing all the relevant aerodynamic noise sources. The dipole and monopole source terms accounts for any aerodynamic sound generated at the porous surface as momentum and mass flux across the surface acts as noise sources associated with the acoustical field encompassed by the surface.

3.2 Computational model

The computational setup is based on Bridges & Brown [65] experimental campaign, which reports far-field noise data for a wide range of jet conditions according to a matrix of set points (SP) defined by the jet's acoustic Mach number, M_a, and temperature ratio, T_J/T_∞. This work is focused in the SP03, whose conditions, described by Table 3.1, characterize a cold subsonic single-stream jet.

Table 3.1 – Jet conditions.

NPR	M_a	M_J	T_J/T_∞	Re_J
1.2	0.50	0.50	0.955	585×10^3

In Table 3.1, the Nozzle Pressure Ratio (NPR) and jet Mach number M_J are defined as

$$\text{NPR} = \frac{P_0}{P_\infty}; \qquad M_J = \frac{U_J}{\sqrt{\gamma R T_J}}; \tag{3.13}$$

where P_∞ and P_0 are the ambient and stagnation pressure, respectively, and U_J is the jet velocity at the nozzle exit.

The nozzle under consideration is the SMC000 (see Figure 3.6a), which consists of a convergent nozzle with a inlet diameter of 6-inches ($\sim$ 152.5 mm) followed by a contraction of 27°. In the nozzle outlet, a 5° contraction tapers till the nozzle exit, which has a flat circular shape with an effective diameter of 2-inches (D_J = 50.8 mm). In the computational model, the cartesian coordinate system adopted has the origin centered at the nozzle exit (see Figure 3.6b), with the centerline set along the x-axis.

3.2.1 Computational domain and grid definitions

The jet nozzle is centered in a box-shaped fluid domain, whose side length corresponds to $L_D = 1024 D_J$ (see Figure 3.7). Target values corresponding to the ambient pressure, P_∞, are prescribed at the outer boundaries of the fluid box in order to emulate a free-field condition and a freestream Mach, M_∞, is set at the positive x-direction to help in the jet entrainment. The fluid properties set in the simulation domain are presented in Table 3.2.

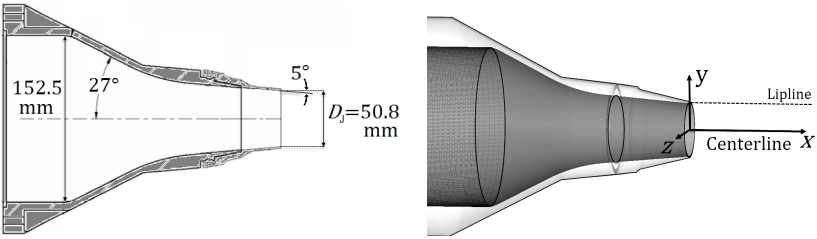

(a) (b)

Figure 3.6 – Sketch of the SMC000 nozzle: (a) geometry details described by Bridges & Brown [65] and (b) the computational nozzle with adopted cartesian coordinate system.

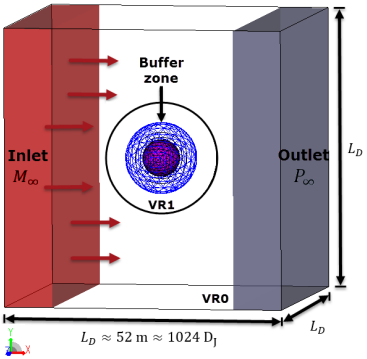

Figure 3.7 – Computational domain.

Table 3.2 – Nominal fluid properties considered in the simulations.

Pressure	$P_\infty = 101325$ Pa
Temperature	$T_\infty = 288.15$ K
Sound speed	$c_\infty = 340.3$ m/s
Freestream Mach	$M_\infty = 0.005$
Density	$\rho_\infty = 1.22$ kg/m^3
Kinematic viscosity	$\nu_\infty = 1.46 \times 10^{-5}$ m^2/s

To reduce the computational cost, the domain is partitioned into fourteen (14) variable resolution regions, where the VR 0 and VR 13 corresponds to the coarser and finest grid resolutions, respectively. A spherical sponge layer (see Figure 3.8) is defined to prevent any inward reflection of acoustic waves. The buffer zone is characterized by an exponential increase of the damping parameter along a spherical zone defined from a inner radius corresponding to the end of VR 5, $r_{\text{inner}} \approx 60D_J$ from the nozzle exit, to a outer radius corresponding to the end of VR 2, $r_{\text{out}} \approx 123D_J$. The damping parameter ν/T ranges from a minimum of 0.005, which is the default value employed in the simulation volume containing the jet flow itself (from VR 5 inwards), to a maximum of 0.5, which is applied in the region where $r \geq r_{\text{out}}$.

The damping parameter is defined as [97]

$$\nu/T = B_{\mathrm{B}} \times \exp(A_{\mathrm{B}}.r), \tag{3.14}$$

where the factors A_{B} and B_{B} are defined by

$$A_{\mathrm{B}} = \log\left[\frac{(\nu/T)_{\min}}{(\nu/T)_{\max}}\right] / (r_{\mathrm{inner}} - r_{\mathrm{out}}), \tag{3.15}$$

and

$$B_{\mathrm{B}} = \left(\frac{\nu}{T}\right)_{\min} / \exp(A_{\mathrm{B}}.r_{\mathrm{inner}}). \tag{3.16}$$

A set of concentric VRs with conical shape (see Figure 3.9) are defined to avoid abrupt discontinuities by gradually coarsening the grid resolution. These VRs forms the mesh configuration towards the main region of interest, the jet plume, which is enclosed by VR 10. The FWH surface is also inside this VR and will be defined in Section 3.2.3.

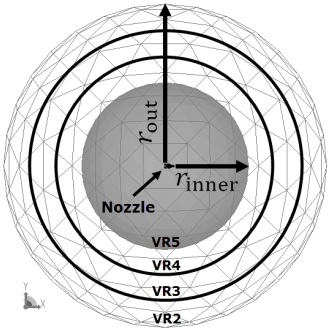

Figure 3.8 – Anechoic buffer zone and adjacent variable resolution regions.

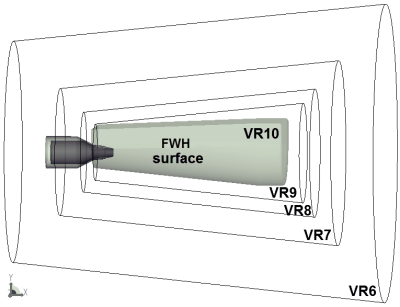

Figure 3.9 – Variable resolution configuration towards the jet plume and FWH surface.

The mesh configuration in the main region of interest can be seen in Figure 3.10. The finer grid resolution is distributed along VR 13, which comprehends the nozzle boundary layer, starting from the end of the contraction zone inside the nozzle to a small zone outside the nozzle lip. This exterior radial refinement is needed because the flow suffers a high strain rate at the nozzle interface between internal and external domains, meaning that substantial local velocity gradients need to be computed (see Equation (A.2)). Thus, if not well discretized, the turbulence model is not able to compute eddy viscosity efficiently

at this region, fact which, according to Brès et al. [98] and Farosonov et al. [99], compromises the jet flow transition to a fully turbulent regime as the early shear layer is not adequately computed. The VR 12 and VR 11 are also extended outside the nozzle. The first is meant to refine the jet early shear layer and the later the jet shear layer up to the end of the potential core, whose has the length estimated based on Witze's formula (see Equation (2.6)). Figure 3.10b presents grid details in the vicinity of the jet nozzle and also illustrates the position of the boundary layer trip, which is discretized by VR 13 at the proximity of the nozzle walls. The use of a tripping device is further discussed in Section 3.2.2. Furthermore, Figure 3.10c gives an azimuthal perspective of the grid discretization at the nozzle exit.

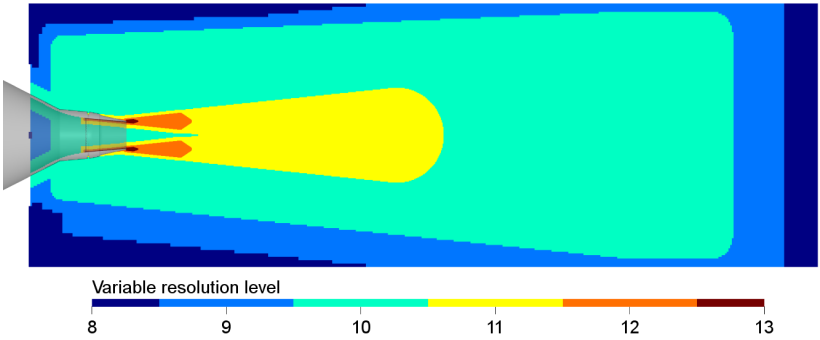

(a)

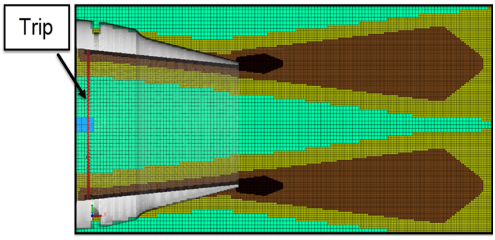

(b)

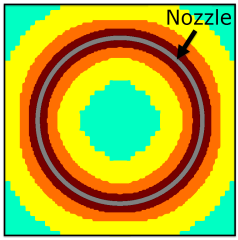

(c)

Figure 3.10 – Computational grid layout: (a) lateral view; (b) grid details and trip position and (c) frontal view at the nozzle exit.

3.2.2 Boundary layer tripping

In real applications, the flow coming into the jet exhaust is fully unsteady when it reaches the exhaust nozzle, but this cannot always be achieved in simulations with conventional boundary conditions. In order to overcome this computational limitation, solid trip entities can be used as an artifact to introduce unsteadiness in the nozzle boundary layer (see Figure 3.11).

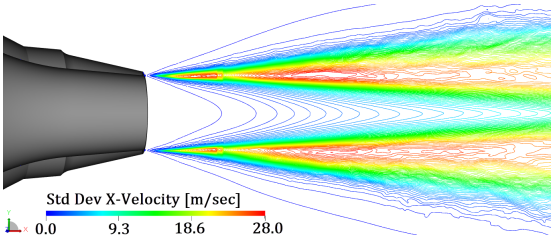

(a)

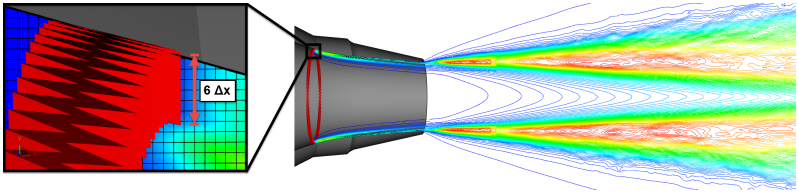

(b)

Figure 3.11 – Contours of resolved turbulence for simulations (a) without and (b) with trip.

In the case of PowerFLOW, the trip adds 3-dimensionality to the fluid flow and activates the swirl model, supporting the turbulence model to trigger instabilities that will generate a unsteady flow. The question is: how to best define a trip? The impact of factors such as geometry, position and thickness were assessed by a previous investigation [100], from where the trip configuration applied to the numerical model was defined.

The trip adopted has a circular geometry with a height of $6\Delta x$ and 200 ziz-zags distributed equally around it's circumference. The trip is positioned $1.5D_{\mathrm{J}}$ away from the nozzle exit in order to prevent any spurious trip noise in far-field acoustics.

3.2.3 Boundary conditions and FWH surface

The mean flow is imposed in a region upstream the nozzle exit by a total pressure inlet Boundary Condition (BC), which constraints the stagnation pressure P_0 and temperature T_0 values of the flow at the inlet region illustrated in Figure 3.12. Based on the jet Mach number M_J and temperature ratio given by Table 3.1, the inlet BC input parameters are calculated using the following isentropic thermodynamic relations,

$$P_0 = P_\infty \left(1 + \left(\frac{\gamma - 1}{2}\right) M_\mathrm{J}^2\right)^{\frac{\gamma}{\gamma - 1}}, \tag{3.17}$$

and

$$T_0 = T_\mathrm{J} \left(1 + \left(\frac{\gamma - 1}{2}\right) M_\mathrm{J}^2\right). \tag{3.18}$$

Turbulent kinetic energy and dissipation input values based on a turbulence intensity of 1 % and turbulent length scale in the order of 1 % of the jet diameter are also prescribed at the inlet BC. A buffer zone with increased viscosity is set to prevent the formation of any acoustical field inside the nozzle. Regarding the solid surfaces, all nozzle interior walls are treated as no-slip, including the trip surface.

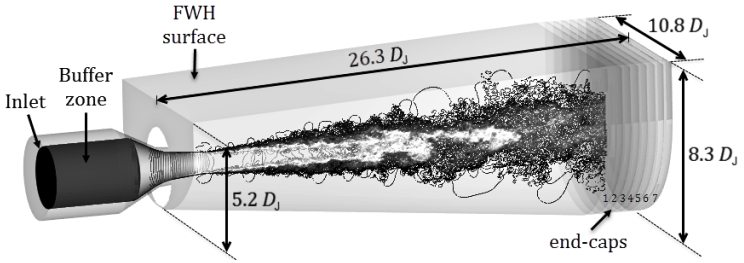

Figure 3.12 – Scheme illustrating the inlet and buffer zone applied in the jet nozzle along with the FWH surface geometry and transient contours of velocity magnitude.

The permeable FWH surface geometry is shown by Figure 3.12. This particular geometry was adopted so that it could encompass all the relevant noise sources, including installed cases where the additional sound sources associated with the presence of a solid surface near the jet also needs to be computed. Because the downstream region of the

surface is in direct contact with hydrodynamic disturbances, it must be far away and contain a series of end-caps to be time-averaged together. Following the recommendations of Shur et al. [101] and Mendez et al. [102], this averaging procedure is necessary to mitigate spurious noise associated with the hydrodynamic disturbances of the flow being advected downstream through the surface. Having this in mind, the FWH surface adopted extends for $25D_\mathrm{J}$ from the nozzle exit and also covers a small portion upstream the nozzle's exit. Seven end-caps are placed at the surface downstream, with an distance $\Delta l_\mathrm{cups} = 0.42D_\mathrm{J}$ from each other.

Time histories of the jet's velocity, pressure and density fields are stored on the surface for later extrapolation to the far-field through a post-processing procedure using the FWH formulation described in Section 3.1.5. The results are acquired in the surface mesh elements, whose spatial resolution and acquisition sampling rate requirements will be further assessed in Section 4.2.2 by a parametric analysis.

3.2.4 Time definitions

The total simulation time, t_s, is divided into two terms, namely the transient time, t_t, and the acquisition time, t_a, so that $t_\mathrm{s} = t_\mathrm{t} + t_\mathrm{a}$. The transient time is necessary in order to ensure the convergence of the mean flow to its steady state, and is based in the time needed for the jet flow to exit the nozzle and the FWH surface, as

$$t_\mathrm{t} = 10\left(\frac{L_\mathrm{FWH}}{U_\mathrm{J}}\right), \tag{3.19}$$

where L_FWH is the FWH surface length. Therefore, the transient time configured allows ten flow passes through the FWH surface. In turn, the acquisition time is calculated based on the minimum frequency of interest ($f_\mathrm{min} = 134$ Hz $\rightarrow \mathrm{St}_\mathrm{min} = 0.04$) multiplied by a factor $\beta_\mathrm{s} = 15$[1], so that

$$t_\mathrm{a} = \beta_\mathrm{s}\left(f_\mathrm{min}\right)^{-1}, \tag{3.20}$$

which corresponds to $t_\mathrm{a} = 0.11$ s or, in dimensionless acoustic units, $t_\mathrm{a}c_\infty/D_\mathrm{J} \approx 750$.

[1]The acquisition time factor β_s comprehends the number of desired spectral averages times the window overlap factor. For this work, 30 spectral averages were set in order to ensure an adequate statistical convergence and an overlap factor of 50% is adopted.

4 VALIDATION ANALYSIS: ISOLATED JET

This section presents the validation of the computational model described in Section 3.2. Recently, jet noise simulations using the new entropy solver available in PowerFLOW, version 6.0beta, were validated by van der Velden et al. [68], including the SP03 configuration. The current work complements this validation by further investigating the sensitivity of both hydrodynamic and acoustic fields to the grid resolution. The analysis is carried out for the case of an isolated jet and three grid resolutions. Table 4.1[1] presents details on the configurations of the cases considered.

Table 4.1 – Computational setup of the validation cases. All simulations were performed on a Linux Xeon E5-2690 2.9 GHz platform with 480 cores and 128 GB RAM.

	Grid resolution		Time resolution		Mesh size	Computational cost	
Case	$D_J/\Delta x$	Δx (mm)	Δt (μs)	$\Delta t c_\infty/D_J$	10^6 cells	Hours	kCPUh
coarse	256	0.198	0.30	0.0020	128	10.9	5.2
medium	360	0.141	0.21	0.0014	313	31.5	20.8
fine	512	0.009	0.15	0.0010	806	84.7	44.8

For the validation of the acoustic results, an experimental campaign based on the flow configurations described by Table 3.1 was performed at the Jet Acoustic Rig (JAR), located in the Laboratory of Vibrations & Acoustics (LVA) at the Federal University of Santa Catarina (UFSC), Brazil. Further information about the facility and its validation, as well as on the experimental setups are presented in Appendix B. The validation of the computational model is carried out in two steps:

1. The jet flow field is validated in Section 4.1 against the experimental results reported by Bridges & Wernet [26]. The validation of the simulated aerodynamic field is further complemented in Section 4.1.1 by comparing the boundary layer profile at the nozzle exit with experimental results obtained at the JAR (LVA/UFSC) by Camara [103], using hot-wire anemometry (HWA);

[1] The grid resolution is defined here taking into account the spatial pitch, Δx, of the finest grid element size.

2. Far-field acoustic predictions are validated in Section 4.2, having experimental results obtained at the JAR (LVA/UFSC) as the reference.

4.1 Flow field

This section validates the jet's mean flow field computed by the numerical model. Figure 4.1 presents contours of mean acoustic Mach number and standard deviation of the axial velocity for the coarse resolution case. Figure 4.1a shows that the averaged acoustic Mach number along the nozzle exit diameter achieved by the simulated jet is $M_a = 0.48$, an error of 4% in relation to the target value prescribed at the inlet, which was $M_a = 0.5$. This was observed for all cases assessed and can be attributed to the prescribed inlet boundary condition (see Section 3.2.3), which is defined under the premise of a uni-dimensional compressible isentropic flow. Since the far-field acoustic pressure is related to the jet velocity, an underestimation of the acoustic results obtained by the numerical model is expected.

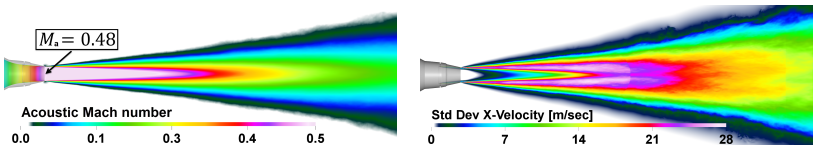

(a) (b)

Figure 4.1 – Contours of the jet mean flow field obtained with the coarse resolution case: (a) acoustic Mach number and (b) streamwise velocity standard deviation.

Figure 4.1b presents the computational predictions of the jet's mean turbulence field, from where it is possible to verify qualitatively that the flow field has achieved transition to a fully developed turbulent profile for the coarse resolution case. This observation along with the symmetric behaviour of the flow field showed by Figure 4.1 are good indications that the computed flow field has achieved statistical convergence. A quantitative analysis is made hereafter to investigate the influence of the grid resolution on the flow predictions of the computational model.

4.1.1 Boundary-layer

As previously discussed in Section 3.2.2, the effective computation of the turbulence levels inside the nozzle plays an important role when modelling jet noise since it impacts directly on the transition of the jet's shear-layer. Besides, the boundary-layer condition at the nozzle-exit provides information on the flow regime inside the nozzle. Figure 4.2 assesses the grid resolution influence on the boundary-layer state by comparing experimental and computational results of the mean axial velocity and turbulence profiles at the nozzle-exit.

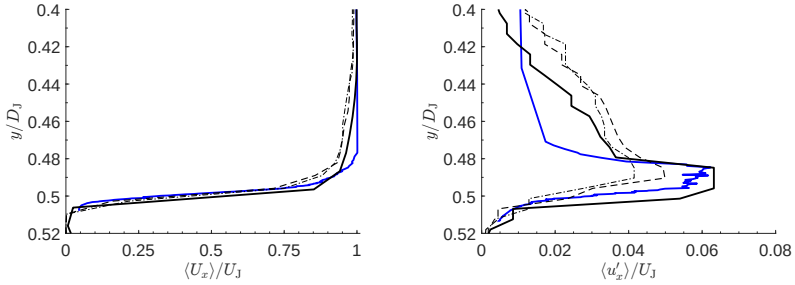

Figure 4.2 – Mean (a) and turbulence intensity (b) boundary-layer profiles at the nozzle exit ($\sim x/D_J$=0.04). Experimental results obtained at the JAR (LVA/UFSC) by Camara [103] using hot-wire anemometry (——) and numerical results represented by: coarse (- · - · -), medium (- - - -) and fine (——).

It is possible to observe in Figure 4.2a that the mean axial velocity profile is slightly altered by the grid resolution. Moreover, all computational predictions of the mean velocity profile at the nozzle exit are in good agreement with the experimental results. The small deviations can be attributed to differences between experimental and numerical measurement positions.

On the other hand, the turbulence intensity levels at the nozzle exit proved to be sensitive to the grid resolution, as can be verified in Figure 4.2b. This is expected since the increase of the grid resolution lead to (1) the flow is more refined at the vicinity of the nozzle inner walls; (2) the simulation time resolution is smaller. Both factors impact the simulated unsteady flow since they force the computational model to resolve smaller turbulence length-scales. Thus, the computational

model was able to present turbulence levels close to the experiment only when using the fine resolution grid.

4.1.2 Jet development

Figures 4.3 and 4.4 verify the influence of the grid resolution on the jet's development by presenting results of the mean flow field along the jet centerline and lipline. The numerical results are compared to the experimental measurements of Bridges & Wernet [26], whose were defined from a consensus among three jet measurements made under the same conditions as SP03 but with different nozzles, being one of them the SMC000. Figure 4.3 shows time-averaged results of the mean axial velocity and turbulence intensity along the jet centerline.

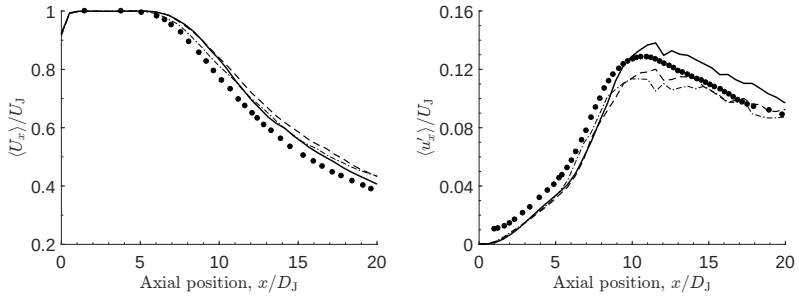

Figure 4.3 – Streamwise velocity along the jet centerline: (a) mean velocity and (b) turbulence intensity. Experimental results by Bridges & Wernet [26] represented by symbols (●) and numerical results represented by lines: coarse (- · - · -), medium (- - - -) and fine (——).

The results presented in Figure 4.3a indicate that the numerical model is over-predicting the jet potential core length[2]. The estimated lengths from the numerical data are x_c/D_J=6.9, 7.1 and 7.3 for the coarse, medium and fine resolution cases, respectively, while the experimental value is x_c/D_J=6.8. Despite the potential core over-estimation, all cases seems to provide an good estimate of the mean flow decay along the jet centerline.

[2]The jet potential core length is defined as the axial position, x_c, where the jet centerline velocity reduces 95 % of the exhaust velocity, $U(x_c) = 0.95U_J$ [64].

The numerical results for the turbulence intensity showed in Figure 4.3b presented similar trends as the reference results, an indication that the computational model provides a fair prediction of the jet turbulence field evolution along the centerline. However, the turbulence intensity peak, at approximately $x/D_\mathrm{J} = 10.7$, is better predicted by the fine resolution case as a consequence of the grid resolution increasing in the nozzle boundary layer and at the jet plume. It also supports the understanding that the turbulent boundary-layer condition at the nozzle-exit impacts the development of the jet since higher turbulence levels along the centerline were verified.

Figure 4.4 shows the mean velocity (a) and turbulence intensity (b) results along the jet lipline. From Figure 4.4a, it is possible to observe that (1) all cases presented similar results and (2) the mean velocity field is underestimated from the nozzle exit to $x/D_\mathrm{J} = 5$ and then presents an good agreement with the experimental results downstream the jet's lipline. Figure 4.4b shows that the computational model was able to predict accurately the turbulence intensity levels along the jet lipline for the medium and fine cases while the coarse case underestimate the experimental result. Despite the deviations of the numerical results after $x/D_\mathrm{J} = 10$, one can verify in Figure 17 of Bridges & Wernet [26] work that all simulated turbulence field magnitudes are inside the standard deviation of the consensus curve used as reference here. It is noticeable that the grid resolution has exerted little influence on the mean velocity field while the turbulence intensity results are more dependent on the grid resolution.

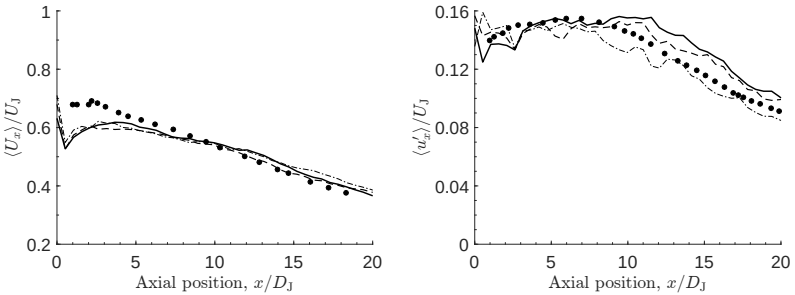

Figure 4.4 – Streamwise velocity along the jet lipline: (a) mean velocity and (b) turbulence intensity. Experimental results by Bridges & Wernet [26] represented by symbols (●) and numerical results represented by lines: coarse (- · - · -), medium (- - - -) and fine (——).

4.1.3 Axisymmetry

Despite the good agreement of the numerical model in both magnitude and shape at the jet centerline and lipline, more information of the grid resolution influence on the spatial homogeneity of the simulated jet flow is needed. Figure 4.5 compares computational and experimental radial profiles of the jet mean velocity, computed at distinct axial positions ($x/D_\mathrm{J} = 4, 8, 12$ and 16).

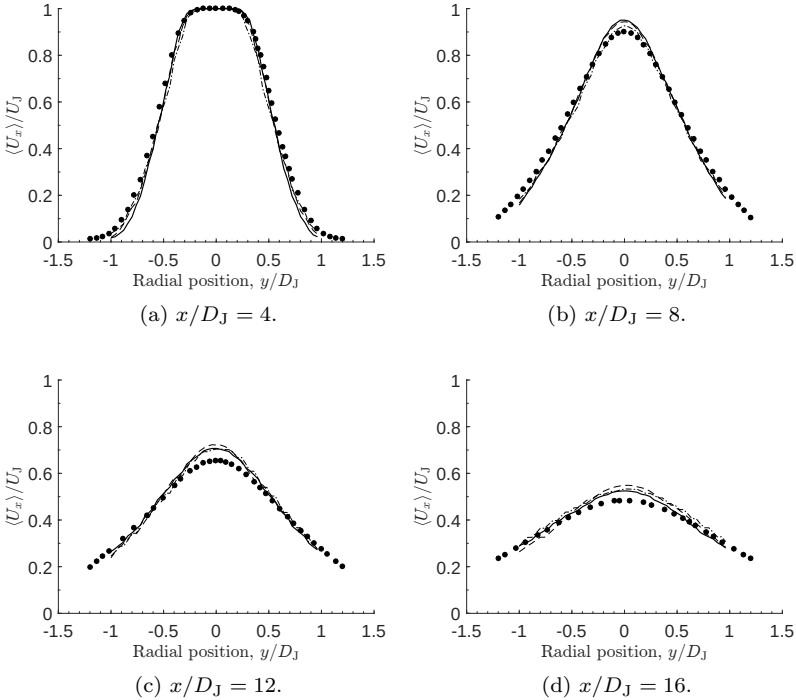

(a) $x/D_\mathrm{J} = 4$. (b) $x/D_\mathrm{J} = 8$.

(c) $x/D_\mathrm{J} = 12$. (d) $x/D_\mathrm{J} = 16$.

Figure 4.5 – Radial profiles of streamwise mean velocity at different axial positions. Experimental results by Bridges & Wernet [26] represented by symbols (●) and numerical results represented by lines: coarse (-·-·-), medium (- - - -) and fine (——).

Is possible to observe in Figure 4.5 that the simulated mean velocity magnitude is specially over-predicted at the jet centerline for axial distances far-downstream, but follows the same trends of the experi-

mental results as the radial distance increases. This is an indication that, despite the over-estimation of the jet potential core length already verified in Figure 4.3a, the numerical model was able to capture the spatial development of the jet mean flow satisfactorily with almost no sensitivity to the grid resolution.

Figure 4.6 presents radial profiles of turbulence intensity for different axial positions. The results shows that, despite the over-prediction at $x/D_\mathrm{J} = 16$, the simulated radial profiles of turbulence are in good agreement in both level and shape with the reference results. This shows that the grid refinement has a small impact on the results.

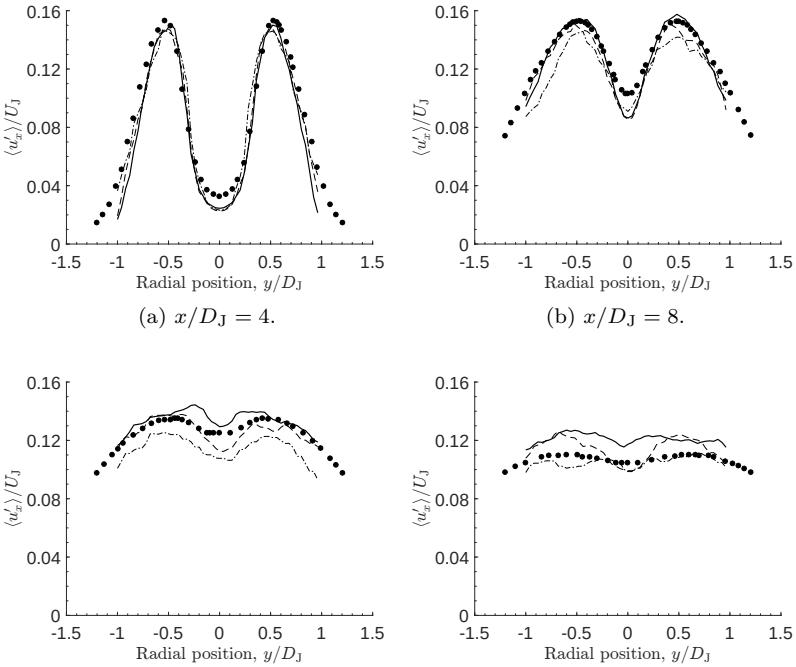

(a) $x/D_\mathrm{J} = 4$. (b) $x/D_\mathrm{J} = 8$.

(c) $x/D_\mathrm{J} = 12$. (d) $x/D_\mathrm{J} = 16$.

Figure 4.6 – Radial profiles of turbulence intensity for distinct axial positions. Experimental results by Bridges & Wernet [26] represented by symbols (●) and numerical results represented by lines: coarse (- · - · -), medium (- - - -) and fine (——).

Figure 4.7 provides a qualitative verification of the azimuthal symmetry of the velocity field obtained with the coarse resolution model. The radial contours allow to verify that mean velocity and turbulence flow solutions achieved for the coarse resolution grid exhibited an axisymmetric behaviour at different axial positions, which is expected for a statistically converged turbulent jet flow issued by a round nozzle.

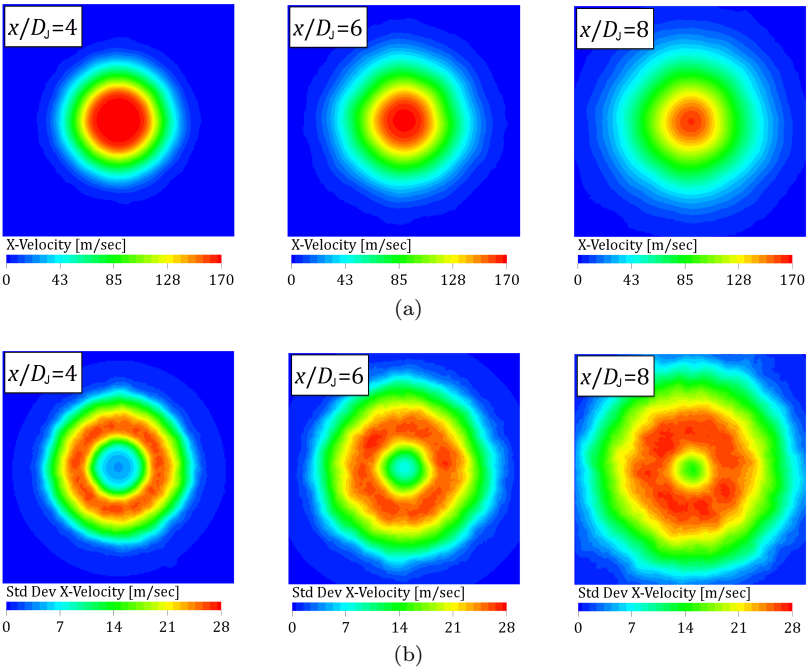

Figure 4.7 – Radial contours of (a) streamwise mean velocity and (b) velocity standard deviation for different axial positions. Numerical results obtained with the coarse resolution model.

4.2 Far-field acoustics

This section verifies the influence of the numerical grid resolution on the far-field acoustic results. As previously discussed in Section 3.1.5, PowerFLOW employs a hybrid methodology to compute the noise at a far-field observation point. The signals in time and frequency domain are obtained in PowerACOUSTICS 4.0b by post-processing the results previously stored at the permeable FWH surface defined in Section 3.2.3.

First, the time-domain FWH formulation (see Appendix A.4) is employed to compute the acoustic pressure fluctuation, $p'(\mathbf{x}, t)$, at time, t, and cartesian microphone vector position $\mathbf{x}$, which is defined based on the polar and azimuthal planes defined in Figure 4.8. The signals are propagated to a radial distance of $\sim 41D_{\mathrm{J}}$ (2.01 m) from the nozzle exit. The resultant pressure signal is computed from the contributions of all the permeable FWH surface faces, including the time-averaged pressure contribution among the end-caps, as discussed in Section 3.2.3.

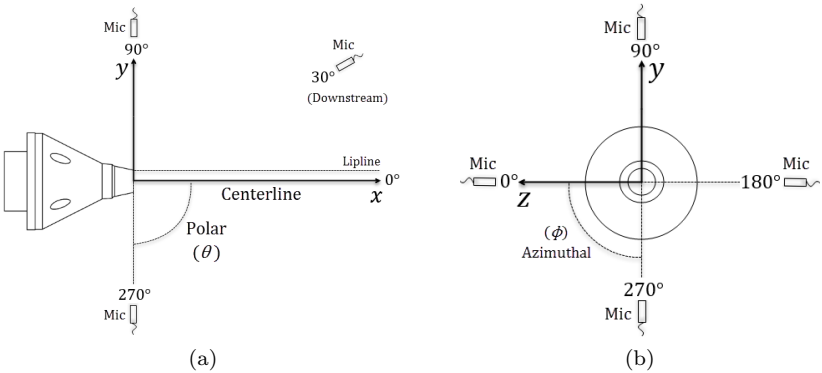

Figure 4.8 – Coordinates definitions: (a) polar plane and (b) azimuthal plane.

In a second moment, the far-field noise is assessed in frequency domain by applying a windowed Fast Fourier Transform (FFT) to the pressure signals, following the Welch's method [104]. All signals are processed in narrow-bands with a frequency discretization $\Delta f = 25$ Hz. To minimize energy leakage, Hanning windows with 50 % overlap were applied to the signals. Since the pressure signals were obtained

during $t_a = 0.11$ s, the Welch's method allows ~ 6 spectral averages to be taken along the signal[3].

The Sound Pressure Level (SPL) is computed from the power spectrum of the complex pressure Fourier coefficients, $S_{pp} = \tilde{P}(\mathbf{x}, f)\tilde{P}^*(\mathbf{x}, f)$, as

$$\mathrm{SPL}(\mathbf{x}, f) = 10 \log_{10} \left(\frac{S_{pp}}{p_{ref}^2} \right), \tag{4.1}$$

where the superscripts $\tilde{(.)}$ and $(.)^*$ denote a complex quantity and its conjugate, respectively, and $p_{ref} = 20$ μPa is the reference sound pressure level.

4.2.1 Data correction

It was previously verified in Figure 4.1 that the exit acoustic Mach number of the simulated jet is underestimated, so a velocity correction must be applied in order to compare the far-field acoustic results computed by the numerical model with the experimental results obtained at the JAR (LVA/UFSC). The corrected SPL is given by

$$\mathrm{SPL}_c = \mathrm{SPL} + 10 \log_{10} \left(\frac{M_{a_{ref}}}{M_a} \right)^{\eta(\theta)}. \tag{4.2}$$

For the sake of comparison, it was chosen to adopt the velocity condition of the numerical model as the reference value, so that $M_{a_{ref}} = 0.48$. This velocity correction is based on Lighthill's eighth power law but rather then a fixed exponent coefficient, it relates the far-field acoustic pressure to the jet velocity by employing a angular coefficient $\eta(\theta)$, so that $p'^2 \propto U_J^{\eta(\theta)}$. The semi-empirical coefficient, whose values are given in Figure 4.9, complements Lighthill's assumption of pure quadrupole-like aerodynamic sound sources by taking into account the angle dependency of the jet noise caused by sound refraction and convective effects.

[3]The number of averages in function of the window frame-length can be calculated by $N_{avg} = \frac{t_a \Delta f}{N_{overlap}}$, where $N_{overlap}$ is the overlap factor and Δf is the frequency bandwidth.

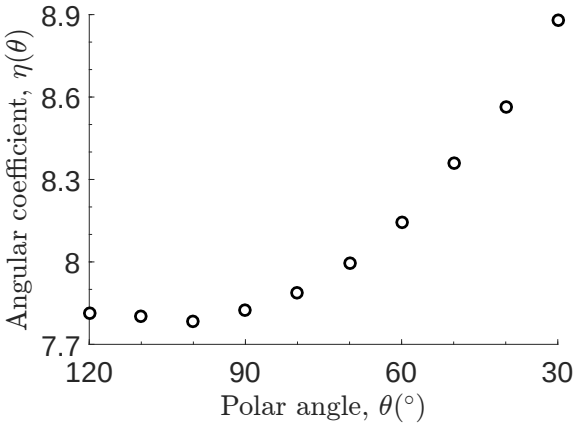

Figure 4.9 – Angular coefficient, $\eta(\theta)$, estimated experimentally at the JAR (LVA/UFSC) by Sirotto [43] for a jet exit condition corresponding to $M_a = 0.5$.

4.2.2 FWH surface analysis

Before analyzing the influence of the mesh resolution on the far-field acoustic results, is important to define the best-practice settings of the permeable FWH surface. Since transient pressure fluctuations signals are acquired by a surface mesh, two parameters are of particular interest: (1) the FWH grid resolution Δx_{FWH} and (2) the sampling frequency, f_s, in which the data is acquired. The first is important so the surface can properly sample the smaller wavelengths of interest and the later restricts the maximum frequency of analysis. Moreover, both parameters will influence the storage size of the FWH surface.

To analyze the influence of these two parameters on the far-field acoustic results, a parametric study is performed on the FWH surface settings of the medium resolution model. The 1/3 octave band far-field results obtained at the JAR (LVA/UFSC) are used as reference and a maximum frequency of interest $f_{\max}$=40 kHz is adopted. First, the sensitivity of the results to the spatial resolution is assessed while the sampling frequency is fixed in f_s=2$f_{\max}$, following the Nyquist criteria. Table 4.2 presents the setup configurations and Figure 4.10 presents the results.

Table 4.2 – FWH surface spatial resolution analysis: setup parameters and storage size.

Spatial resolution			
$D_J/\Delta x_{FWH}$	Δx_{FWH} (mm)	N_{ppw}[4]	Size (GB)
4	13	0.6	118
8	6.35	1.4	178
16	3.17	2.7	332
32	1.59	5.4	789

The results showed in Figure 4.10 presented a convergence trend by increasing the spatial resolution. The difference is noticeable for angles downstream the jet flow, where the results obtained with the coarsest resolution highly over-estimates the experimental results. Despite the fact that resolutions 8, 16 and 32 presents very similar results, only the results obtained by resolutions 16 and 32 collapses for all angles. Thus, for the sake of storage thrift, a resolution of 16 $D_J/\Delta x_{FWH}$ will be further adopted.

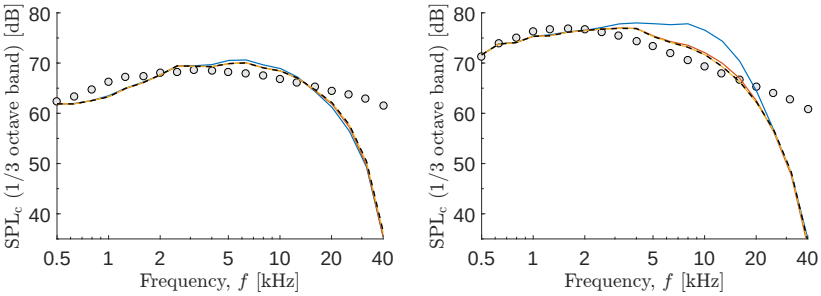

(a) $\theta = 120°$. (b) $\theta = 30°$.

Figure 4.10 – Parametric analysis of the FWH surface spatial resolution. Experimental results obtained at the JAR (LVA/UFSC) are represented by (○) symbols. Numerical results are represented by lines: $D_J/\Delta x_{FWH}$=4 (——), $D_J/\Delta x_{FWH}$=8 (——), $D_J/\Delta x_{FWH}$=16 (——) and $D_J/\Delta x_{FWH}$=32 (- - - -).

[4]The number of points per wavelength, $N_{ppw} = c_\infty/(f_{max}\Delta x_{FWH})$, is calculated in relation to the acoustic wavelength of the maximum frequency of interest, which is 40 kHz, and Δx_{FWH} is the minimum element size of the FWH surface grid.

After the definition of the FWH surface grid resolution, the sampling frequency is assessed following the configurations defined in Table 4.3.

Table 4.3 – FWH surface time resolution analysis: setup parameters and storage size.

Time resolution			
f_s	Δt_{FWH} (μs)	$\Delta t_{FWH} c_\infty / D_J$	Size (GB)
$2f_{max}$	12.5	0.0837	332
$4f_{max}$	6.25	0.0419	580
$8f_{max}$	3.12	0.0209	1150

Figure 4.11 compares the results obtained by different sampling rates. Is evident that the increasing of f_s allows the surface to compute more energy on the higher frequencies of the pressure power spectrum. Since the results obtained with f_s=8f_{max} are already very demanding in terms of storage, it was chosen to adopt this value as a best-practice setting for the remaining simulations.

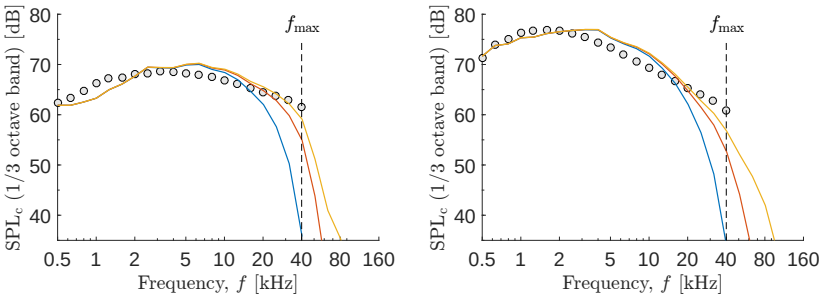

(a) $\theta = 120°$. (b) $\theta = 30°$.

Figure 4.11 – Parametric analysis of the FWH surface temporal resolution: 1/3 octave band sound pressure level for different polar angles. Experimental results obtained at the JAR (LVA/UFSC) are represented by (○) symbols. Numerical results are represented by lines: f_s=2f_{max} (——), f_s=4f_{max} (——) and f_s=8f_{max} (——).

4.2.3 Polar directivity

This section validates the far-field polar acoustic directivity obtained via the hybrid computational approach using the permeable FWH surface. The experimental results were performed at the JAR (LVA/UFSC). Figure 4.12 presents 1/3 octave band SPL results for different polar angles.

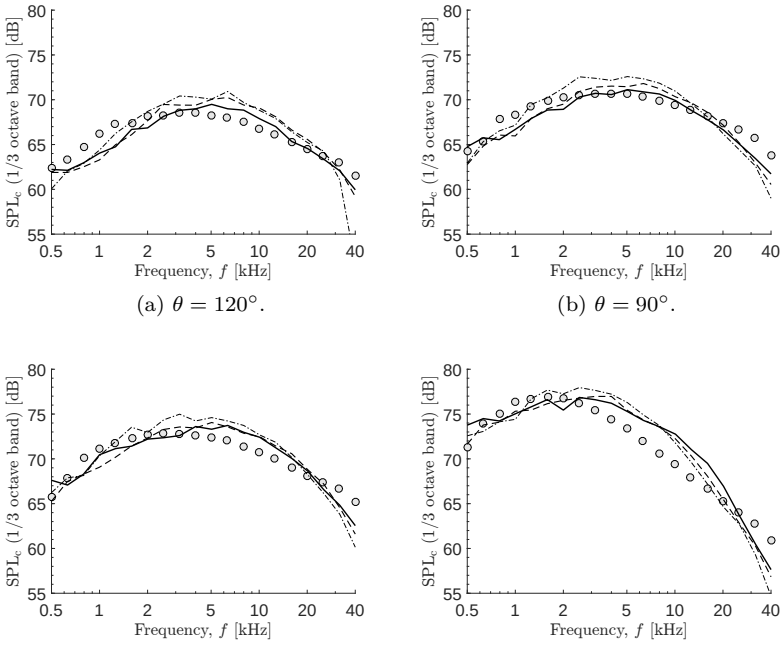

(a) $\theta = 120°$. (b) $\theta = 90°$.

(c) $\theta = 60°$. (d) $\theta = 30°$.

Figure 4.12 – 1/3 octave band sound pressure level for different observation polar angles. Experimental results obtained at the JAR (LVA/UFSC) are represented by (○) symbols. Numerical results are represented by lines: coarse (- · - · -), medium (- - - -) and fine (——).

In general, the simulation results presented in Figure 4.12 showed a good agreement with the experimental results in terms of magnitude, specially for polar angles upstream the nozzle. Even though a small deviation in magnitude is seen, the acoustic results obtained by all computational models are considered satisfactory. This can be an indication that the computational model is already converged, even for the coarse resolution case, since the grid resolution does not affect substantially the far-field acoustic results. However, the computational model fails at predicting the jet spectra shape at angles downstream the nozzle, overestimating the experimental results after 2 kHz. A possible source of error for this "bump" behaviour is the FWH surface length, which could be too exposed to hydrodynamic pressure fluctuations downstream the jet flow. da Silva [105] observed the same behaviour while performing a parametric analysis on the FWH surface length for a jet with similar conditions, and recommended a minimum FWH surface length of $30D_{\mathrm{J}}$ downstream the nozzle exit, which is larger than the one adopted by the current work.

The jet acoustic far-field polar directivity can be further verified by means of Overall Sound Pressure Level (OASPL), which computes the total spectral energy of the pressure fluctuations perceived at an observation position. The OASPL is computed as the sum of the pressure power spectrum frequency components within a specified bandwidth, as

$$\mathrm{OASPL} = 10\log_{10}\left(\sum_{f_{\min}}^{f_{\max}} 10^{\frac{\mathrm{SPL_c}}{10}}\right), \tag{4.3}$$

where $f_{\min}$ and $f_{\max}$ are the minimum and maximum frequency bands under consideration in Figure 4.12.

Figure 4.13 compares the simulated OASPL results obtained with different grid resolutions to experimental data measured at the JAR (LVA/UFSC). As one can observe, the predictions of the computational model are in good agreement with the experimental data. In all cases, the computational results are following the same trends as the experimental data. The results obtained with the coarse resolution grid over-estimates the reference data for the entire range assessed, presenting an maximum deviation of 1.4 dB. In counterpart, the results obtained with the medium and fine resolution grids are in good agreement with experimental data, presenting a difference no bigger than 0.6 dB from the reference results. Moreover, the influence of the grid for these two cases is small as the difference between results is no greater

than 0.3 dB for the entire range assessed.

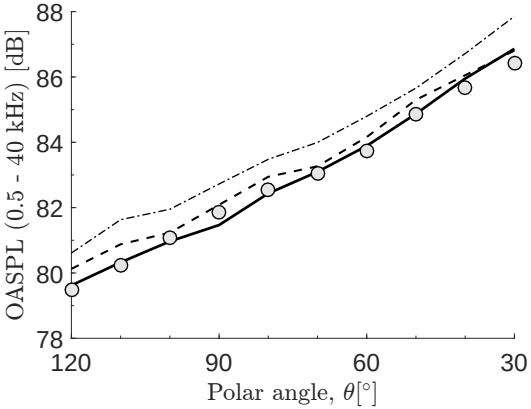

Figure 4.13 – OASPL computed from 0.5 to 40 kHz. Experimental results obtained at the JAR (LVA/UFSC) are represented by (○) symbols. Numerical results are represented by lines: coarse (- · - · -), medium (- - - -) and fine (——).

Despite the good agreement of the OASPL for the available experimental angles, more information is needed to confirm that the numerical model is able to predict the polar directivity pattern of the noise generated by a turbulent jet. Figure 4.14 extends the analysis by providing an overall picture of the numerical predictions of the acoustic polar directivity.

From Figure 4.14, one can verify that the far-field OASPL predictions present a highly directive polar pattern downstream the jet flow. This is in agreement with the directivity pattern observed by MacGregor et al. [106], which is illustrated in Figure 2.11. These authors states that the elementary noise generators, i.e. the turbulent eddies, of an subsonic, isothermal, turbulent jet produce a basic quasi-omnidirectional noise radiation pattern which is amplified downstream the jet flow due to convective effects. Furthermore, refraction effects caused by local velocity and temperature gradients are responsible for bending a portion of the sound waves away from the jet axis, giving rise to a "silent" zone at polar angles downstream the jet flow. Therefore, Figure 4.14 allows one to conclude that the numerical model is able to capture the convective and refractive effects suffered by the acoustical field generated by the turbulent jet flow, and that the hybrid computa-

tional methodology using the FWH surface provides a valid prediction of the jet's acoustic far-field polar directivity. This is observed for all grid resolutions assessed.

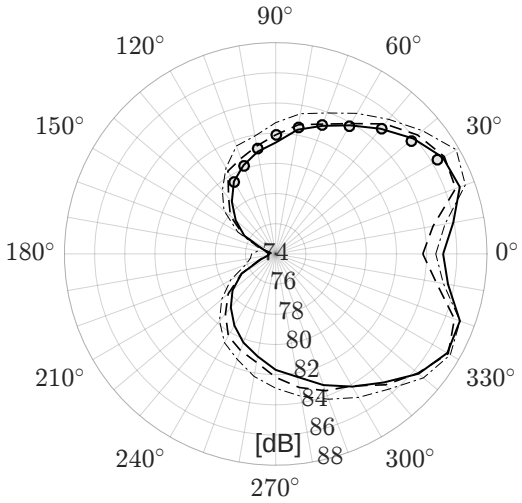

Figure 4.14 – Far-field polar directivity prediction. OASPL results computed from 0.5 to 40 kHz. Experimental results obtained at the JAR (LVA/UFSC) are represented by (○) and numerical results are represented by lines: coarse (- · - · -), medium (- - - -) and fine (——).

5 JET-PLATE INTERACTION NOISE

In this chapter, the computational model described in Section 3.2 is employed to investigate fundamental aspects of the installation noise phenomena by considering the interaction between a single-stream, cold, subsonic jet with $M_a = 0.5$ and a flat plate. Following the validation analysis conducted in Chapter 4, the numerical model with the fine resolution grid is used hereafter since it presented improved predictions, especially in terms of turbulence levels along the jet plume.

The surface is positioned parallel to the jet centerline according to a distance x_{te} from the nozzle exit to the plate's trailing edge (TE) and a radial distance, h, from the jet centerline. Figure 5.1 illustrates the conventions adopted to define the surface and far-field microphone positions.

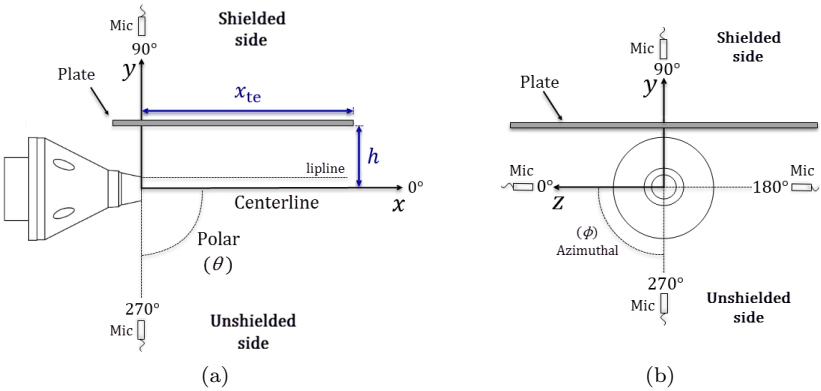

Figure 5.1 – Schematic representation of the case setup: (a) polar plane and (b) azimuthal plane. For clarity, real proportions of the plate are not maintained.

The plate dimensions are presented by Figure 5.2, which also defines a cartesian system (x_s,y_s,z_s), centered at the mid-span of the plate's trailing edge. The effect of the plate radial distance, h, on the jet flow and acoustics is investigated by three installation configurations, as defined in Table 5.2.

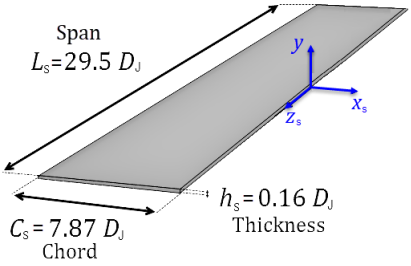

Figure 5.2 – Plate dimensions and TE based cartesian system.

Table 5.1 – Installation configurations.

Case	x_{te}/D_J	h/D_J
1	6	2
2	6	1.5
3	6	1

The rigid flat plate is treated with a no-slip condition and is discretized mainly by VR 10, except when the plate is close to the jet shear-layer, as in configuration 3 ($h/D_J = 1$). In this case, a small portion of the plate is also discretized by VR 11. Figure 5.3 allows for a better visualization of the computational mesh for case 3.

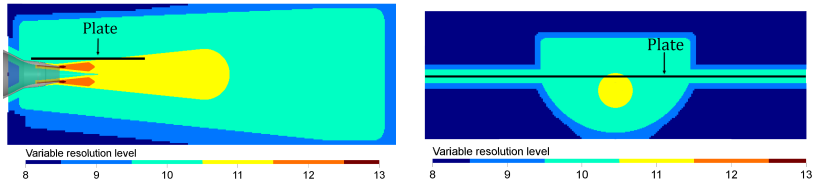

Figure 5.3 – Computational grid layout for installation configuration 3 ($h/D_J = 1$): (a) lateral view and (b) frontal view at the plate's TE axial position, $x_{te}/D_J = 6$.

Table 5.2 compares the simulation setup for the isolated and installed cases, showing that the inclusion of the plate on the computational domain increased the computational cost of the simulation by $\sim 12\%$. This is due to the addition of 42×10^6 elements in VR 10 to discretize the plate along its spam direction.

Table 5.2 – Jet-plate interaction simulation setup. All simulations were performed on a Linux Xeon E5-2690 2.9 GHz platform with 480 cores and 128 GB RAM.

	Grid resolution		Time resolution		Mesh size	Computational cost	
Case	$D_J/\Delta x$	Δx (mm)	Δt (μs)	$\Delta t c_\infty/D_J$	10^6 cells	Hours	kCPUh
Isolated	512	0.009	0.15	0.0010	806	84.7	44.8
Installed	512	0.009	0.15	0.0010	848	94.2	49.2

This chapter is organized as follows. Section 5.1 investigates the influence of the plate on the jet mean streamwise velocity, its standard deviation, and its spectrum. Section 5.2 assesses the jet near-field aiming at characterizing the regime of the pressure fluctuations incident on the plate. Finally, Section 5.3 provides an analysis of the installation effect on the jet far-field noise.

5.1 Flow field

This section investigates whether the plate modifies the flow field of the jet. Figure 5.4 presents contours of the jet mean flow field under different installation configurations.

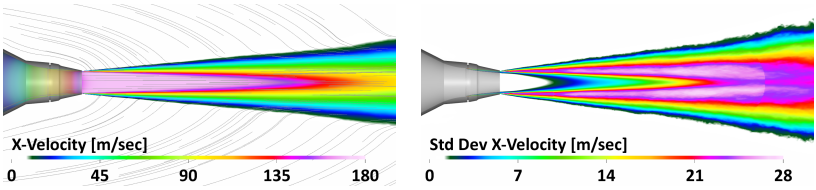

(a) Isolated jet.

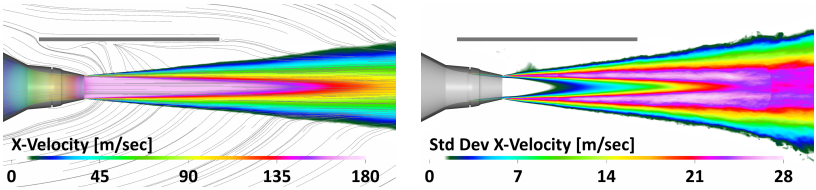

(b) Installation configuration 1: h/D_J=2.

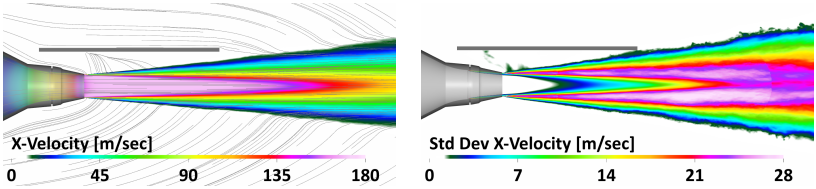

(c) Installation configuration 2: h/D_J=1.5.

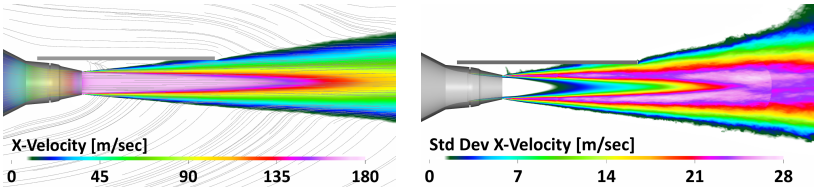

(d) Installation configuration 3: h/D_J=1.

Figure 5.4 – Streamwise velocity field for different jet-plate configurations. Left column: mean velocity and streamlines; right column: standard deviation.

Figure 5.4 shows that plate restricts the jet entrainment, but does not exert significant impact on the jet mean flow field. In fact, a small portion of the plate TE interacts with the mean flow only in the most intrusive case (h/D_J=1). Regarding the jet turbulence field, a few comments can be made over the modifications observed: 1) in configurations 2 and 3, the plate interacts directly with the turbulence field; 2) in configuration 3, a wall boundary layer is formed at the plate's TE. In order to quantify whether the plate changes the jet flow, a more quantitative analysis can be made in Figure 5.5, where a comparison of the mean flow at the jet's centerline and lipline is shown for the different installation configurations.

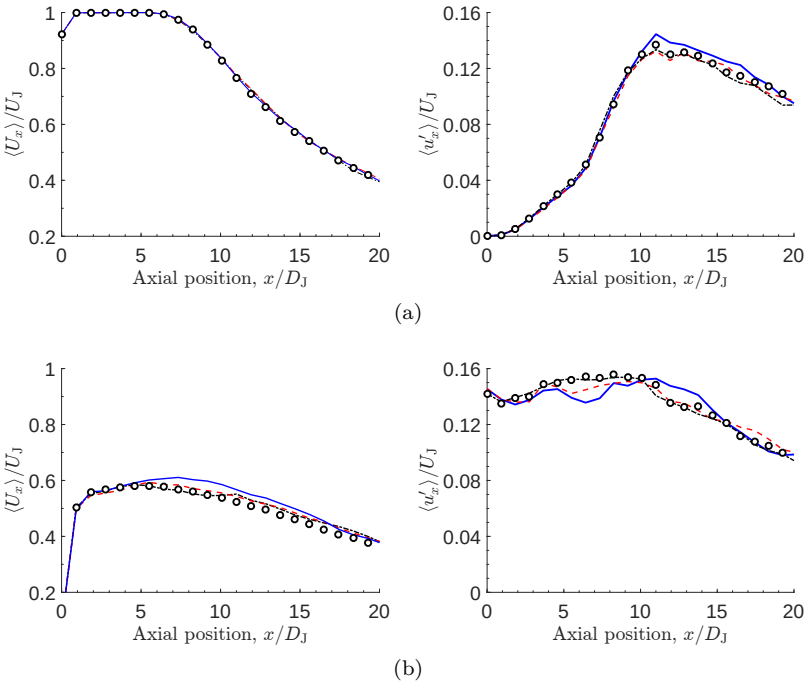

Figure 5.5 – Computational results of streamwise mean velocity (left column) and turbulence intensity (right column) along the jet (a) centerline and (b) lipline for different jet-plate configurations: isolated (○), h/D_J=1 (——), h/D_J=1.5 (- - - -) and h/D_J=2 (-·-·-).

Apart from a small increasing of the turbulence intensity peak level, the results in Figure 5.5a show no significant differences when comparing isolated and installed configurations along the jet centerline. Figure 5.5b shows that, when the surface is positioned farther away, there is no significant modifications on the mean flow along the jet lipline closer to the surface. However, when the plate is closer (h/D_J=1), the mean velocity is increased downstream the axial position of the surface TE while the turbulence intensity is reduced at the surface TE position.

Figure 5.6 complements the analysis of the installation effect on the jet's mean flow field by comparing radial profiles of streamwise velocity for isolated and installed configurations at distinct axial positions.

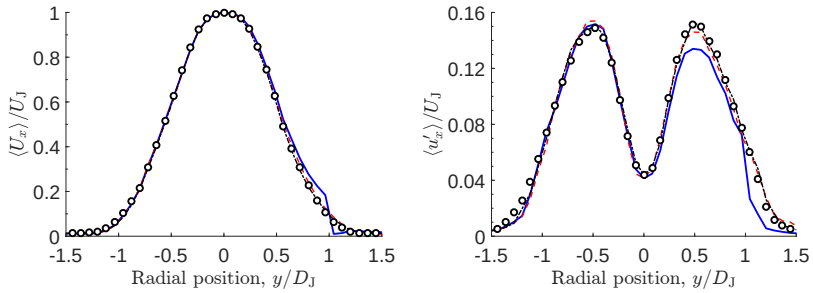

(a) x/D_J=6.

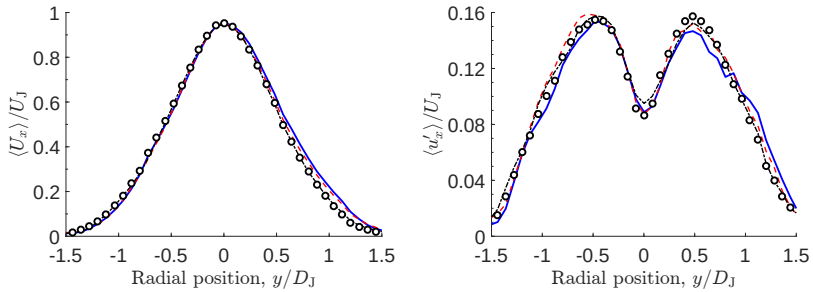

(b) x/D_J=8.

Figure 5.6 – Radial profiles of time-averaged streamwise velocity (left column) and turbulence intensity (right column) for different axial positions and jet-plate configurations: isolated (○), h/D_J=1 (——), h/D_J=1.5 (- - - -) and h/D_J=2 (-·-·-).

Figure 5.6 shows that the radial profiles only change significantly for the most intrusive configuration (h/D_J=1). In this case, it seems that the mean flow is slightly accelerated in the direction towards the surface while a drop on the turbulence levels is seen at the plate's TE axial position. Similar trends were verified in the literature for slightly different configurations [107, 108]. Therefore, despite small local modifications, one may conclude that the jet mean flow does not suffer substantial modifications due to the surface presence.

In addition to the mean flow, more information is needed to verify whether the plate modifies the turbulent structures of the jet flow. Thus, Figure 5.7b investigates the changes on the unsteady flow field of the jet for different installation configurations. For that, the velocity power spectrum is computed at the plate's TE axial position by probes P1 (centerline) and P2 (lipline) (see Figure 5.7a) in 25 Hz ($\mathrm{St}_{D_J} \sim 0.008$) narrow-bands and smoothed for a better visualization.

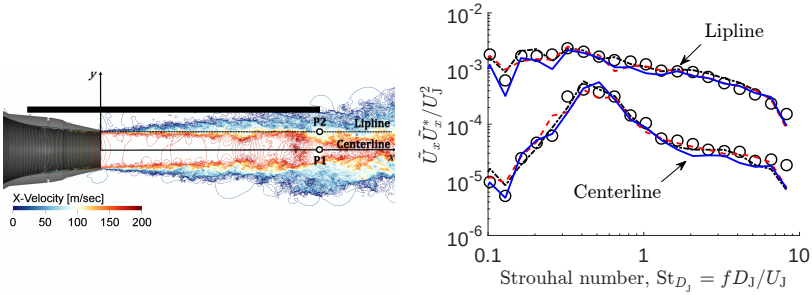

(a) Contours of transient U_x and probe positions.

(b) Smoothed streamwise velocity power spectrum.

Figure 5.7 – Installation effect on the jet streamwise velocity spectra at x/D_J=6: isolated jet (○), h/D_J=1 (——), h/D_J=1.5 (- - - -) and h/D_J=2 (-·-·-).

Figure 5.7 shows that the frequency content of the velocity field depends on the radial position, presenting a prominent peak around $\mathrm{St}_{D_J} \sim 0.4$ at the centerline and a broadband behaviour at the jet lipline. Moreover, one may state that the surface does not change the turbulent structures of the jet since the shapes and levels of the velocity spectra are not modified in any of these radial positions.

Similar to the investigation made by Cavalieri et al. [109], Figure 5.8 evaluates the impact of the surface on the downstream evolution of the velocity fluctuations at the jet centerline and lipline for a few chosen Strouhal numbers.

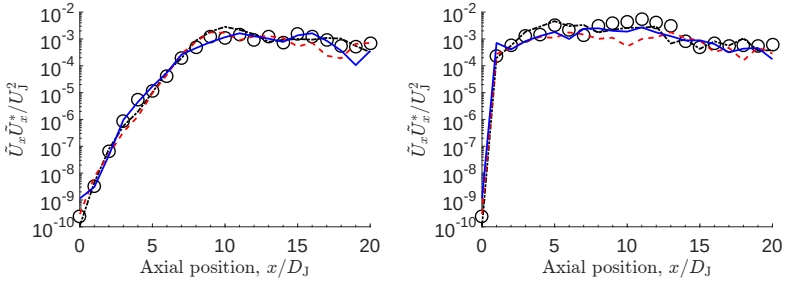

(a) $\mathrm{St}_{D_J} = 0.2$.

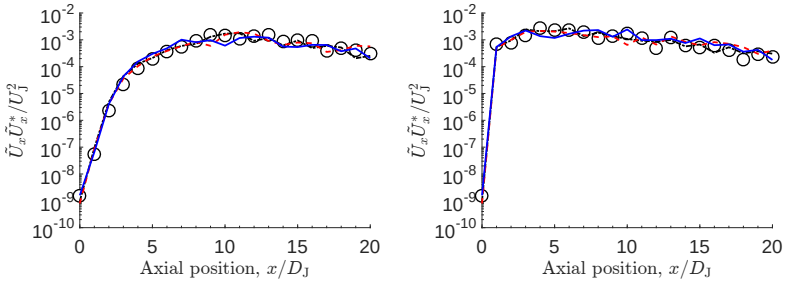

(b) $\mathrm{St}_{D_J} = 0.4$.

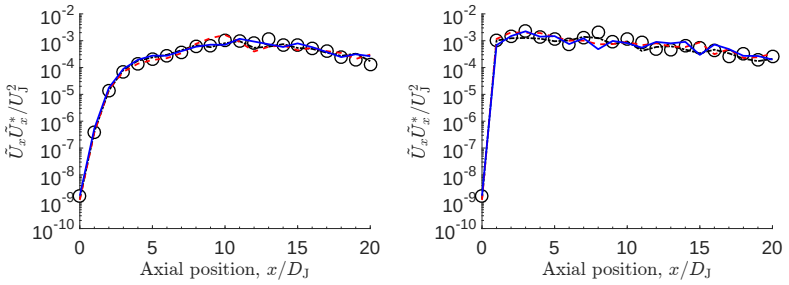

(c) $\mathrm{St}_{D_J} = 0.6$.

Figure 5.8 – Axial evolution of streamwise velocity fluctuations at the jet centerline (left row) and lipline (right row) for different Strouhal numbers: isolated jet (○), h/D_J=1 (——), h/D_J=1.5 (- - - -) and h/D_J=2 (-·-·-).

The results presented by Figure 5.8 shows that the axial evolution of the turbulent structures follows the same trends for all configurations at the Strouhal numbers assessed. At the centerline, the power spectrum levels presents a Strouhal number dependent exponential growth with the axial distance till a stagnation point from where the levels are kept constant. For the lipline, the results are less dependent on the Strouhal number and shows almost constant levels for the entire axial range.

As a general conclusion, the investigation on the jet's mean and transient flow field made in this section showed that, for the configurations under consideration, the plate does not modify significantly the jet flow. Thus, one may conclude that the plate will affect only the propagation of the pressure-field generated by an isolated jet. This observation makes plausible the use of source terms derived from free-jets to develop low-order models for jet-plate interaction problems.

5.2 Pressure near-field

As discussed in Section 2.2.1, two pressure regimes coexist in the jet near-field: (1) an evanescent hydrodynamic regime and (2) a propagating acoustic regime. Thus, when a solid plate is positioned at the vicinity of a turbulent jet flow, it is important to characterize the nature of the pressure-field incident upon the surface so that the mechanisms behind jet-plate interaction noise can be understood and properly modeled. Since this is a rather demanding task to be performed experimentally, this section aims at using the computational model to provide insight on (1) which regime characterizes the pressure fluctuations incident on the plate; and (2) verify whether the plate modifies the pressure field generated by the jet.

Figure 5.9 presents a qualitative visualization of the pressure fluctuations generated by the jet flow by means of dilatation fields, i.e. contours of pressure time-derivative $\partial p/\partial t$, whose colour bars are saturated in order to emphasize the time-derivatives related to the jet near-field.

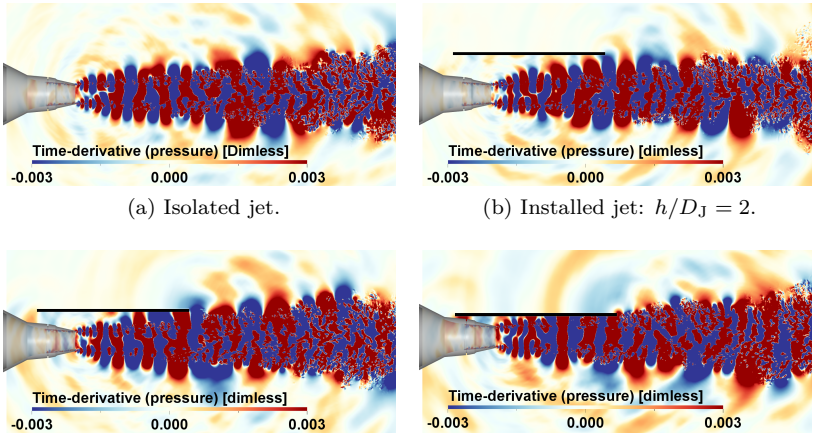

(a) Isolated jet.

(b) Installed jet: $h/D_\mathrm{J} = 2$.

(c) Installed jet: $h/D_\mathrm{J} = 1.5$.

(d) Installed jet: $h/D_\mathrm{J} = 1$.

Figure 5.9 – Computational predictions of the jet's pressure near-field: snapshots of dilatation field for different jet-plate configurations.

The presence of coherent pressure fluctuations within the jet shear-layer is evident on the contours showed by Figure 5.9. These hydrodynamic waves in the form of wavepackets are known to be a consequence of large-scale turbulent structures generated by Kelvin-Helmholtz instability mechanisms. Since the first observation of coherent structures in jet flows [110, 111], many studies have shown that the pressure disturbances generated by such structures can be modeled using linear instability theory, e.g. wavepacket models [112, 113]. A complete review of wavepackets and their relevance on the noise radiated by turbulent jet flows is provided by Jordan & Colonius [114]. Moreover, as can observed in Figure 5.9, the plate is interacting directly with the jet near-field in all installed configurations and a stronger interaction takes place as the plate becomes closer to the jet nozzle. However, a more quantitative analysis is needed so that the pressure regime incident on the plate can be characterized and the influence of the plate upon the pressure-field can be quantified.

Figure 5.10 presents results of the pressure power spectrum obtained at an radial position immediately below the plate's trailing edge. The results are obtained for isolated and installed configurations at the same position for the sake of comparison. All curves were obtained in 25 Hz narrow-bands ($\mathrm{St}_{D_\mathrm{J}} \sim 0.008$) using a Hanning window and smoothed to represent the mean trend.

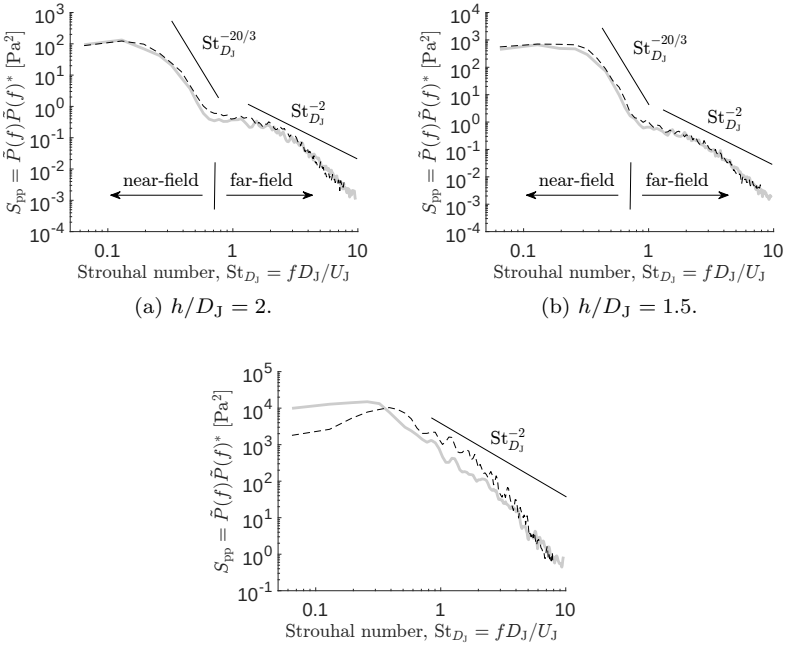

(a) $h/D_J = 2$.

(b) $h/D_J = 1.5$.

(c) $h/D_J = 1$.

Figure 5.10 – Pressure power spectrum at the plate trailing-edge position (x_s, y_s, z_s)=$(0, h/D_J, 0)$. Results obtained for different installation configurations. Isolated jet is represented by (- - - -) and installed jet for different radial positions by (——).

Figure 5.10 shows that when the plate is positioned at radial distances $h/D_J = 2$ and 1.5 is possible to characterize the regime of the incident pressure on the plate as a function of the Strouhal number. A clear dividing line at $\mathrm{St}_{D_J} = 0.7$ seems to be the transition point between near- and far-field behaviour, which is in accordance with the work of Lawrence [24]. When $\mathrm{St}_{D_J} > 0.7$, the plate interacts with an acoustic-field whose pressure fluctuations are characterized by an intensity decay $\propto \mathrm{St}_{D_J}^{-2}$. In this case, the incident pressure on the plate is reflected and scattered as the plate can be considered as a non-compact body. In counterpart, for low-Strouhal numbers below 0.7, the plate interacts with hydrodynamic pressure disturbances which predominate in terms of magnitude over the acoustical-field verified for

$\mathrm{St}_{D_\mathrm{J}} > 0.7$. In this case, the pressure disturbances are considered as non-compact noise sources and the scattering of the jet hydrodynamic field by the plate TE is expected to be the main mechanism associated to the installation effect on the far-field. Within the near-field, linear hydrodynamic pressure disturbances that tends to decay $\propto \mathrm{St}_{D_\mathrm{J}}^{-20/3}$ are verified for $0.3 < \mathrm{St}_{D_\mathrm{J}} < 0.7$, which is consistent with the work of Arndt et al. [37]. As a final observation, the installation effect on the pressure regime seems to be negligible when the plate is positioned at these radial distances as similar results were obtained for isolated and installed cases.

On the other hand, for the close-coupled case when $h/D_\mathrm{J} = 1$ (see Figure 5.10c), acoustic and hydrodynamic disturbances coexists for a larger range of Strouhal numbers as its not clear to identify the regime of the incident pressure on the plate. For this case, it would be necessary to employ more advanced methods, such as wavelet transform [34] or wavenumber transform [36], to isolate the acoustic and hydrodynamic pressure regimes within the jet near-field. Furthermore, the close proximity of the plate leads to strong interactions with the non-linear, rotational hydrodynamic field of the jet at the energy containing range (see Figure 2.9) and, as a consequence, the magnitude of the pressure spectra is increased by the plate at the lower Strouhal numbers.

Figure 5.11 compares the magnitude of the pressure power spectrum for installed cases showed in Figure 5.10. Is possible to observe that, for the cases when $h/D_\mathrm{J} = 2$ and 1.5, the pressure incident on the plate has nearly the same magnitude for Strouhal numbers > 0.7, which is a range associated to acoustic pressure fluctuations. For the lower Strouhal number range associated with hydrodynamic pressure disturbances, the magnitude of the pressure power spectrum increases as the radial distance decreases. For the case when $h/D_\mathrm{J} = 1$, the results indicate that the magnitude of the pressure field incident upon the plate is significantly increased for all Strouhal numbers and is not clear to distinguish the near-field from the far-field behaviour.

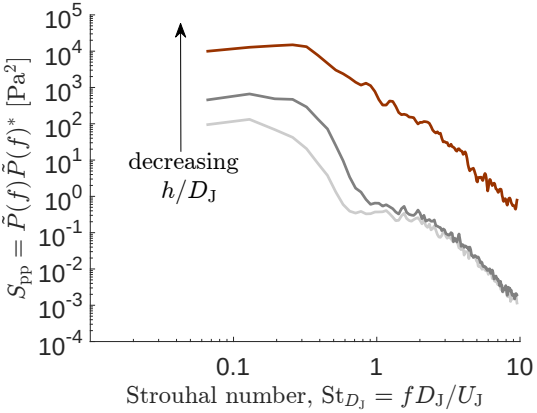

Figure 5.11 – Comparison of the pressure power spectrum immediately below the plate TE for different installation configurations: $h/D_\mathrm{J} = 2$ (——), $h/D_\mathrm{J} = 1.5$ (——), $h/D_\mathrm{J} = 1$ (——).

In general, the characterization of the pressure-field incident on the plate TE position presented in Figures 5.10 and 5.11 showed that the plate is subjected predominantly to hydrodynamic pressure disturbances related to the jet near-field, which grows in terms of magnitude as the radial distance decreases. At the same time, the low-Strouhal number content associated to the jet near-field enlarges as the radial distance decreases. This implies that the installation effect on the far-field due to the scattering of the jet's hydrodynamic field should be relevant for a wider range of Strouhal-numbers on which the noise sources can be considered non-compact.

As previously discussed in Section 2.2.1, is possible to characterize the pressure regime by observing the decay rate of the pressure fluctuations along the radial distance away from the jet flow. Figure 5.12 presents a comparison of the radial evolution of the jet pressure-field for some relevant Strouhal numbers. The results are obtained at the axial distance of the plate TE, $x_\mathrm{te}/D_\mathrm{J} = 6$. The radial range which the plate is positioned is highlighted in light grey area.

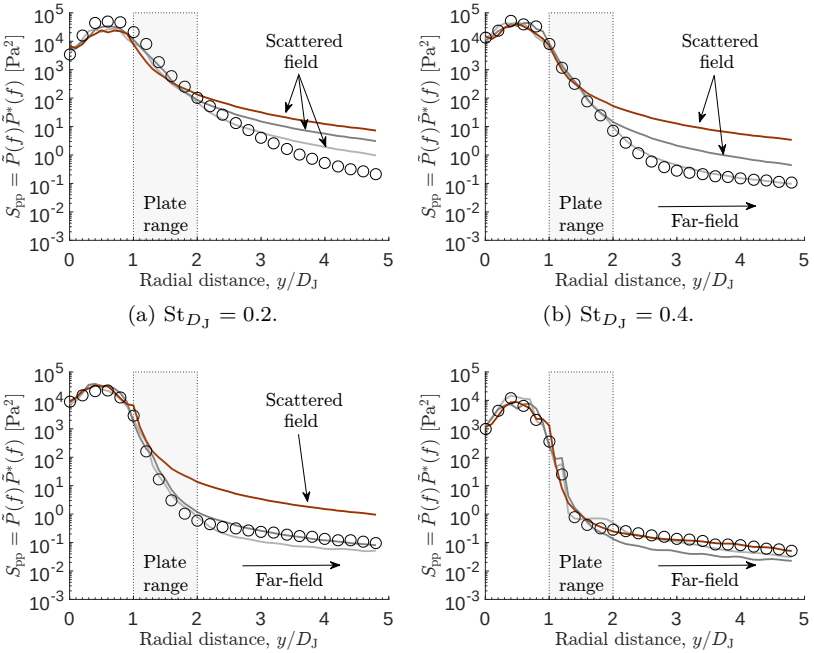

(a) $\mathrm{St}_{D_J} = 0.2$. (b) $\mathrm{St}_{D_J} = 0.4$.

(c) $\mathrm{St}_{D_J} = 0.6$. (d) $\mathrm{St}_{D_J} = 1$.

Figure 5.12 – Scattering effect on the radial decay of the pressure-field for different Strouhal numbers. Results obtained at the plate TE axial distance. Isolated jet results are represented by (○) symbols while installed jet results are represented by lines: $h/D_J = 2$ (——), $h/D_J = 1.5$ (——) and $h/D_J = 1$ (——).

As can be verified from Figure 5.12, the plate is positioned in a region characterized by an exponential decay of the pressure fluctuations for all cases, except for $h/D_J = 2$ and $\mathrm{St}_{D_J} = 1$ (see Figure 5.12d). This implies that, for the lower Strouhal numbers, the plate is interacting with hydrodynamic pressure disturbances characterized by a linear, irrotational regime. Moreover, it is possible to observe the scattering of the jet near-field by the plate as the decay rate of the pressure-field is altered from an exponential decay to an algebraic decay associated with propagating acoustic waves. This mechanism is verified to be dependent on the Strouhal number and on the plate radial distance.

For $\mathrm{St}_{D_\mathrm{J}} = 0.2$ (see Figure 5.12a), the scattering of the near-field is observed for the three plate positions, which indicates that noise sources at this wavelength are non-compact in relation to the characteristic length of the plate. For $\mathrm{St}_{D_\mathrm{J}} = 0.4$ and 0.6 is observed that the scattering depends on the relative radial distance of the plate as a change on the decay rate of an isolated jet is only observed when the plate is positioned at $h/D_\mathrm{J} = 1$ and $h/D_\mathrm{J} = 1.5$ for $\mathrm{St}_{D_\mathrm{J}} = 0.4$ and when $h/D_\mathrm{J} = 1$ for $\mathrm{St}_{D_\mathrm{J}} = 0.6$.

Moreover, for $\mathrm{St}_{D_\mathrm{J}} = 1$, no scattering effects are observed as the rate of decay of the pressure fluctuations remains the same of an isolated jet for all installed configurations. For this situation, the wavelength of the noise source is much smaller than the characteristic length of the plate and the main mechanism of the installation noise is attributed mainly to the reflection of acoustic waves rather than to the scattering of the hydrodynamic field.

5.3 Far-field acoustics

This section analyses the installation effect on the acoustic far-field. The results are obtained using the permeable FWH surface defined previously by Figure 3.12. To keep a low computational cost, the FWH surface encompasses only a portion of the plate, as can be verified in Figure 5.13.

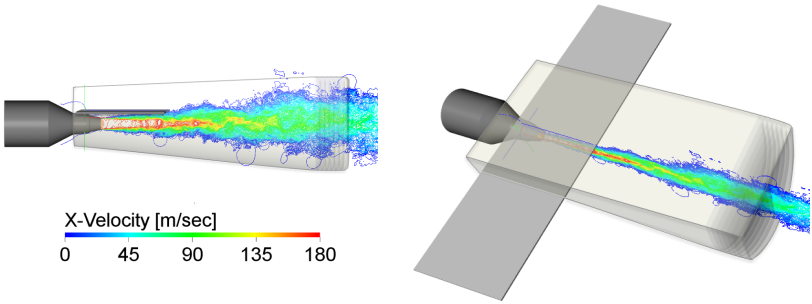

(a) (b)

Figure 5.13 – Permeable FWH surface along with the solid plate and contours of transient x-velocity: (a) lateral view and (b) perspective view.

After being propagated to the far-field microphone positions, the pressure signals are assessed in frequency domain by computing the pressure power spectrum in $\Delta f = 25$ Hz ($\mathrm{St}_{D_\mathrm{J}} \sim 0.008$) narrow-bands using the Welch's method, as done in Section 4.2. Moreover, the SPL data is corrected following the procedure described in Section 4.2.1.

5.3.1 Polar directivity

The far-field polar directivity is assessed at a radial distance of $41D_\mathrm{J}$ from the nozzle exit according to the polar array of probes defined in Figure 5.14.

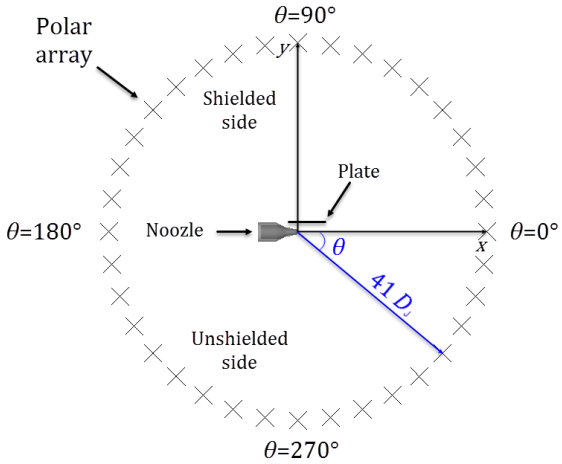

Figure 5.14 – Polar array of probes for far-field noise computation.

The installation effect is assessed in terms of relative delta sound pressure levels, ΔSPL, where the sound pressure level of the isolated jet, $\mathrm{SPL}_\mathrm{jet}$, are subtracted from the sound pressure levels of the installed cases, $\mathrm{SPL}_\mathrm{installed}$, as

$$\Delta\mathrm{SPL} = \mathrm{SPL}_\mathrm{installed} - \mathrm{SPL}_\mathrm{jet}. \tag{5.1}$$

Figure 5.15 presents results for the unshielded side of the surface. The computational results are compared with experimental results for different installation configurations and distinct polar angles.

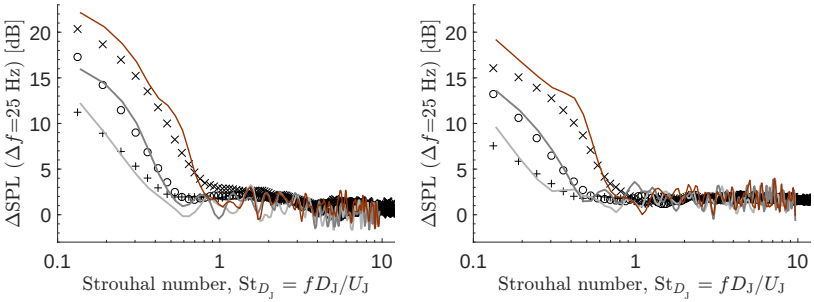

(a) $\theta = 240°$.

(b) $\theta = 270°$.

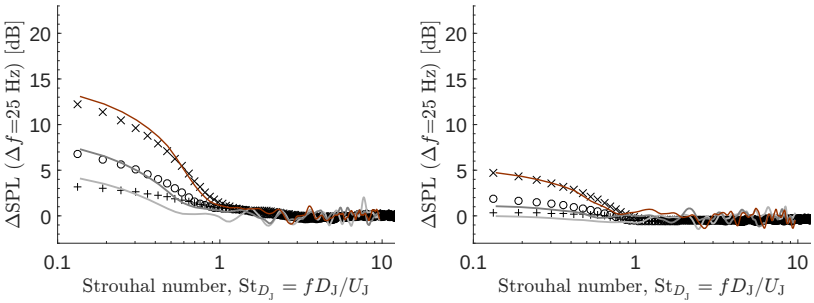

(c) $\theta = 300°$.

(d) $\theta = 330°$.

Figure 5.15 – Far-field, smoothed 25 Hz ($\mathrm{St}_{D_J} \sim 0.008$) narrow-band SPL at unshielded side in terms of installation delta. Experimental results JAR (LVA/UFSC) are represented by symbols and numerical by lines: $h/D_J = 2$ (+, ——), $h/D_J = 1.5$ (○, ——) and $h/D_J = 1$ (×, ——).

It is possible to verify in Figure 5.15 that the computational model was able to predict the trends related to installation noise: (1) augmentation on low Strouhal number due to the jet-surface interaction (JSI) noise and (2) jet-surface reflection (JSR) on the mid and high Strouhal numbers. The JSI is a consequence of the scattering of the jet near-field by the trailing edge of the solid plate, as previously observed in Figure 5.12. The augmentation is intensified and covers a wider range of Strouhal numbers as the plate becomes closer to the jet shear-layer. This is due to the intrinsic nature of the jet near-field interacting with the plate, as previously observed in Figure 5.11. Moreover, the JSI effect is clearly more relevant for polar angles upstream the nozzle while the isolated jet noise dominates the spectra at polar angles downstream.

The JSR seen for Strouhal numbers above 1 is verified to be relevant also for the lower angles and follows the trend found in literature of an increase in 3 dB over the isolated jet noise due to the sum of incoeherent sound reflections.

The polar directivity of the jet is verified through absolute and relative OASPL levels in Figure 5.16. The relative, installation delta OASPL values are obtained in the same fashion as the ΔSPL, i.e. by subtracting the isolated jet noise contribution from the installed levels.

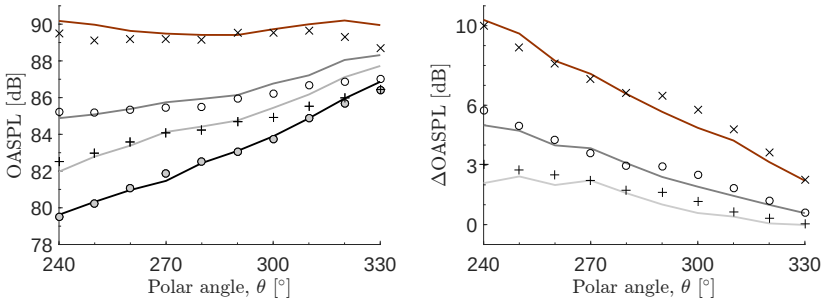

(a) Absolute levels.

(b) Delta levels.

Figure 5.16 – OASPL computed from $\mathrm{St}_{D_\mathrm{J}} \approx 0.16$ to $\mathrm{St}_{D_\mathrm{J}} \approx 12.9$ (0.5 to 40 kHz) at the unshielded side. Experimental results JAR (LVA/UFSC) are represented by symbols and numerical by lines: isolated (○,——), $h/D_\mathrm{J} = 2$ (+,——), $h/D_\mathrm{J} = 1.5$ (○,——) and $h/D_\mathrm{J} = 1$ (×,——).

It is observed in the absolute OASPL results presented in Figure 5.16a that the overall levels are significantly increased for the installed cases, specially for polar angles upstream the nozzle. Nevertheless, the installation effect is also has a non-negligible contribution to the overall levels for polar angles downstream. For the most intrusive case ($h/D_\mathrm{J} = 1$), the OASPL levels are in the same order of magnitude for all angles. This suggests that the contribution of the installation effect is also relevant for polar angles downstream the nozzle for this configuration, a supposition which will be further addressed in Section 5.4.2.

Figure 5.16b shows that the installation effect is predominantly verified for polar angles upstream the nozzle, leading to an augmentation on the far-field noise up to 10 dB for the most intrusive case ($h/D_\mathrm{J} = 1$). In general, one can verify in Figure 5.16 that the simu-

lation results are in good agreement with the experimental data and, thus, the computational model can be considered validated for the investigation of the installation effect on jet noise.

Complementing the experimental measurements, which are limited to polar angles at the unshielded side, Figure 5.17 presents an overall, Strouhal number dependent picture of the far-field acoustic polar directivity in terms of relative installation delta sound pressure levels.

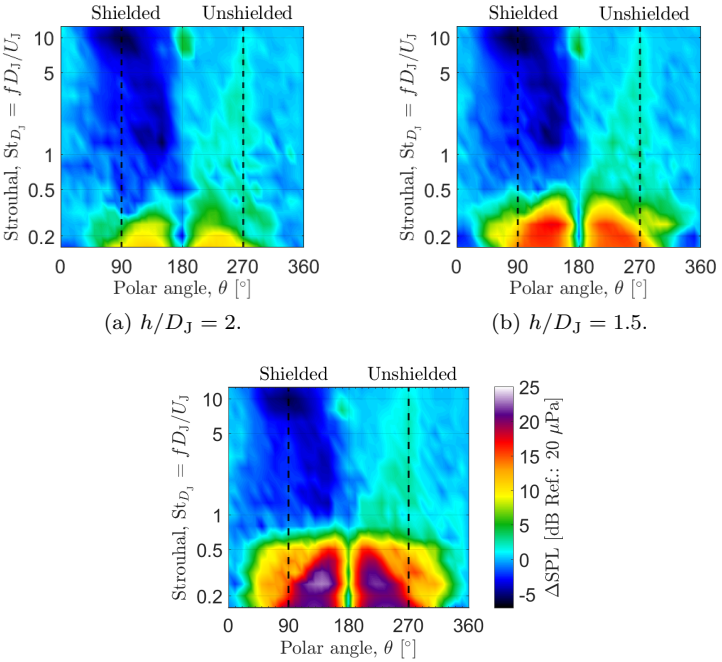

(a) $h/D_J = 2$. (b) $h/D_J = 1.5$.

(c) $h/D_J = 1$.

Figure 5.17 – Installation effect on the far-field SPL polar directivity for different jet-plate configurations. The polar array is centered at the nozzle exit, $(x/D_J, y/D_J, z/D_J, R/D_J) = (0, 0, 0, 41)$. Results expressed in terms of SPL installation delta (installed minus isolated jet).

As can be seen in Figure 5.17, the installation effect on the jet polar directivity is highly dependent on the Strouhal number. For high Strouhal numbers, the surface acts as a non-compact body and significantly alters the jet polar directivity by (1) shielding the acoustic

field at angles around $\theta = 90°$ and (2) reflecting the sound waves to the unshielded side in approximately 3 dB for polar angles around $\theta = 270°$. For low Strouhal numbers, the surface scatters the jet near-field, increasing the SPL levels above the isolated jet. The scattering effect covers a wider range of Strouhal numbers as the plate becomes closer to the jet shear-layer. Furthermore, the directivity for low Strouhal number appears to assume a cardioid-like shape as the maximum radiation occurs at polar angles upstream the nozzle for both unshielded and shielded sides of the plate. The peak Strouhal in which the scattering effect is maximum is observed to be $\mathrm{St}_{D_\mathrm{J}}$=0.26 ($\sim$ 800 Hz) for all cases.

Figure 5.18 aims at the verification of the polar directivity pattern for two relevant Strouhal numbers: (a) $\mathrm{St}_{D_\mathrm{J}}$=0.26, which is the Strouhal number where the installation noise associated with JSI effect has it's maximum contribution and (b) $\mathrm{St}_{D_\mathrm{J}}$=1, where jet-surface reflection is the main mechanism associated to the presence of the plate.

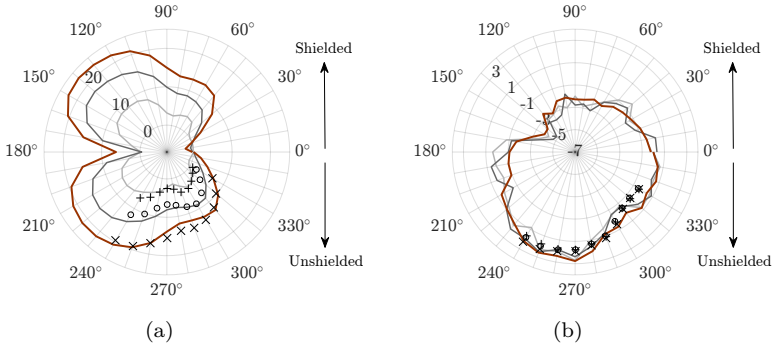

Figure 5.18 – Installation effect on the jet polar directivity pattern for (a) $\mathrm{St}_{D_\mathrm{J}}$=0.26 and (b) $\mathrm{St}_{D_\mathrm{J}}$=1. Experimental results (LVA/UFSC) are represented by symbols and numerical by lines: $h/D_\mathrm{J} = 2$ (+, ——), $h/D_\mathrm{J} = 1.5$ (○, ——) and $h/D_\mathrm{J} = 1$ (×, ——). Results expressed in terms of ΔSPL, which were computed in 1/3 octave bands.

The experimental results for the polar angles available are presented in Figure 5.18 and the good agreement observed gives confidence on the use of the numerical model to investigate the installation effect on the jet radiation pattern as a function of the Strouhal number. The installation effect for the most relevant Strouhal number ($\mathrm{St}_{D_\mathrm{J}}$=0.26) is verified in Figure 5.18a to have a radiation pattern that resembles a cardioid shape quasi-symmetric at the shielded and unshielded sides.

The maximum radiation levels were observed to happen at polar angles upstream the nozzle ($\theta = 140°$ and $\theta = 220°$). This radiation pattern is expected as, for this Strouhal number, the acoustic wavelength is ∼0.42 m, which is of the same order of the plate chord. Thus, the plate can't be considered as acoustically compact nor non-compact and the acoustic radiation assumes a directivity pattern whose shape is a transition from a compact dipole to the one of a non-compact cardioid. Moreover, the JSI effect associated with the scattering of the jet near-field is observed to be dependent on the plate distance as the closer the plate is to the jet shear-layer, the stronger is the magnitude of the pressure near-field interacting with the plate (see Figure 5.11).

On the other hand, the results for $\mathrm{St}_{D_\mathrm{J}}$=1 shown in Figure 5.18b allow to observe that the JSR mechanism is dependent only on the polar angle as any relevant differences in magnitude were observed for different plate distances. This is expected as the wavelength for this Strouhal number is much smaller than the characteristic length of the plate. Thus, the main mechanism associated with the installation effect is the reflection of the acoustic waves. The maximum radiation for this Strouhal number occurs for polar angles around $\theta = 270°$, with a magnitude of 3 dB, which is in accordance with results available in the literature [24, 45]. The shielding of the sound waves is verified for angles around $\theta = 90°$, where the installation delta assumes negative levels, meaning sound pressure levels below the ones verified for the isolated jet. Interestingly, a valley on the sound radiation magnitude is seen for angles around $\theta = 150°$, which could be associated with a destructive interference effect caused by the diffraction of the sound field at the plate's leading edge.

In Figure 5.19, the effect of the plate distance on the magnitude of the installation effect for $\mathrm{St}_{D_\mathrm{J}}$=0.26 is further investigated. The results are obtained for $\theta = 90°$ and 270° corresponding to the shielded and unshielded sides of the plate, respectively.

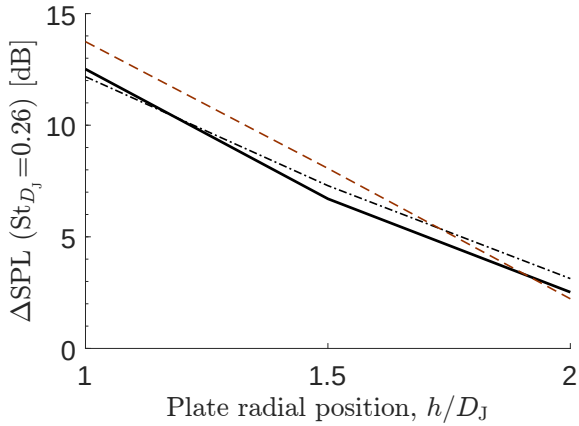

Figure 5.19 – Installation delta SPL for St_{D_J}=0.26 as a function of the plate radial distance. Experimental (——) and numerical (-·-·-) results at unshielded side (θ, ϕ)=(90°, 90°). Numerical results for shielded side (θ, ϕ)=(90°, 270°) are represented by (- - - -).

By comparing the simulation and experimental results, it is possible to verify in Figure 5.19 that the numerical results follow the same trend observed experimentally. The installation effect is observed to increase exponentially with the plate distance at both shielded and unshielded sides, which is represented by an almost linear increase of the installation delta levels in logarithmic scale. As previously verified in Figure 5.12, for this Strouhal number, the plate is positioned in a region predominantly characterized by an linear, non-rotational hydrodynamic field which has an exponential dependence with the radial distance. Thus, as the plate comes closer to the jet, the magnitude of the pressure fluctuations incident on the plate also follows the same trend. This implies that the magnitude of the installation effect on the far-field noise caused by the JSI mechanism is highly correlated with the pressure field interacting with the plate TE.

5.4 Surface pressure field

In this section, the computational model is further explored to assess the pressure field information acquired on the plate's surface and to assess its influence on the far-field noise. As verified earlier in Section 5.2, the pressure field incident upon the plate is characterized by a hydrodynamic regime with relevant spectral content at Strouhal numbers between 0.1 and 1. Figure 5.20 presents contours of SPL obtained at the plate surface for a Strouhal number range relative to hydrodynamic pressure perturbations for distinct installation configurations.

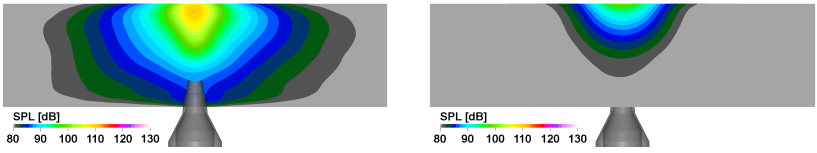

(a) Installed jet: $h/D_J = 2$.

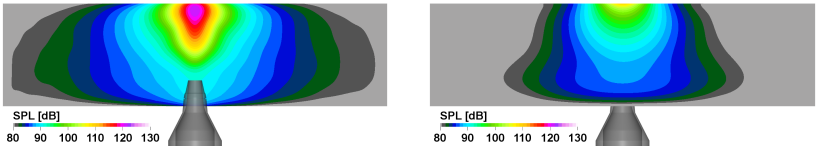

(b) Installed jet: $h/D_J = 1.5$.

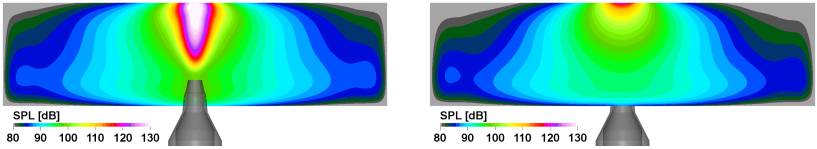

(c) Installed jet: $h/D_J = 1$.

Figure 5.20 – Sound pressure level distribution at the unshielded (left column) and shielded (right column) sides of the solid plate for different installation configurations. The results are computed from St_{D_J}=0.16 to St_{D_J}=1 (0.5 to 3 kHz).

The SPL contours presented in Figure 5.20 shows that the higher SPL are verified in regions close to the plate TE for all configurations and at both shielded and unshielded sides. Moreover, the plate is subjected to high SPL levels along it's spanwise direction, especially for the most intrusive cases, as illustrated by Figures 5.20b and 5.20c. This suggests that information of the pressure field on the whole plate's surface is relevant for the installation effect on the jet noise.

In order to assess how the pressure fluctuations incident upon the plate contributes to the far-field sound, a solid FWH formulation is employed. The results on the whole plate surface are acquired during the transient flow simulations by a mesh with spatial resolution equal to 0.8 mm and a sampling rate of 834 kHz, which complies by far the requirements for the permeable FWH surface investigated in Section 4.2.2. Later, these results are post-processed in PowerACOUSTIC 4.0a., which employs a solid FWH integral formulation to compute the sound at far-field observation points. The computational cost of such approach lies around 190 GB of storage, for all simulations. As discussed in Appendix A.4, the solid FWH formulation for a static solid body retrieves Curle's equation, where a surface distribution of dipole noise sources represents the sound generation due to unsteady forces acting upon the turbulent field in addition to Lighthill's quadrupole noise source term.

5.4.1 Noise source breakdown

The possibility to breakdown the relevant noise sources associated with the installation effect by employing computational approaches involving permeable and solid FWH surfaces is proposed and investigated in this section. If we consider that the installation noise is composed by two main noise sources, given by (1) the jet noise contribution (quadrupoles) and (2) the plate contribution (dipoles), it is possible to recover the total installation noise, $\mathrm{SPL}_{\mathrm{installed}}$, by an incoherent[1] sum of the noise sources, as

$$\mathrm{SPL}_{\mathrm{installed}} = 10\log_{10}\left(10^{\frac{\mathrm{SPL}_{\mathrm{jet}}}{10}} + 10^{\frac{\mathrm{SPL}_{\mathrm{plate}}}{10}}\right), \tag{5.2}$$

[1] In the case of two incoherent sound sources, interference effects in a observation point are negligible as the phase of the frequency components of the sources are assumed to be uncorrelated.

where $\mathrm{SPL}_{\mathrm{jet}}$ is contribution of the isolated jet noise, computed with the permeable FWH surface, and $\mathrm{SPL}_{\mathrm{plate}}$ is the plate contribution to the far-field noise, which is computed by the solid FWH surface.

Figure 5.21 presents the results for distinct installation configurations and polar angles. The sound spectra are computed in 25 Hz narrow bands ($\mathrm{St}_{D_\mathrm{J}}$=0.008) at a radial distance $41D_\mathrm{J}$ from the nozzle exit, following the polar angle convention defined for the experimental measurements (see Figure B.2).

In general, the results presented in Figure 5.21 shows that it is possible to represent the installation noise by a superposition of the isolated jet and the plate contributions as the incoherent sum of these noise sources presented a good agreement when compared to the experimental results. Therefore, the use of a solid FWH surface to compute the noise sources associated with the pressure fluctuations incident on the plate surface proves to be a useful approach to assess the installation noise. Moreover, the following observations can be made over the results presented in Figure 5.21:

- The plate contribution to the far-field noise is verified to have a predominant influence at low Strouhal numbers. Moreover, the noise associated with the solid plate becomes more relevant as the plate becomes closer to the jet flow. This is in agreement with the observations made in Section 5.2, where it was shown that the plate scatters the near-field of the jet flow for Strouhal numbers $\mathrm{St}_{D_\mathrm{J}} < 1$;

- For Strouhal numbers above 1, the isolated jet noise source is the dominant noise mechanism on the sound spectra. This is verified for all installation configurations and polar angles assessed;

- The plate contribution predominates over the isolated jet contribution for polar angles upstream the jet flow. As mentioned before, this is observed only for low Strouhal numbers;

- For angles downstream the jet flow, the jet mixing noise predominates over the plate contribution, even for low Strouhal number. However, the plate contribution overcomes the isolated jet noise for the most intrusive installation configuration (h/D_J=1).

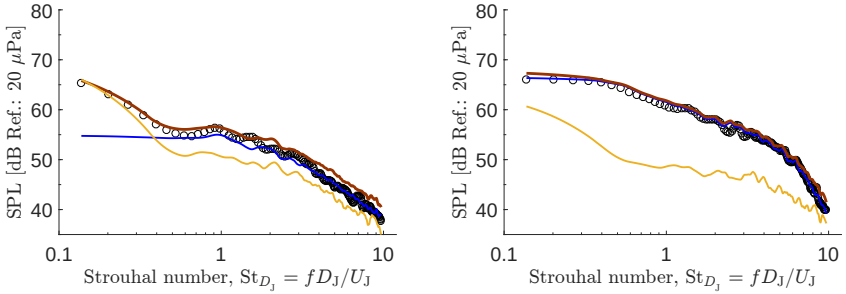

(a) h/D_J=2.

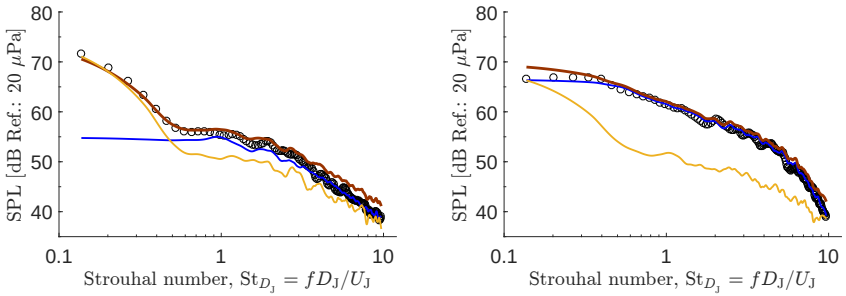

(b) h/D_J=1.5.

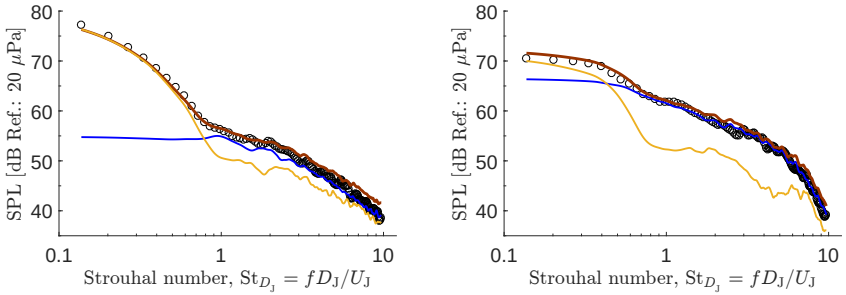

(c) h/D_J=1.

Figure 5.21 – Noise source decomposition for different installed cases for $\theta = 240°$ (left column) and $\theta = 330°$ (right column). Numerical results: $\mathrm{SPL}_{\mathrm{jet}}$ (——), $\mathrm{SPL}_{\mathrm{plate}}$ (——) and $\mathrm{SPL}_{\mathrm{installed}}$ (——). Experimental results obtained at the JAR (LVA/UFSC) are represented by (○).

5.4.2 Far-field polar directivity

After confirming that the installation effect can be described by the contributions of two distinct noise sources and having validated an approach to decompose them computationally using different FWH formulations, it is reasonable to employ this approach to further investigate the contributions of each noise source to the far-field polar directivity. Figure 5.22 presents results of OASPL obtained using the noise source breakdown approach described and validated in the previous section. Experimental results obtained at the JAR (LVA/UFSC) are presented so that one can easily verify whether the numerical results follows the correct sound directivity trends.

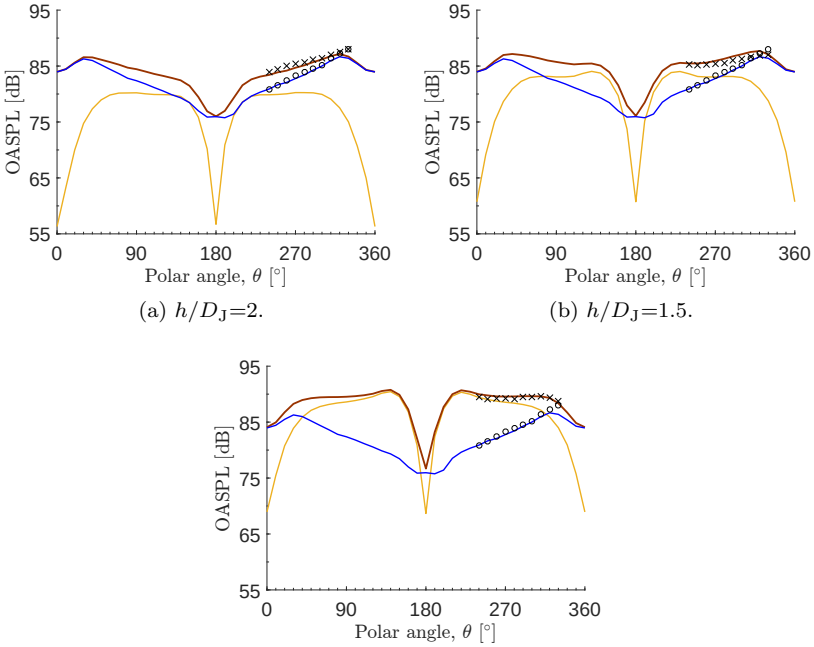

(a) h/D_J=2.

(b) h/D_J=1.5.

(c) h/D_J=1.

Figure 5.22 – Installation noise sources contributions to the far-field polar directivity: SPL_{jet} (——), SPL_{plate} (——) and $SPL_{installed}$ (——). Experimental results obtained at the JAR (LVA/UFSC) are represented by symbols: isolated (○) and installed (×). Results computed from St_{D_J}= 0.16 to 12.9 (0.5 to 40 kHz) in 1/3 octave bands.

Three general observations can be made from the results showed in Figure 5.22: (1) all noise sources contributions are symmetric around $\theta = 180°$; (2) the isolated jet noise contribution predominates in all cases for polar angles downstream the jet flow (around $\theta = 0°$) and (3) the plate contribution to the far-field polar directivity is dependent on the plate's radial distance and on the polar angle. For the case which the plate is farther away (see Figure 5.22a), the contribution of the isolated jet predominates for the entire range of polar angles, especially for angles downstream the jet flow. Moreover, the plate contribution is verified to have a dipole radiation pattern for this case. As the plate becomes closer to the jet flow, its contribution overcomes the isolated jet contribution for a wider range of polar angles. In fact, the plate contribution for the most intrusive case (see Figure 5.22c) is predominant for almost all polar angles, being negligible only angles close to the jet axis.

Figure 5.23 complements the analysis by comparing the plate contributions for different installation configurations. The results are expressed in terms of installation delta, i.e. installed minus isolated OASPL levels.

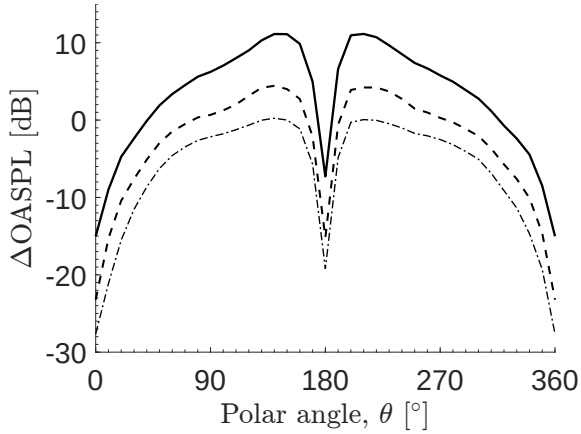

Figure 5.23 – Plate contribution to the far-field polar directivity. Comparison between different radial positions in terms of installation delta: h/D_J=2 (-·--·-), h/D_J=1.5 (- - - -) and h/D_J=1 (——).

It is possible to verify in Figure 5.23 that the noise increase caused by the plate contribution presents a maximum radiation for the polar angles $\theta = 140°$ and $210°$ for all cases. Moreover, the directivity pattern is symmetric for all cases and resembles a dipole radiation shape as a valley is seen at $\theta = 180°$ and at very sharp angles downstream the jet flow, i.e. for polar angles around $\theta = 0°$.

In order to have an insight on how the directivity pattern of the noise radiated by the plate is composed, the acoustic radiation pattern as a function of the Strouhal number is further assessed. Having in mind the concept of acoustically compact and non-compact bodies, and how it should influence the radiation pattern, is convenient to define the adimensional wavenumber, kC_s, which relates the acoustic wavenumber, $k = 2\pi f/c_\infty = 2\pi/\lambda$, to the relevant characteristic length of the plate, which in this case is the plate's chord length, C_s, defined in Figure 5.2. Figure 5.24 shows results the radiation patterns for three relevant Strouhal numbers. The SPL results are obtained in 10 Hz ($\mathrm{St}_{D_\mathrm{J}}$=0.0032) narrow bands and are normalized by the maximum value verified for each case. The results are obtained for a polar array centered in the mid-span of the plate TE, for a distance of $R_\mathrm{p}/D_\mathrm{J}$=41, according to the plate TE based cartesian system defined in Figure 5.2.

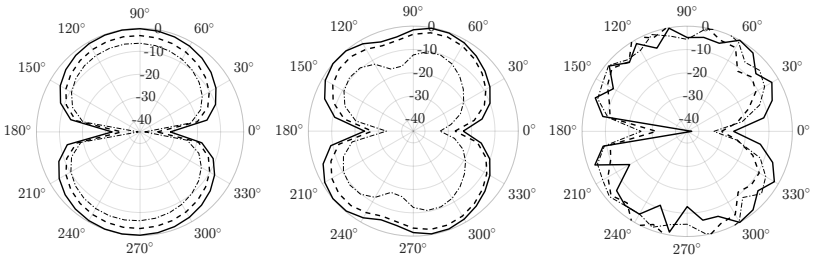

(a) $\mathrm{St}_{D_\mathrm{J}}$=0.01; ($kC_\mathrm{s}$=0.22).

(b) $\mathrm{St}_{D_\mathrm{J}}$=0.26; ($kC_\mathrm{s}$=6).

(c) $\mathrm{St}_{D_\mathrm{J}}$=2; ($kC_\mathrm{s}$=45).

Figure 5.24 – Solid plate far-field polar directivity for different Strouhal numbers and installation configurations: h/D_J=2 (- · - · -), h/D_J=1.5 (- - - -) and h/D_J=1 (——).

The results shown in Figure 5.24a present a dipole-like directivity pattern. This is in accord with Curle's theory as, for this case, the plate is considered as an acoustically compact body since $kC_s << 1$. For the case where the wavelength is in the order of the plate chord (see Figure 5.24b), the directivity pattern resembles the one of a cardioid. For the case where the wavelength is much smaller than the plate's chord (see Figure 5.24c), the radiation pattern still resembles the one of a cardioid, but no significant differences in magnitude are verified for the distinct plate radial distances.

6 CONCLUSIONS

This work presented a computational investigation on fundamental aspects related to the jet noise installation effects by considering the interaction between a single-stream, cold jet flow issued by a round nozzle with $M_a = 0.5$ and a flat plate. The numerical investigation was conducted using a commercial package based on a hybrid approach involving the Lattice-Boltzmann method and a turbulence model to simulate high-subsonic flows. The far-field noise predictions were obtained using the FWH integral formulation.

To evaluate how accurate is the computational model for the prediction of jet noise, a validation analysis was presented in Chapter 4 by considering the case of an isolated jet flow. The analysis focused on (1) investigating the flow and acoustic results sensitivity to the numerical grid resolution and (2) checking the requirements necessary for an efficient computation of the far-field noise using a permeable FWH surface. The computational model proved to be robust since both flow and acoustic results showed a small dependency on the grid resolution. The fine resolution grid was chosen to conduct the investigations on the installation effect since it showed improved results, especially in terms of turbulence levels at the nozzle exit. Moreover, the parametric analysis on the requirements of the permeable FWH surface proved to be essential for an effective computation of the far-field noise as the results are highly overestimated if the FWH surface is not properly configured. In general, the computational model achieved a good agreement with experimental results for both flow and far-field acoustic predictions. The computational cost was considered feasible since a simulation using a fine resolution grid requires 44.8 kCPUh ($\sim$ 4 days) of calculations with the computational resources available, generating about 1 TB of data.

The investigation of the jet-plate interaction noise was presented in Chapter 5, which comprises four parts: (1) the effect of the plate on the jet flow field (Section 5.1); (2) the characterization of the pressure field incident on the plate (Section 5.2); (3) the installation effect on the far-field acoustics (Section 5.3) and (4) the use of a solid FWH surface to isolate and investigate the plate contribution to the far-field noise (Section 5.4).

The influence of the plate on the mean and unsteady velocity fields was investigated in Section 5.1. The results suggest that, for the installation configurations under consideration, the plate does not modify significantly the jet flow.

A characterization of the pressure field interacting with the plate was performed in Section 5.2, which led to the following conclusions: (1) the near- of far-field is dependent on the Strouhal number and on the radial distance from the jet shear-layer; (2) a dividing line at $\mathrm{St}_{D_\mathrm{J}} = 0.7$ seems to be the transition point between near- and far-field pressure regimes; (3) the plate is positioned in a region characterized by a linear hydrodynamic field, whose pressure fluctuations decay exponentially, and (4) the plate scatters the jet near-field at low Strouhal numbers, which is observed as a change on the decay rate of the pressure field along the radial distance. Thus, the main mechanism attributed to the augmentation of low Strouhal numbers above the far-field noise of an isolated jet can be attributed to this scattering effect, as the plate modifies evanescent hydrodynamic pressure disturbances into propagating acoustic waves.

The installation effect on the far-field acoustics was assessed in Section 5.3. The computational results were compared with experimental data, showing a good agreement and proving to be able to capture the installation effects on the far-field acoustics. This includes the augmentation on the low Strouhal number associated with the scattering of the jet near-field and the jet-surface reflection effects responsible for shielding and reflecting the acoustic field at mid and high Strouhal numbers. It was observed that the peak Strouhal in which the installation effect is maximum was $\mathrm{St}_{D_\mathrm{J}} = 0.26$ for all cases, which is in agreement with the literature.

Finally, the use of a solid FWH surface to investigate the plate contribution to the far-field noise was assessed in Section 5.4. The results suggest that the installation noise can be broken down into a incoherent energetic sum of the contributions of the isolated jet (quadrupole noise sources) and the pressure fluctuations on the plate surface (dipole noise sources). This approach was further employed to investigate the contributions of each noise source to the far-field, from where it can be concluded that the contribution of the plate is verified to be strongly dependent on the plate distance to the jet flow, on the polar observation angle and on the Strouhal number.

6.1 Suggestions for future work

The results achieved in this work highlights the capabilities of the numerical model to simulate the aeroacoustics of isolated and installed subsonic jets. Thus, the following suggestions are made for future investigations of jet noise and installation effects using PowerFLOW:

- The validation analysis suggests that further information regarding the flow field computation is required. Thus, improved validation procedures involving the evaluation of the turbulence spectra and azimuthal modes with experimental data are recommended;
- As only one flow condition was assessed in this work, the validation of computational models for different flow conditions (higher mach values and/or different temperature ratios) is suggested;
- The use of the computational model to develop low order models of the jet near-field is proposed since this is a rather time consuming task to be performed experimentally;
- Investigation regarding more realistic installation configurations involving inclined or sweep plates, as well as jet-flap interaction noise;
- Investigation of the flight stream effect on the jet flow and acoustics for isolated and installation configurations;
- Investigation of passive noise reduction strategies such as chevron nozzles or microjets.

REFERENCES

[1] NETO, J. R. de L.; CARDOSO, C. A. Impacto sonoro do aeroporto santos dumont/rj: análise e medidas de controle. **Paranoá: cadernos de arquitetura e urbanismo**, n. 12.

[2] SCHRECKENBERG, D. et al. Aircraft noise and quality of life around frankfurt airport. **International journal of environmental research and public health**, Molecular Diversity Preservation International, v. 7, n. 9, p. 3382–3405, 2010.

[3] FLOUD, S. et al. Exposure to aircraft and road traffic noise and associations with heart disease and stroke in six european countries: a cross-sectional study. **Environmental Health**, BioMed Central, v. 12, n. 1, p. 89, 2013.

[4] WEIHOFEN, V. M. et al. Environmental aircraft noise and stroke: a systematic review and meta-analysis. In: . [S.l.]: Proceedings of Internoise 2016, Hamburg, Germany.

[5] INTERNATIONAL CIVIL AVIATION ORGANIZATION. Environmental technical manual - volume i procedures for the noise certification of aircraft. 2005.

[6] ASTLEY, R. et al. Predicting and reducing aircraft noise. 2007.

[7] INTERNATIONAL CIVIL AVIATION ORGANIZATION. Environmental report 2010 - aviation and climate change. **Montreal, Quebec, Canada**, 2010.

[8] ZAPOROZHETS, O.; TOKAREV, V.; ATTENBOROUGH, K. **Aircraft noise propagation, exposure & reduction**. [S.l.]: Spon Press„ 2011.

[9] MARTINEZ, R. M. **Microphone arrays for imaging of aerospace noise sources**. Tese (Doutorado) — Delft University of Technology, 2018.

[10] BERTSCH, E.-L. **Noise prediction within conceptual aircraft design**. Tese (Doutorado) — DLR, 2013.

[11] CASALINO, D. et al. Aircraft noise reduction technologies: a bibliographic review. **Aerospace Science and Technology**, Elsevier, v. 12, n. 1, p. 1–17, 2008.

[12] DYKE, M. V. An album of fluid motion. Parabolic Press Stanford, 1982.

[13] ABRAMOVICH, G. N. et al. The theory of turbulent jets. **Moscow Izdatel Nauka**, 1984.

[14] MATHIEU, J.; SCOTT, J. **An introduction to turbulent flow**. [S.l.]: Cambridge University Press, 2000.

[15] POPE, S. B. **Turbulent flows**. [S.l.]: IOP Publishing, 2001.

[16] NIEUWSTADT, F. T.; WESTERWEEL, J.; BOERSMA, B. J. **Turbulence: Introduction to Theory and Applications of Turbulent Flows**. [S.l.]: Springer, 2016.

[17] WILLIAMS, J. F.; HALL, L. Aerodynamic sound generation by turbulent flow in the vicinity of a scattering half plane. **Journal of fluid mechanics**, Cambridge University Press, v. 40, n. 4, p. 657–670, 1970.

[18] RICHARDSON, L. F. Weather prediction by numerical methods. **Cambridge: Cambridge University Press**, 1922.

[19] HILARES, T. W. C.; ROBERTO, L. **Numerical simulation of the dynamics of turbulent swirling flames**. Tese (Doutorado) — Technische Universität München, 2012.

[20] MCLAUGHLIN, P. **A contribution to the jet noise installation problem**. Tese (Doutorado) — University of Southampton, 2010.

[21] BOGEY, C.; MARSDEN, O. Influence of nozzle-exit boundary-layer profile on high-subsonic jets. In: **20th AIAA/CEAS Aeroacoustics Conference**. [S.l.: s.n.], 2014. p. 2600.

[22] CAVALIERI, A. V. G. **Wavepackets as sound-source mechanisms in subsonic jets**. Tese (Doutorado) — Université de Poitiers, 2012.

[23] DAVIES, P.; FISHER, M.; BARRATT, M. The characteristics of the turbulence in the mixing region of a round jet. **Journal of Fluid Mechanics**, Cambridge University Press, v. 15, n. 3, p. 337–367, 1963.

[24] LAWRENCE, J. **Aeroacoustic interactions of installed subsonic round jets**. Tese (Doutorado) — University of Southampton, 2014.

[25] BATTISTIN, B. **Effects of Surrounding Aircraft Structures on the Noise Produced by Propulsive Jets**. Tese (Doutorado) — Universitá di Padova, 2013.

[26] BRIDGES, J.; WERNET, M. Establishing consensus turbulence statistics for hot subsonic jets. In: **16th AIAA/CEAS aeroacoustics conference**. [S.l.: s.n.], 2010. p. 3751.

[27] WITZE, P. . Centerline velocity decay of compressible free jets. **AIAA journal**, v. 12, n. 4, p. 417–418, 1974.

[28] LIGHTHILL, M. J. On sound generated aerodynamically i. general theory. **Proc. R. Soc. Lond. A**, The Royal Society, v. 211, n. 1107, p. 564–587, 1952.

[29] CAVALIERI, A. V. et al. Axisymmetric superdirectivity in subsonic jets. **Journal of fluid Mechanics**, Cambridge University Press, v. 704, p. 388–420, 2012.

[30] SAVELL, C. Precision and accuracy of jet noise measurements. In: **4th Aeroacoustics Conference**. [S.l.: s.n.], 1977. p. 1302.

[31] HARPER-BOURNE, M. On modelling the hydrodynamic field of high-speed jets. In: **10th AIAA/CEAS aeroacoustics conference**. [S.l.: s.n.], 2004. p. 2830.

[32] SUZUKI, T.; COLONIUS, T. Instability waves in a subsonic round jet detected using a near-field phased microphone array. **Journal of Fluid Mechanics**, Cambridge University Press, v. 565, p. 197–226, 2006.

[33] GUITTON, A. et al. Velocity dependence of the near pressure field of subsonic jets: understanding the associated source mechanisms. In: **13th AIAA/CEAS Aeroacoustics Conference (28th AIAA Aeroacoustics Conference)**. [S.l.: s.n.], 2007. p. 3661.

[34] GRIZZI, S.; CAMUSSI, R. Wavelet analysis of near-field pressure fluctuations generated by a subsonic jet. **Journal of Fluid Mechanics**, Cambridge University Press, v. 698, p. 93–124, 2012.

[35] HOWES, W. L. Distribution of time-averaged pressure fluctuations along the boundary of a round subsonic jet. In: **Technical report NASA/NASA-TN-D-468**. [S.l.: s.n.], 1960. p. 18.

[36] TINNEY, C.; JORDAN, P. The near pressure field of co-axial subsonic jets. **Journal of Fluid Mechanics**, Cambridge University Press, v. 611, p. 175–204, 2008.

[37] ARNDT, R. E.; LONG, D.; GLAUSER, M. The proper orthogonal decomposition of pressure fluctuations surrounding a turbulent jet. **Journal of Fluid Mechanics**, Cambridge University Press, v. 340, p. 1–33, 1997.

[38] TAM, C. K. Jet noise: since 1952. **Theoretical and Computational Fluid Dynamics**, Springer, v. 10, n. 1-4, p. 393–405, 1998.

[39] RIBNER, H. S. Quadrupole correlations governing the pattern of jet noise. **Journal of Fluid Mechanics**, Cambridge University Press, v. 38, n. 1, p. 1–24, 1969.

[40] LUSH, P. Measurements of subsonic jet noise and comparison with theory. **Journal of Fluid Mechanics**, Cambridge Univ Press, v. 46, n. 03, p. 477–500, 1971.

[41] HARPER-BOURNE, M. Jet noise measurements: past and present. **International Journal of Aeroacoustics**, SAGE Publications Sage UK: London, England, v. 9, n. 4-5, p. 559–588, 2010.

[42] WILLIAMS, J. F. The noise from turbulence convected at high speed. **Phil. Trans. R. Soc. Lond. A**, The Royal Society, v. 255, n. 1061, p. 469–503, 1963.

[43] SIROTTO, J. R. d. L. N. **Validação experimental de bancada para medição de ruído de jatos**. Dissertação (Mestrado) — Dissertação (mestrado) - Universidade Federal de Santa Catarina, Centro Tecnológico, Programa de Pós-Graduação em Engenharia Mecânica, Florianópolis, 2016.

[44] HEAD, R.; FISHER, M. Jet/surface interaction noise-analysis of farfield low frequency augmentations of jet noise due to the presence of a solid shield. In: **3rd Aeroacoustics Conference**. [S.l.: s.n.], 1976. p. 502.

[45] LAWRENCE, J.; AZARPEYVAND, M.; SELF, R. Interaction between a flat plate and a circular subsonic jet. In: **17th AIAA/CEAS Aeroacoustics Conference (32nd AIAA Aeroacoustics Conference)**. [S.l.: s.n.], 2011. p. 2745.

[46] CURLE, N. The influence of solid boundaries upon aerodynamic sound. In: THE ROYAL SOCIETY. **Proceedings of the Royal Society of London A: Mathematical, Physical and Engineering Sciences**. [S.l.], 1955. v. 231, n. 1187, p. 505–514.

[47] VELDEN, W. V. D. **Computational aeroacoustic approaches for wind turbine blade noise prediction**. Tese (Doutorado) — Delft University of Technology, 2017.

[48] BROWN, C. Jet-surface interaction test: far-field noise results. In: AMERICAN SOCIETY OF MECHANICAL ENGINEERS. **ASME Turbo Expo 2012: Turbine Technical Conference and Exposition**. [S.l.], 2012. p. 357–369.

[49] ANDERSSON, B. **Computational fluid dynamics for engineers**. Cambridge New York: Cambridge University Press, 2012. ISBN 1107018951.

[50] DECK, S.; TERRACOL, M. **Multiscale and multiresolution approaches in turbulence**. [S.l.]: World Scientific, 2006.

[51] MANNING, T.; LELE, S. A numerical investigation of sound generation in supersonic jet screech. In: **6th Aeroacoustics Conference and Exhibit**. [S.l.: s.n.], 2000. p. 2081.

[52] FREUND, J. B. Noise sources in a low-reynolds-number turbulent jet at mach 0.9. **Journal of Fluid Mechanics**, Cambridge University Press, v. 438, p. 277–305, 2001.

[53] TAM, C. K. Computational aeroacoustics-issues and methods. **AIAA journal**, v. 33, n. 10, p. 1788–1796, 1995.

[54] BOGEY, C.; BAILLY, C.; JUVÉ, D. Noise investigation of a high subsonic, moderate reynolds number jet using a compressible large eddy simulation. **Theoretical and Computational Fluid Dynamics**, Springer, v. 16, n. 4, p. 273–297, 2003.

[55] COLONIUS, T.; LELE, S. K. Computational aeroacoustics: progress on nonlinear problems of sound generation. **Progress in Aerospace sciences**, Elsevier, v. 40, n. 6, p. 345–416, 2004.

[56] BAILLY, C.; BOGEY, C. Contributions of computational aeroacoustics to jet noise research and prediction. **International Journal of Computational Fluid Dynamics**, Taylor & Francis Group, v. 18, n. 6, p. 481–491, 2004.

[57] BODONY, D. J.; LELE, S. K. Current status of jet noise predictions using large-eddy simulation. **AIAA journal**, v. 46, n. 2, p. 364–380, 2008.

[58] WANG, M.; FREUND, J. B.; LELE, S. K. Computational prediction of flow-generated sound. **Annu. Rev. Fluid Mech.**, Annual Reviews, v. 38, p. 483–512, 2006.

[59] TAM, C. K. W.; AURIAULT, L. Jet mixing noise from fine-scale turbulence. **AIAA journal**, v. 37, n. 2, p. 145–153, 1999.

[60] WILLIAMS, J. F.; HAWKINGS, D. L. Sound generation by turbulence and surfaces in arbitrary motion. **Philosophical Transactions of the Royal Society of London A: Mathematical, Physical and Engineering Sciences**, The Royal Society, v. 264, n. 1151, p. 321–342, 1969.

[61] BRÈS, G.; PÉROT, F.; FREED, D. A ffowcs williams-hawkings solver for lattice-boltzmann based computational aeroacoustics. In: **16th AIAA/CEAS Aeroacoustics Conference**. [S.l.: s.n.], 2010. p. 3711.

[62] LEW, P.-T. et al. Noise prediction of a subsonic turbulent round jet using the lattice-boltzmann method. In: **13th AIAA/CEAS Aeroacoustics Conference (28th AIAA Aeroacoustics Conference)**. [S.l.: s.n.], 2007. p. 3636.

[63] LEW, P.-T.; MONGEAU, L.; LYRINTZIS, A. Noise prediction of a subsonic turbulent round jet using the lattice-boltzmann method. **The Journal of the Acoustical Society of America**, ASA, v. 128, n. 3, p. 1118–1127, 2010.

[64] LEW, P.-T. et al. An extended lattice boltzmann methodology for high subsonic jet noise prediction. In: **20th AIAA/CEAS Aeroacoustics Conference**. [S.l.: s.n.], 2014. p. 2755.

[65] BRIDGES, J.; BROWN, C. Small hot jet acoustic rig validation. In: **Technical report NASA/TM-2006-214234**. [S.l.: s.n.], 2005. p. 241.

[66] SILVA, F. D. da et al. Assessment of jet-plate interaction noise using the lattice boltzmann method. In: **21st AIAA/CEAS Aeroacoustics Conference**. [S.l.: s.n.], 2015. p. 2207.

[67] SILVA, F. D. da et al. Numerical assessment of jet-plate interaction with and without sweep. In: **Proceedings of the 22th International Conference on Sound and Vibration**. [S.l.: s.n.], 2015.

[68] VELDEN, W. C. van der et al. Jet noise prediction: Validation and physical insight. In: **2018 AIAA/CEAS Aeroacoustics Conference**. [S.l.: s.n.], 2018. p. 3617.

[69] CROUSE, B. et al. Fundamental aeroacoustics capabilities of the lattice-boltzmann method. In: **12th AIAA/CEAS Aeroacoustics Conference (27th AIAA Aeroacoustics Conference)**. [S.l.: s.n.], 2006. p. 2571.

[70] WILDE, A. Calculation of sound generation and radiation from instationary flows. **Computers & fluids**, Elsevier, v. 35, n. 8, p. 986–993, 2006.

[71] KOTAPATI, R. et al. **The lattice-Boltzmann-VLES Method for automotive fluid dynamics simulation, a review**. [S.l.], 2009.

[72] NOELTING, S.; BRÈS, G.; DETHIOUX, P. A hybrid lattice-boltzmann/fh-w method to predict sources and propagation of landing gear noise. In: **16th AIAA/CEAS Aeroacoustics Conference**. [S.l.: s.n.], 2010. p. 3976.

[73] HABIBI, K.; MONGEAU, L. Prediction of sound absorption by a circular orifice termination in a turbulent pipe flow using the lattice-boltzmann method. **Applied Acoustics**, Elsevier, v. 87, p. 153–161, 2015.

[74] WOLF-GLADROW, D. A. **Lattice-gas cellular automata and lattice Boltzmann models: an introduction**. [S.l.]: Springer, 2004.

[75] SUCCI, S. **The Lattice Boltzmann Equation for Fluid Dynamics and Beyond**. Oxford: Oxford University Press, 2001.

[76] BHATNAGAR, P. L.; GROSS, E. P.; KROOK, M. A model for collision processes in gases. i. small amplitude processes in

charged and neutral one-component systems. **Physical review**, APS, v. 94, n. 3, p. 511, 1954.

[77] CHEN, H.; TEIXEIRA, C.; MOLVIG, K. Digital physics approach to computational fluid dynamics: some basic theoretical features. **International Journal of Modern Physics C**, World Scientific, v. 8, n. 04, p. 675–684, 1997.

[78] CHAPMAN, S.; COWLING, T. G.; BURNETT, D. **The mathematical theory of non-uniform gases: an account of the kinetic theory of viscosity, thermal conduction and diffusion in gases**. [S.l.]: Cambridge university press, 1990.

[79] QIAN, Y.; D'HUMIERES, D.; LALLEMAND, P. Lattice BGK models for Navier-Stokes equation. **Europhysics Letters**, v. 17, n. 6, p. 479–484, 1992.

[80] WOLF-GLADROW, D. A. **Lattice-gas cellular automata and lattice Boltzmann models: an introduction**. [S.l.]: Springer Science & Business Media, 2000.

[81] AIDUN, C. K.; CLAUSEN, J. R. Lattice boltamnn method for complex flows. **Annu. Rev. Fluid Mech.**, v. 42, p. 439–472, 2010.

[82] NIE, X.; SHAN, X.; CHEN, H. A lattice-boltzmann/finite-difference hybrid simulation of transonic flow. In: **47th AIAA Aerospace Sciences Meeting Including the New Horizons Forum and Aerospace Exposition**. [S.l.: s.n.], 2009. p. 139.

[83] ZHANG, R.; FAN, H.; CHEN, H. A lattice boltzmann approach for solving scalar transport equations. **Philosophical Transactions of the Royal Society of London A: Mathematical, Physical and Engineering Sciences**, The Royal Society, v. 369, n. 1944, p. 2264–2273, 2011.

[84] TEIXEIRA, C. M. Incorporating turbulence models into the lattice-boltzmann method. **International Journal of Modern Physics C**, World Scientific, v. 9, n. 08, p. 1159–1175, 1998.

[85] CHEN, H. et al. Expanded analogy between boltzmann kinetic theory of fluids and turbulence. **Journal of Fluid Mechanics**, Cambridge University Press, v. 519, p. 301–314, 2004.

[86] YAKHOT, V.; ORSZAG, S. A. Renormalization group analysis of turbulence. i. basic theory. **Journal of scientific computing**, Springer, v. 1, n. 1, p. 3–51, 1986.

[87] PERVAIZ, M. M.; TEIXEIRA, C. M. Two equation turbulence modeling with the lattice-boltzmann method. **ASME-PUBLICATIONS-PVP**, ASME; 1998, v. 397, n. 1, p. 15–24, 1999.

[88] FARES, E. Unsteady flow simulation of the ahmed reference body using a lattice boltzmann approach. **Computers & fluids**, Elsevier, v. 35, n. 8, p. 940–950, 2006.

[89] SUCCI, S. et al. An integer lattice realization of a lax scheme for transport processes in multiple component fluid flows. **Journal of Computational Physics**, Elsevier, v. 152, n. 2, p. 493–516, 1999.

[90] CANHA, J.; GAVILAN, M.-E. Powerflow: Basic training course. In: . [S.l.]: Unpublished presentation, 2012.

[91] CHEN, H. et al. Grid refinement in lattice boltzmann methods based on volumetric formulation. **Physica A: Statistical Mechanics and its Applications**, Elsevier, v. 362, n. 1, p. 158–167, 2006.

[92] CHEN, H. Volumetric formulation of the lattice boltzmann method for fluid dynamics: Basic concept. **Physical Review E**, APS, v. 58, n. 3, p. 3955, 1998.

[93] CHEN, H.; TEIXEIRA, C.; MOLVIG, K. Realization of fluid boundary conditions via discrete boltzmann dynamics. **International Journal of Modern Physics C**, World Scientific, v. 9, n. 08, p. 1281–1292, 1998.

[94] JONG, A. D. Experimental and numerical investigation of the flow-induced resonance of slender deep cavities. **Master of Science Thesis, Delft University of Technology**, 2008.

[95] EXA-CORPORATION, E. **PowerFLOW User's Guide - Release 5.3**. 2015.

[96] LAUNDER, B. E.; SPALDING, D. B. The numerical computation of turbulent flows. In: **Numerical Prediction of Flow, Heat Transfer, Turbulence and Combustion**. [S.l.]: Elsevier, 1983. p. 96–116.

[97] APPELBAUM, J. **Airframe aeroacoustic best practice - User Guide v1**. [S.l.]: Exa GmbH, 2017.

[98] BRÈS, G. et al. Towards best practices for jet noise predictions with unstructured large eddy simulations. In: **42nd AIAA Fluid Dynamics Conference and Exhibit**. [S.l.: s.n.], 2012. p. 2965.

[99] FARANOSOV, G. A. et al. Cabaret method on unstructured hexahedral grids for jet noise computation. **Computers & fluids**, Elsevier, v. 88, p. 165–179, 2013.

[100] GRECO, G. F. **Assessing PowerFLOW Capabilities for Cold Subsonic Jet Noise Prediction**. [S.l.]: UFSC/EMBRAER internal report, 2017.

[101] SHUR, M. L.; SPALART, P. R.; STRELETS, M. K. Noise prediction for increasingly complex jets. part i: Methods and tests. **International journal of aeroacoustics**, SAGE Publications Sage UK: London, England, v. 4, n. 3, p. 213–245, 2005.

[102] MENDEZ, S. et al. On the use of the ffowcs williams-hawkings equation to predict far-field jet noise from large-eddy simulations. **International Journal of Aeroacoustics**, SAGE Publications Sage UK: London, England, v. 12, n. 1-2, p. 1–20, 2013.

[103] CAMARA, F. A. F. **LVA/UFSC Jet rig aerodynamic validation report**. [S.l.]: UFSC/EMBRAER internal report (*private communication*), 2018.

[104] SHIN, K.; HAMMOND, J. **Fundamentals of signal processing for sound and vibration engineers**. [S.l.]: John Wiley & Sons, 2008.

[105] SILVA, F. Dutra da. **Análise do ruído de jatos interagindo com superfícies sólidas através do método de Lattice-Boltzmann**. 2014. Qualificação de Doutorado, Universidade Federal de Santa Catarina.

[106] MACGREGOR, G.; RIBNER, H.; LAM, H. "basic" jet noise patterns after deletion of convection and refraction effects: Experiments vs. theory. **Journal of Sound and Vibration**, Elsevier, v. 27, n. 4, p. 437–454, 1973.

[107] BROWN, C. A.; WERNET, M. P. Jet-surface interaction test: Flow measurement results. In: **20th AIAA/CEAS Aeroacoustics Conference**. [S.l.: s.n.], 2014. p. 3198.

[108] PROENCA, A.; LAWRENCE, J.; SELF, R. A survey of the turbulence statistics of a model-scale installed jet at low and moderate mach numbers. In: **23rd AIAA/CEAS Aeroacoustics Conference**. [S.l.: s.n.], 2017. p. 3705.

[109] CAVALIERI, A. V. et al. Scattering of wavepackets by a flat plate in the vicinity of a turbulent jet. **Journal of sound and Vibration**, Elsevier, v. 333, n. 24, p. 6516–6531, 2014.

[110] MOLLO-CHRISTENSEN, E. **Measurements of near field pressure of subsonic jets**. [S.l.], 1963.

[111] CROW, S. C.; CHAMPAGNE, F. Orderly structure in jet turbulence. **Journal of Fluid Mechanics**, Cambridge Univ Press, v. 48, n. 03, p. 547–591, 1971.

[112] GUDMUNDSSON, K.; COLONIUS, T. Instability wave models for the near-field fluctuations of turbulent jets. **Journal of Fluid Mechanics**, Cambridge University Press, v. 689, p. 97–128, 2011.

[113] CAVALIERI, A. V. et al. Wavepackets in the velocity field of turbulent jets. **Journal of fluid mechanics**, Cambridge University Press, v. 730, p. 559–592, 2013.

[114] JORDAN, P.; COLONIUS, T. Wave packets and turbulent jet noise. **Annual Review of Fluid Mechanics**, Annual Reviews, v. 45, p. 173–195, 2013.

[115] ANSELMET, F.; MATTEI, P.-O. **Acoustics, aeroacoustics and vibrations**. [S.l.]: John Wiley & Sons, 2016.

[116] HOWE, M. S. **Theory of vortex sound**. [S.l.]: Cambridge University Press, 2003. v. 33.

[117] HIRSCHBERG, A.; RIENSTRA, S. W. An introduction to aeroacoustics. **Eindhoven university of technology**, 2004.

[118] MOORE, P. **Aeroacoustics of compressible subsonic jets**. [S.l.]: Delft: Phd Thesis, Laboratory for Aero & Hydrodynamics, TU Delft, 2009.

[119] LOCKARD, D. A comparison of ffowcs williams-hawkings solvers for airframe noise applications. In: **8th AIAA/CEAS Aeroacoustics Conference & Exhibit**. [S.l.: s.n.], 2002. p. 2580.

[120] BRENTNER, K. S.; FARASSAT, F. Analytical comparison of the acoustic analogy and kirchhoff formulation for moving surfaces. **AIAA journal**, v. 36, n. 8, p. 1379–1386, 1998.

[121] FARASSAT, F. Derivation of formulations 1 and 1a of farassat. **Technical report, TM-2007-214853 NASA**.

[122] CASALINO, D. An advanced time approach for acoustic analogy predictions. **Journal of Sound and Vibration**, Elsevier, v. 261, n. 4, p. 583–612, 2003.

[123] BASTOS, L. P. et al. Development, validation and application of a newly developed rig facility for investigation of jet aeroacoustics. **Journal of the Brazilian Society of Mechanical Sciences and Engineering**, Springer, v. 40, n. 4, p. 171, 2018.

[124] SIROTTO, J. et al. Validation of cold jet noise rig at Laboratory of Acoustic and Vibration (LVA), Federal University of Santa Catarina (UFSC). In: **Proceedings of the 22th international congress on acoustics, Buenos Aires**. [S.l.: s.n.], 2016.

[125] BASTOS, L. P. **Desenvolvimento e emprego de uma bancada para análise de efeitos de instalação sobre jatos de bocais serrilhados**. Tese (Doutorado), 2016.

APPENDIX A – Aerodynamic sound

The term "aerodynamic sound" was introduced by Sir James Lighthill [28], who, prompted by the need for quieter jet aeroengines, developed the fundamental basis towards a better understanding of the physical phenomena involving sound generation by air flows. By manipulating the governing equations of fluid motion, Lighthill derived an exact non-homogeneous form of the wave equation whose source term represents the noise produced by an unbounded turbulence region. Subsequently, Lighthill's theory was extended by Curle [46], Ffowcs Williams & Hawkings [60] and Ffowcs Williams & Hall [17] to include the effects of solid boundaries.

In general, the contribution of these theories, also called aeroacoustic analogies, lies on describing the aerodynamic sound sources in terms of simple sound emitter sources such as monopoles, dipoles or quadrupoles. These analogies comprehends the foundations of Aeroacoustics, a branch of physics concerned with noise generation via either turbulent fluid motion or aerodynamic forces interacting with surfaces, and will be further discussed in this appendix.

A.1 Lighthill's analogy

In his work, Lighthill [28] rearranged the equations of conservation of mass and momentum to obtain a non-homogeneous form of the wave equation with a source term that concerns only an unbounded turbulent region of the fluid. Among some premises adopted for his derivation, the following are listed: 1) the influence of sound generated by the flow in the flow itself can be ignored; 2) sound is radiated in free space; 3) the flow is at low subsonic regime. Having these premises in mind, Lighthill's equation[1] is given by

$$\underbrace{\frac{\partial^2 \rho'}{\partial t^2} - c_\infty^2 \nabla^2 \rho'}_{\text{wave equation}} = \underbrace{\frac{\partial^2 T_{ij}}{\partial x_i \partial x_j}}_{\text{source term}} , \tag{A.1}$$

[1] The complete development of Lighthill's equation can be found in the books of Anselmet et al. [115] and Howe [116].

where c_∞ is the ambient sound speed and ρ' is the fluctuation density relative to the fluid density at rest[2], ρ_0. The source term on the RHS of Equation (A.1) can be interpreted as a distribution of quadrupole sources whose force per unit volume is given by the Lighthill tensor, T_{ij}. Therefore, the conclusion taken from Equation (A.1) is that calculating the sound generated by a unbounded turbulent structures is equivalent to solving the wave equation generated by a quadrupole source propagating in a stationary medium.

The Lighthill tensor is derived under the consideration that the difference between a real fluid and an ideal fluid can be seen as a sound source, and can be expressed as

$$T_{ij} = \underbrace{\rho u_i u_j}_{\text{inertial forces}} + \underbrace{\left(p' - c_\infty^2 \rho'\right) \delta_{ij}}_{\text{entropy}} - \underbrace{\sigma_{ij}}_{\text{viscosity}}, \tag{A.2}$$

where u is the flow velocity, p and p_0 are the total and mean pressure, respectively, δ_{ij} is the Kronecker delta and σ_{ij} is the viscous stress tensor. Each term in Equation (A.2) may play a significant role in the noise generation depending upon the flow conditions. The first term, the Reynolds stress tensor, accounts for the convection of sound waves by the turbulent flow velocity. The second term represents refraction effects caused by local sound speed variations due to temperature gradients. Finally, the last term concerns sound dissipation due to thermal and viscous effects.

If no solid boundaries are present, Equation (A.1) can be solved using a free space green function. Considering an isentropic flow so that pressure and density fluctuations are related by $p' = \rho' c_\infty^2$, the solution in terms of the pressure fluctuation can be expressed as

$$p'(\mathbf{x}, t) = \frac{1}{4\pi} \frac{\partial^2}{\partial x_i \partial x_j} \int_V \frac{T_{ij}(\mathbf{y}, t - \frac{|\mathbf{x}-\mathbf{y}|}{c_\infty})}{|\mathbf{x} - \mathbf{y}|} \mathrm{d}\mathbf{y}, \tag{A.3}$$

where $\mathbf{x}$ is the distance between the origin and the observer in a time t and $\mathbf{y}$ is the distance between the origin and the noise source. Thus, the far-field noise generated by a jet can be obtained by a volume integral involving turbulent quantities at a retarded time, $t - |\mathbf{x} - \mathbf{y}|/c_\infty$, a very demanding task that requires full knowledge of the turbulent flow field. This can be achieved through computational simulations or by approximations of the source term using empirical models.

[2]The fluid properties, such as pressure, velocity and density, are decomposed into a mean value plus a fluctuation component, so that, for example, the total density can be decomposed into $\rho = \rho_0 + \rho'$.

- **Lighthill's eighth power law**

In order to estimate the order of magnitude of the pressure fluctuation in Equation (A.3), Lighthill proposed some approximations based on basic characteristics of the fluid. First, it is assumed that the aerodynamic sound is generated by turbulent eddies with a characteristic length scale of the order of the jet exit diameter, D_J, so that $\mathrm{d}^3\mathbf{y} \sim D_\mathrm{J}^3$. It can be further assumed that the quiescent medium and the flow have the same density and that the velocity will be of the same order as the jet mean exit velocity, U_J. According to Lighthill, the frequency of the noise generated can be approximated by $f \sim U_\mathrm{J}/D_\mathrm{J}$. By neglecting viscous effects and considering that the mean temperature of the jet is the same as that of the ambient fluid, which is a good approximation for high-Reynolds cold jets at low Mach numbers, the Lighthill tensor can be approximated by $T_{ij} \sim \rho u_i u_j \sim \rho_\infty U_\mathrm{J}^2$. Finally, by assuming a far-field condition, the space derivatives can be approximated by $\partial/\partial x \sim c_\infty^{-1}\partial/\partial t \sim 2\pi f c_\infty^{-1}$. According to Hirschberg [117], by applying these simplifications in Equation (A.3), it can be shown that acoustic intensity of the quadrupole source term, I_Q, satisfies the relation

$$I_\mathrm{Q} \sim \rho_\infty U_\mathrm{J}^8 c_\infty^{-5} \left(\frac{D_\mathrm{J}}{r}\right)^2, \tag{A.4}$$

where $r = |\mathbf{x} - \mathbf{y}|$. The total acoustic power of the quadrupoles, W_Q, can be approximated from the sound intensity, giving

$$W_\mathrm{Q} \sim 4\pi r^2 \langle I_\mathrm{Q} \rangle \sim \rho_\infty D_\mathrm{J}^2 U_\mathrm{J}^8 c_\infty^{-5}. \tag{A.5}$$

The Equation (A.5) is Lighthill's eighth power law, which was confirmed experimentally by Lush [40] to provide a quite accurate estimation of the far-field noise generated by a cold subsonic free jet. This law implies that a significant noise reduction can be achieved by reducing the flow velocity. In fact, the eighth power law explains the noise reduction achieved by the high-bypass turbofan aeroengines introduced in the 1960s. In this type of propulsion system, a mass of cold, slow air flows through a bypass duct, allowing the jet velocity to be reduced without compromising the resulting thrust.

A.2 Curle's analogy

Lighthill's analogy does not take solid boundaries into account, making it solely applicable to sound generated by free turbulence. Curle [46] proposed an extension to Lighthill's theory so that the influence of solid boundaries upon the aerodynamic sound field could be incorporated. The author states that the influence of the solid boundary are two-fold:

1. The sound generated by free turbulence (quadrupoles) will be reflected and diffracted by the solid boundaries;

2. A resultant dipole field at the solid boundaries is seen as the quadrupoles will no longer be distributed over the entire space but only throughout the region external to the solid surface. Dipoles are likely, since in acoustics they correspond to forces externally applied to the fluid.

Curle proposed a general solution to Equation (A.1) in which the Lighthill tensor contribution continues being a fundamental part of the phenomena, however, an additional term accounts for the resultant forces exerted upon the fluid by the solid boundaries. If we consider a non-vibrating, solid surface, the solution of Curle's equation is given by

$$p'(\mathbf{x},t) = \underbrace{\frac{1}{4\pi}\frac{\partial^2}{\partial x_i \partial x_j}\int_V \frac{T_{ij}(\mathbf{y},t-\frac{r}{c_\infty})}{r}\mathrm{d}\mathbf{y}}_{\text{quadrupole}} - \underbrace{\frac{1}{4\pi}\frac{\partial}{\partial x_i}\int_S \frac{P_i(\mathbf{y},t-\frac{r}{c_\infty})}{r}\mathrm{d}S(\mathbf{y})}_{\text{dipole}}, \tag{A.6}$$

where $P_i = -\mathbf{n}_j P_{ij}$, being $\mathbf{n}_j$ the outward normal from the fluid and $P_{ij} = p'\delta_{ij} + \sigma_{ij}$ is the compressive stress tensor. The surface integral term in Equation (A.6) include forces due to (a) the impact of sound waves from the quadrupoles on the solid surface and (b) due to the hydrodynamic flow itself. It is shown by Curle that this surface integral is exactly equivalent to the sound generated by a distribution of dipoles with strength P_i per unit area representing the fluctuating forces exerted on the fluid by the solid boundary. This allows the conclusion

that the resulting sound field is generated by two distinct mechanisms, namely (i) a volume distribution of quadrupoles and, (ii) a surface distribution of dipoles.

- **Curle's sixth power law**

Considering turbulent eddies with a length scale in the same order of the surface's characteristic dimension, s, Curle followed the same approach adopted by Lighthill to estimate the order of magnitude of the pressure fluctuations generated by the surface integral at a far-field observer point. This way, Curle showed that the sound intensity generated by the dipoles, I_{D}, satisfies the relation

$$I_{\mathrm{D}} \sim \rho_{\infty} U_{\mathrm{J}}^{6} c_{\infty}^{-3} \left(\frac{s}{r}\right)^{2}. \tag{A.7}$$

From Equation (A.7), it follows that the total acoustic power contribution of the dipoles, W_{D}, is roughly proportional to

$$W_{\mathrm{D}} \sim \rho_{\infty} U_{\mathrm{J}}^{6} c_{\infty}^{-3} s^{2}, \tag{A.8}$$

which is Curle's sixth power law for flow-structure interaction. This way, Curle showed that dipoles should be more efficient sound generating sources than Lighthill's quadrupoles in cases where the Mach number is low enough. Curle's approximation is only valid for acoustic compact surfaces, that is, bodies whose characteristic length scale is much smaller than the acoustic wavelength, λ, being emitted by the turbulent eddies so that $\lambda >> s$.

A.3 Ffowcs Williams & Hall analogy

Ffowcs Williams & Hall [17] considered the problem in where a potential field is radiated by a quadrupole distribution in the vicinity of a sharp edged half plane. In order to establish relations between the acoustic wavelength of the sound sources and the intensity of the scattered field, the authors rewrote Lighthill's equation in the frequency domain. By neglecting viscous effects and considering and isentropic flow, the inhomogeneous Helmholtz equation is obtained from Equation (A.1) as

$$\nabla^{2}\tilde{p}' + k^{2}\tilde{p}' = -\frac{\partial^{2}\rho u_{i} u_{j}}{\partial x_{i}\partial x_{j}}, \tag{A.9}$$

where $k = \omega/c_\infty$ is the acoustic wavenumber, $\omega = 2\pi f$ is the angular frequency and the superscripts $\tilde{(.)}$ denotes a Fourier transformed complex quantity[3]. The solution of the Helmholtz equation for a point source can be expressed in terms of the Green's function, G, as

$$\nabla^2 G + k^2 G = -4\pi\delta(\mathbf{x} - \mathbf{y}), \tag{A.10}$$

where $\delta(.)$ is the Dirac's delta function. This way, the authors applied the second green's theorem to write the solution of Equation (A.9) for a pressure perturbation as

$$\tilde{p}'(\mathbf{x},\omega) = \underbrace{\frac{1}{4\pi}\int_S G\frac{\partial\tilde{p}'}{\partial\mathbf{n}} - \tilde{p}'\frac{\partial G}{\partial\mathbf{n}}\mathrm{d}S}_{\text{scattered noise}} + \underbrace{\frac{1}{4\pi}\int_V G\frac{\partial^2\rho u_i u_j}{\partial x_i\partial x_j}\mathrm{d}\mathbf{y}}_{\text{incident noise}}. \tag{A.11}$$

In Equation (A.11), the term $\partial\tilde{p}'/\partial\mathbf{n} = 0$ as the surface is considered to be rigid and the volume integral is non-zero in the turbulent region. The authors showed that, since the equation above is valid for any Green's function, it is possible to eliminate the surface integral by assuming a condition where $\partial G/\partial\mathbf{n} = 0$. This way, the effect of acoustic scattering will be included in G, and only the information about the Reynolds tensor is needed to estimate the far-field pressure, leading to

$$\tilde{p}'(\mathbf{x},\omega) = \frac{1}{4\pi}\int_V (\rho u_i u_j)\frac{\partial^2 G}{\partial x_i\partial x_j}\mathrm{d}\mathbf{y}. \tag{A.12}$$

Considering Equation (A.12) in cylindrical polar coordinates, Ffowcs Williams & Hall derived an tailored green function satisfying $\partial G/\partial\mathbf{n} = 0$ for a semi-infinite half plane and, through a series of dimensional analysis, they observed that the scattered sound intensity for a non-compact body increases in proportion to the fifth power of the fluid velocity. By comparing this result with Lighthill's eighth power law for free turbulence, or with Curle's sixth power law for the dipole contributions of a compact surface, it is possible to observe that presence of non-compact surfaces considerably impacts the increase in aerodynamic noise generated at low Mach numbers. As another contribution, Ffowcs Williams & Hall's work showed that the scattered pressure intensity has a directional dependence on $\sin^2(\theta/2)$, meaning that the maximum radiation occurs upstream the half plane's trailing edge.

[3]By definition, a Fourier transform of a function $f(t)$ is given by $f(\omega) = \frac{1}{2\pi}\int_{-\infty}^{\infty} f(t)e^{-\mathrm{j}wt}\mathrm{d}t$, being j the complex number.

A.4 Ffowcs Williams & Hawkings analogy

As seen in Appendix A.1, Lighthill's equation was built upon the equations of conservation of mass and momentum of a compressible fluid, whose are valid only at regions exterior to any closed surface. A more general formulation which is applicable to the cases where a moving solid surface is present in the flow field was developed by Ffowcs Williams & Hawkings (FWH) [60] as a generalization of Curle's analogy. To tackle this problem, Ffowcs Williams & Hawkings introduced a system of mathematical control surfaces which encloses the surface of a moving solid body and, using the concept of generalized functions, they were able to rearrange the governing equations of fluid motion into an inhomogeneous form of the wave equation.

Let V be the fluid exterior to a closed control surface S (see Figure A.1), which is mathematically represented by a function $f(\mathbf{x}, t) = 0$, so that

$$f(\mathbf{x},t) = \begin{cases} 0, & \mathbf{x} \in S, \\ < 0, & \mathbf{x} \text{ within } S, \\ > 0, & \mathbf{x} \in V. \end{cases} \tag{A.13}$$

Additionally, let us consider a Heaviside function, defined as

$$H(f) = \begin{cases} 1, & \mathbf{x} \in V, \\ 0, & \mathbf{x} \text{ within } S. \end{cases} \tag{A.14}$$

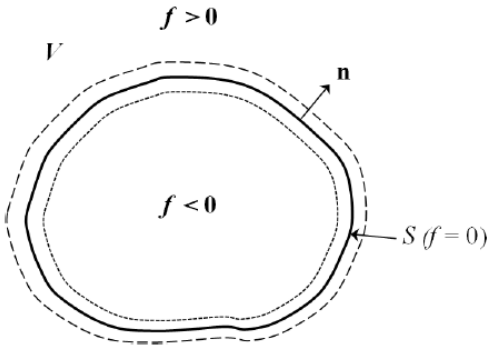

Figure A.1 – Definition of an control surface. Source: Howe [116].

By applying the concept of generalized functions to represent the discontinuities associated with the control surface within the infinite fluid, the Heavyside function can be used to rewrite the governing equations of mass and momentum so that they are valid only at the relevant regions of the domain. This process yields the differential form of the Ffowcs Williams & Hawkings equation, given by [61]

$$\underbrace{\frac{\partial^2 \rho'}{\partial t^2} - c_\infty^2 \nabla^2 \rho'}_{\text{wave equation}} = \underbrace{\frac{\partial}{\partial t}[Q_n \delta(f)]}_{\text{monopole}} - \underbrace{\frac{\partial}{\partial x_i}[L_i \delta(f)]}_{\text{dipole}} + \underbrace{\frac{\partial^2}{\partial x_i \partial x_j}[T_{ij} H(f)]}_{\text{quadrupole}}, \tag{A.15}$$

where $\delta(f)$ is the Dirac's delta function, which is equals to unity when $f(\mathbf{x}, t)$=0 and zero elsewhere. T_{ij} is the Lighthill's tensor (see Equation (A.2)) and the variables Q_n and L_i are defined as

$$Q_n = Q_i \hat{n}_i = [\rho_0 v_i + \rho(u_i - v_i)]\hat{n}_i, \tag{A.16}$$

and

$$L_i = L_{ij} \hat{n}_i = [P_{ij} + \rho u_i (u_j - v_j)]\hat{n}_i, \tag{A.17}$$

where $\hat{n}$=∇f is the unit outward vector normal to the surface[4], v_i are the velocities of the surface and u_i are the fluid velocities on the surface. The compressive stress tensor is given by $P_{ij} = (p - p_0)\delta_{ij} + \sigma_{ij}$.

The source terms in Equation (A.15) shows that, in general, aerodynamic sound can be regarded as generated by three distinct sources: (1) a surface distribution of monopoles which represents a volume displacement effect associated with moving surfaces; (2) a surface distribution of compact dipoles with strength density $P_{ij}\mathbf{n}$ (Curle [46]) and (3) a distribution of acoustic quadrupoles of strength T_{ij} distributed throughout the region exterior to the control surface (Lighthill [28]).

[4]The superscript $\hat{(.)}$ denotes a unit vector.

- **Numerical implementation in PowerFLOW**

For aeroacoustic problems involving large distances, the computational cost of predicting far-field noise is prohibitive as large domains would be required to propagate the sound field without any numerical dissipation and dispersion. Thus, as an interesting application of the FWH equation, arbitrary control surfaces can be used to compute the far-field noise from unsteady compressible flow simulations. If the control surface, $f(\mathbf{x}, t)$=0, corresponds to a solid body, then u_i=v_i in Equations (A.16) and (A.17) and the FWH formulation reduces to Curle's equation[5]. In this case, surface dipole distributions represents sound generation due to unsteady forces acting upon the exterior turbulent field. Moreover, a monopole source term accounts for the sound generated by the displacement of the solid body.

On the other hand, the FWH method is still applicable when the control surface do not corresponds to a solid body. In this case, an arbitrary surface can be used to compute the far-field noise generated by a flow field within a limited region. In such situation, mass and momentum discontinuities on the surface act as noise sources associated with the acoustical field encompassed by the porous surface. This implies that any acoustic sources within the porous surface are automatically accounted for by the surface integral terms. When the surface encompasses all the relevant noise sources, the quadrupole term (see Equation (A.15)) contribution is small compared to the others source terms contributions and is often neglected. According to Moore [118], this approach is especially practical for jet noise calculations as it requires less data storage than predictions based on Lighthill's analogy.

The FWH equation is typically solved using a Green's function, where the temporal and spatial convolution of a free-space Green function with the source terms in Equation (A.15) yields the solution for pressure or density fluctuations at a far-field observe point [119]. However, solving the FWH equation for control surfaces with a complex geometry demands a suitable formulation for an efficient numerical implementation.

[5]This version of the FWH equation is also referred to as the solid (impenetrable) formulation.

The FWH solver available in PowerACOUSTICS 4.0a post processing module is based on Farrassat's formulation 1A [120, 121]. This formulation is extended to a convective wave equation in order to predict the noise generated by an moving acoustic source in a fluid at rest, and measured at a stationary receiver located in the far-field. The FWH formulation is implemented in time-domain using a source-time dominant algorithm [122]. Hereafter, a brief description of the formulation implemented in PowerACOUSTICS is given. More details about the computational implementation can be found in the work of Brès et al. [61].

Neglecting the quadrupole terms, Farassat's formulation 1A solves Equation (A.15) for the acoustic pressure p', at the observer position $\mathbf{x}$ and time t, by the following integral solution

$$p'(\mathbf{x},t) = p'_{\mathrm{T}}(\mathbf{x},t) + p'_{\mathrm{L}}(\mathbf{x},t), \tag{A.18}$$

where subscripts $(.)_{\mathrm{T}}$ and $(.)_{\mathrm{L}}$ correspond to the thickness (monopole source) and loading (dipole source) components. These terms are defined as [61]

$$\begin{aligned} 4\pi p'_{\mathrm{T}}(\mathbf{x},t) = &\int_{f=0} \left[\frac{\dot{Q}_n + Q_{\dot{n}}}{r(1-M_r)^2}\right]_{\mathrm{ret}} \mathrm{d}S \\ &+ \int_{f=0} \left[\frac{Q_n(r\dot{M}_r + c_\infty(M_r - M^2))}{r^2(1-M_r)^3}\right]_{\mathrm{ret}} \mathrm{d}S, \end{aligned} \tag{A.19}$$

and

$$\begin{aligned} 4\pi p'_{\mathrm{L}}(\mathbf{x},t) = &\frac{1}{c_\infty}\int_{f=0} \left[\frac{\dot{L}_r}{r(1-M_r)^2}\right]_{\mathrm{ret}} \mathrm{d}S \\ &+ \int_{f=0} \left[\frac{L_r - L_M}{r^2(1-M_r)^2}\right]_{\mathrm{ret}} \mathrm{d}S \\ &+ \frac{1}{c_\infty}\int_{f=0} \left[\frac{L_r(r\dot{M}_r + c_\infty(M_r - M^2))}{r^2(1-M_r)^3}\right]_{\mathrm{ret}} \mathrm{d}S, \end{aligned} \tag{A.20}$$

where $\dot{(.)}$ superscripts denotes time derivatives with respect to the source time, τ, and $\mathbf{M}$ is the source Mach number, with component $M_i = v_i/c_\infty$. The remaining terms are defined as

$$M_r = M_i \hat{r}_i, \qquad \dot{M}_r = \frac{\partial M_i}{\partial \tau} \hat{r}_i, \tag{A.21}$$

$$Q_n = Q_i \hat{n}_i, \qquad \dot{Q}_n = \frac{\partial Q_i}{\partial \tau} \hat{n}_i, \qquad Q_{\dot{n}} = Q_i \frac{\partial \hat{n}_i}{\partial \tau}, \tag{A.22}$$

$$L_i = L_{ij} \hat{n}_j, \qquad \dot{L}_r = \frac{\partial L_i}{\partial \tau} \hat{r}_i, \qquad L_r = L_i \hat{r}_i, \qquad L_M = L_i M_i. \tag{A.23}$$

The subscript $(.)_{\text{ret}}$ in Equations (A.19) and (A.20) denotes the evaluation of the integrand at a retarded time. This is likely to account for the different relative distances between a moving acoustic source and a stationary observation point. This is done by solving the retarded-time equation for τ_{ret}, which is given by [61]

$$g = \tau_{\text{ret}} - t + \frac{r}{c_\infty}, \tag{A.24}$$

where $r = |\mathbf{x} - \mathbf{y}(\tau_{\text{ret}})|$ is the distance between the observer and the source at the time of emission.

APPENDIX B – Experimental measurements

The experimental campaign of acoustic measurements was performed in the Laboratory of Vibrations & Acoustics (LVA) at the Federal University of Santa Catarina (UFSC), Brazil, which has an experimental Jet Acoustic Rig (JAR) dedicated to study jet aeroacoustics. This facility, which is depicted by Figure B.1, was designed to perform experiments with cold jet flows at subsonic speeds ranging from M_a=0.3 to M_a=0.9.

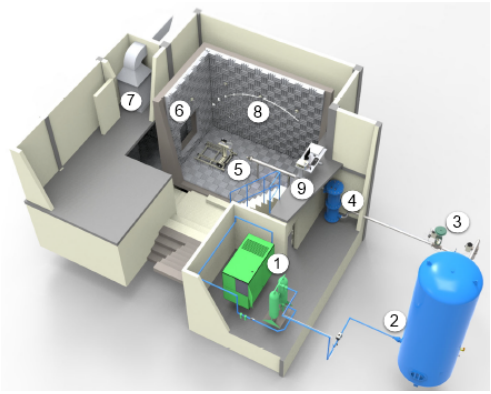

Figure B.1 – Scheme of the Jet Acoustic Rig (JAR) facility: (1) conditioning unit; (2) air reservoir; (3) control valve; (4) plenum vessel; (5) discharge nozzle; (6) anechoic chamber; (7) air collector; (8) polar microphone array and (9) control room. Source: Bastos et al. [123].

The JAR is composed by two main components: (i) an air line responsible for conditioning and supplying the jet exhaust air flow, and (ii) a anechoic chamber containing an acoustic measurement system. First, the air is conditioned by a unit consisting of a industrial compressor, a filter and a dehumidifier, from where air is supplied to a 15 m^3 reservoir. The air flow velocity is controlled by an electronic system responsible for setting the opening percentage of a control valve based on isentropic relations between ambient and stagnation pressure and temperature values. These properties are monitored in real-time during the experiments at the test chamber and inside a plenum vessel. Finally, a 2 meters long duct connects the plenum to a convergent exhaust nozzle SMC000.

The anechoic chamber has an effective volume of 60 m^3 and is decoupled from any structures by an isolation system. The chamber is entirely covered with acoustic foam wedges, including the floor, and presents anechoic conditions above a cutoff frequency of 500 Hz. An air collector section placed downstream the jet flow avoids any recirculations of the jet flow inside the test chamber. Further information on the facility and it's validation are addressed in details by Bastos et al. [123] and Sirotto et al. [124].

- **Acoustic measurement setup & validation**

The experimental setup was set to match the SP03 flow conditions, i.e. M_a=0.5 cold jet (see Table 3.1), while acoustic measurements are performed by a polar array containing ten free-field 1/4″ GRAS 46BE-S1 microphones evenly spaced from θ=30° (downstream) to θ =120° (upstream), where θ=0° corresponds to the exhaust flow direction. Figure B.2a depicts the anechoic chamber's interior while Figure B.2b presents the polar array configuration and conventions.

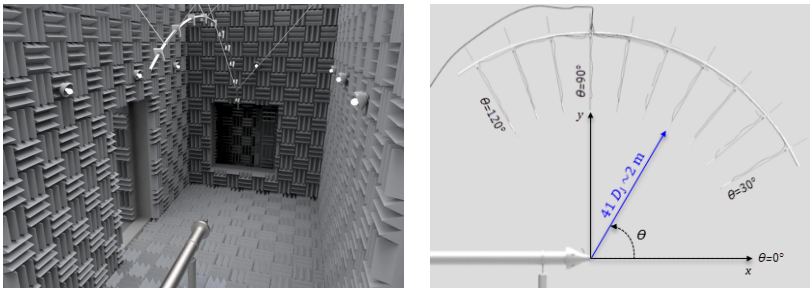

(a) (b)

Figure B.2 – Jet rig facility: (a) anechoic chamber interior and (b) polar microphone array. Source: adapted from Bastos [125].

The microphones are positioned at a radial distance $R = 41D_J \approx$ 2.08 m from the jet exit center, which has been shown by Sirotto [43] to be sufficient to achieve a far-field condition for all frequencies above the chamber's cutoff frequency. The microphones signals were acquired during 20 seconds by a NI PXIe-1082 data acquisition system (DAQ) with a sampling frequency of 120 kHz. The data was obtained for a frequency range of 500 Hz to 40 kHz in Δf=25 Hz narrow bands. A Hanning windowing with 50% overlap is applied to minimize energy

leakage, leading to 2000 spectral averages along the measured pressure time-histories. The background noise during the measurements was no bigger than 30 dB for all microphones.

Figure B.3 compares results of sound pressure levels computed in 1/3 octave bands for different polar angles at the JAR (LVA/UFSC) with experimental data reported by Bridges & Brown [65][1].

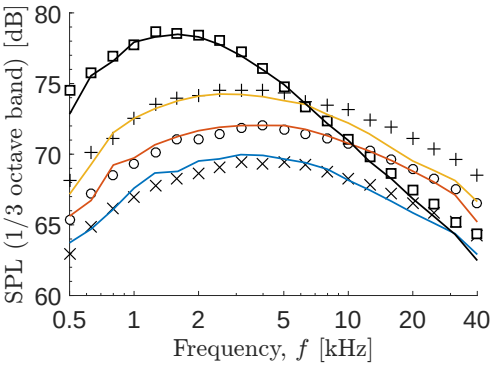

Figure B.3 – 1/3 octave band SPL for different observation polar angles. Experimental results of Bridges & Brown [65] are represented by symbols while measurements conducted at the JAR (LVA/UFSC) are represented by solid lines: $\theta = 30°$ (□,——), $\theta = 60°$ (+,——), $\theta = 90°$ (○,——) and $\theta = 120°$ (×,——).

The results presented by Figure B.3 show that the difference between the measurements performed at the JAR (LVA/UFSC) with data reported in the literature is no bigger than 2 dB for all polar angles. Moreover, the results presented the same directional trends as the ones reported in literature as the SPL presents higher levels at low frequencies for angles downstream the jet flow and a broadband behaviour as the polar angle increases upstream. The bigger deviations are seen at the high frequency range above 10 kHz and can be attributed to small differences between the experiments such as: flow conditions, microphone positioning, calibration, ambient temperature and air humidity.

Figure B.4 complements the verification of the experimental re-

[1] Since the data available by Bridges & Brown [65] was originally computed for a radial distance of $R_{\text{Bridges}} \sim 100 D_{\text{J}}$ away from the nozzle, the reported results are scaled to a radial distance of $R_{\text{JAR}} = 41 D_{\text{J}}$ by applying a geometrical spreading correction factor, given by $20 \log_{10}\left(R_{\text{Bridges}}/R_{\text{JAR}}\right)$.

sults by comparing experimental OASPL results obtained for different polar angles. The spectra energy is integrated from 500 Hz to 40 kHz.

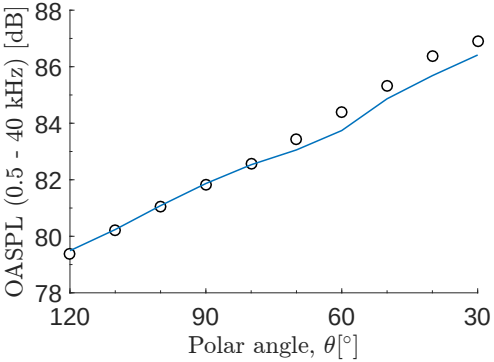

Figure B.4 – Comparison of overall sound pressure levels between experimental data: Bridges & Brown [65] (○) and JAR (LVA/UFSC) (——).

The OASPL results presented in Figure B.4 presents excellent agreement when compared against the experimental data reported by Bridges & Brown, showing differences no bigger than 1 dB for the entire range assessed. The directivity of the noise radiated by the jet is evident as the higher OASPL levels are seen for angles downstream the jet flow. As the polar angle increases upstream, a linear decay trend of the radiated noise magnitude is verified. Therefore, the results presented show that the experiments carried out at the JAR (LVA/UFSC) can reproduce the noise radiated from a cold, turbulent, subsonic jet with a small deviation in comparison with the experiments performed by Bridges & Brown. Therefore, the acoustic measurements conducted at the JAR (LVA/UFSC) are considered validated and will be taken as reference for the validation of the computational model being assessed in this current work.